OPTICAL-EVIDENCE PREDICTIVE REPRESENTATION LEARNING FOR HIDDEN SCREEN RECONSTRUCTION FROM DIFFUSE WALL REFLECTIONS

Anonymous authors
Paper under double-blind review

ABSTRACT

We investigate whether an ordinary RGB camera can recover the content of a hidden screen by observing only the light it casts onto a visible wall. This inverse problem is challenging because indirect propagation attenuates color, luminance, and local structure at different rates, while wall reflectance, ambient illumination, and camera exposure introduce observation-dependent interference. Similar wall patterns can correspond to different screen contents, making the surviving optical cues essential for guiding reconstruction. We propose Optical Evidence Predictive Representation Learning (OEPRL), a reconstruction framework that organizes evidence from observed wall light before using it to correct the decoder's screen-space features. Reliability-Calibrated Optical Evidence Representation (RCER) first organizes the mixed wall response into a global–local optical evidence space, using exposure and contrast to calibrate global conditioning and retaining the positions of informative local regions. Observation-Consistent Optical Predictive Learning (OCPL) then predicts global evidence from decoder features, establishes correspondences between wall and screen regions, and uses prediction errors for sequential global and local corrections guiding hidden-screen reconstruction. Across Browser, Figure, Game, and Lock, OEPRL outperforms all evaluated mainstream image-restoration and passive indirect-reconstruction methods, ranking first in all 12 LPIPS, SSIM, and PSNR comparisons. The method recovers hidden-screen brightness, regional layout, dominant colors, and salient contours using only the diffuse light cast by the screen onto a visible wall. Across diverse screen content, lighting, and viewing conditions, the experiments demonstrate the initial feasibility of recovering hidden-screen content from wall light captured by an ordinary RGB camera.

1 INTRODUCTION

A screen can remain hidden from direct view while its light leaves traces of the displayed content on a nearby wall. Can an ordinary RGB camera recover what the screen displays by observing those traces? Computational periscopy has shown that indirect illumination can reveal hidden color scenes Saunders et al. (2019). We pursue this capability for hidden screens by making their diffuse wall illumination guide the recovery of displayed content. Establishing this capability would extend visual sensing to concealed displays and provide a basis for assessing the information carried by their reflected light.

The first difficulty is finding usable screen information in the mixed wall response. Indirect propagation mixes the displayed content and weakens its color, luminance, and local structure to different degrees, while wall reflectance, ambient light, and exposure further alter the recorded response Faccio et al. (2020). Useful evidence therefore survives in different forms and at different locations within the same observation. A second difficulty arises when that evidence is mapped back to the screen: similar wall patterns can correspond to different displayed content, leaving multiple plausible reconstructions. Hidden-screen recovery therefore requires organizing surviving optical information and using it to correct the reconstruction. These two difficulties motivate a connected sequence: organize the wall response into global and local optical evidence, then use that evidence to guide reconstruction through predictive feedback.

Reviewers: please read the Reviewer Guidelines (iclr.cc/Conferences/2027/ReviewerGuidelines) and the AI Policy for Reviewers (iclr.cc/Conferences/2027/AIPolicyForReviewers). If you used AI to expand, edit, or polish your review, please provide the input text to the LLM. Better still, consider skipping the LLM and submitting your original text: we, and the authors, are much more interested in your unedited thoughts than in what an LLM has to say. AI-assisted or not, you are putting your name and reputation behind your review: LLM-generated falsehoods, hallucinations or misrepresentations are subject to disciplinary action, which may include desk-rejecting all papers you have authored.

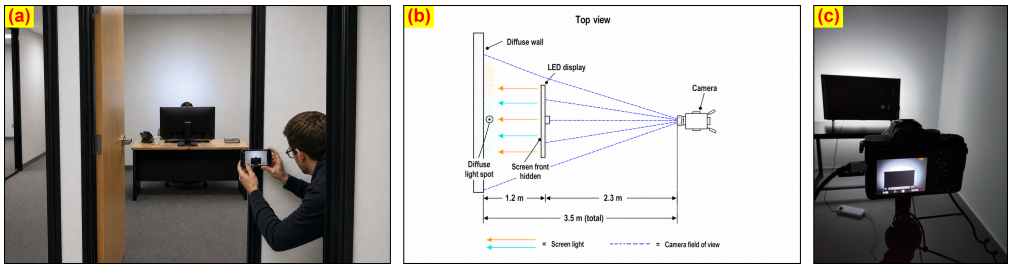

Figure 1: Hidden-screen acquisition setting. (a) Indoor scene illustrating the screen–wall–camera arrangement. (b) Top-view geometry: the hidden screen illuminates a diffuse wall 1.2 m away, while an ordinary RGB camera, positioned 3.5 m from the wall, observes the resulting wall pattern with the screen front outside its field of view. (c) Camera-side view of the physical setup and the recorded diffuse wall response.

To meet these challenges, we propose Optical Evidence Predictive Representation Learning (OEPRL), coupling Reliability-Calibrated Optical Evidence Representation (RCER) with Observation-Consistent Optical Predictive Learning (OCPL) to carry wall cues into hidden-screen reconstruction. RCER organizes the mixed wall response into a global–local optical evidence space. It calibrates global conditioning with exposure and contrast statistics and preserves informative local responses together with their wall positions. OCPL uses this representation to predict global evidence from decoder features, establish regional correspondences, and feed the resulting discrepancies back into the decoder. The two stages structure surviving wall cues as optical evidence, then use discrepancies against it to guide hidden-screen reconstruction. Across Browser, Figure, Game, and Lock, OEPRL outperforms all evaluated mainstream image-restoration and passive indirect-reconstruction methods, ranking first in all 12 category–metric comparisons; on Browser, it improves over the strongest competing result for each metric by 0.0148 LPIPS, 0.0235 SSIM, and 0.714 dB PSNR. Batarseh et al. recovered hidden-object shape information through interferometric spatial-coherence measurements, while Tanaka et al. reconstructed hidden images using a camera fitted with a polarizer Batarseh et al. (2018); Tanaka et al. (2020). OEPRL uses only an ordinary RGB camera for optical acquisition and, through RCER and OCPL, recovers hidden-screen brightness distributions, dominant colors, regional layouts, and salient contours, demonstrating the initial feasibility of recovery from diffuse wall light.

The main contributions are summarized as follows:

(1) We demonstrate the initial feasibility of recovering hidden-screen content from diffuse wall illumination across four content categories and varied observation conditions, with OEPRL ranking first in all 12 LPIPS, SSIM, and PSNR comparisons.

(2) We introduce RCER to organize mixed wall observations into reliability-calibrated global evidence and positioned local tokens, providing a structured optical representation for hidden-screen recovery.

(3) We introduce OCPL to guide hidden-screen reconstruction with observation-derived prediction errors and regional correspondences, carrying the available optical evidence into sequential decoder corrections.

2 Related Work

Indirect Visual Recovery: Indirect imaging recovers hidden scenes from light reaching visible surfaces Faccio et al. (2020). Velten et al. recovered hidden three-dimensional geometry through ultrafast time-of-flight measurements Velten et al. (2012). Bouman et al. used corner-induced radiance variations recorded by consumer RGB cameras to recover angular motion information about hidden subjects Bouman et al. (2017). Saunders et al. recovered two-dimensional color scenes from visible penumbrae using an ordinary digital camera Saunders et al. (2019), and Czajkowski and Murray-Bruce used two orthogonal occluder edges to recover full-color three-dimensional scenes Czajkowski & Murray-Bruce (2024). Learning-based methods further organize the inverse mapping:

NLOS-OT combines manifold embedding with optimal transport Geng et al. (2022), NLOS-LTM infers a latent transport representation for reconstruction modulation with joint reconstruction and reprojection learning Zhang et al. (2025), and learned feature embeddings support indirect imaging and recognition Chen et al. (2020). After learning from paired wall and screen images, OEPRL uses RCER's reliability-calibrated global and positioned local evidence with OCPL's predictive correction to recover static screen content, including browser page frames and graphical color regions (Figure 3).

Conditioning, Selection, and Predictive Representation: Learned restoration develops complementary visual representations through locally enhanced window attention in Uformer Wang et al. (2022), efficient long-range interactions in Restormer Zamir et al. (2022), and simplified restoration blocks in NAFNet Chen et al. (2022). Conditioning adapts these representations through degradation-aware prompts in PromptIR Potlapalli et al. (2023), human instructions in InstructIR Conde et al. (2024), and frequency mining and modulation in AdaIR Cui et al. (2025). Spatially adaptive restoration uses degradation localization to guide restoration, while all-in-one restoration learns degradation representations for subsequent adaptation Purohit et al. (2021); Yao et al. (2024). Adaptive Token Sampling selects informative tokens through adaptive sampling, and TokenLearner forms a compact set of learned visual tokens Fayyaz et al. (2022); Ryoo et al. (2021). Predictive coding uses prediction errors to relate inferred representations to incoming evidence Rao & Ballard (1999), while I-JEPA predicts target-block embeddings from image context Assran et al. (2023). LoFTR and LightGlue establish complementary forms of visual correspondence Sun et al. (2021); Lindenberger et al. (2023). OEPRL uses the same measured wall response for evidence selection and predictive correction. RCER calibrates global conditioning and retains informative local cues with their positions; OCPL uses evidence prediction errors and regional correspondences to turn those cues into sequential corrections of the hidden-screen representation.

3 Method

3.1 Overall Architecture

OEPRL organizes wall evidence, then guides hidden-screen reconstruction with it. RCER outputs a calibrated prompt, a global code, and positioned local tokens: the prompt conditions the encoder, the global code modulates the latent representation, and the tokens feed OCPL at the deepest decoder stage. OCPL applies Optical Predictive Coding (OPC) before Optical Evidence Alignment (OEA), as illustrated in Figure 2.

Let $\mathcal{I} = [0, 1]$ and let $\mathbf{X} \in \mathcal{I}^{B\times 3\times H\times W}$ denote the passive RGB observation and $\mathbf{Y}$ its paired hidden-screen image. The observation boundary and the wall crop derived from it are

$$\mathbf{X} = \mathcal{X}(\mathbf{Y}; \mathbf{R}_{\text{wall}}, \boldsymbol{\ell}) + \mathbf{N}, \qquad \mathbf{W} = \Omega(\mathbf{X}, \mathbf{V}) \in \mathcal{I}^{B\times 3\times H_e\times W_e}. \tag{1}$$

Here, $\mathbf{R}_{\text{wall}}$, $\boldsymbol{\ell}$, and $\mathbf{N}$ denote relay response, ambient illumination, and sensing disturbance. The relation summarizes displayed-content transport; deterministic preprocessing extracts $\mathbf{W}$ using geometry $\mathbf{V}$ for wall-region selection and output placement.

3.2 Reliability-Calibrated Optical Evidence Representation

RCER organizes wall cues by reliability and position: diffuse transport preserves broad color and luminance more reliably than local structure, while exposure and wall reflectance alter both. Let $\mathbf{W}^\circ = \text{clip}_{[0,1]}(\mathbf{W})$ and $\boldsymbol{\gamma} = (0.299, 0.587, 0.114)^\mathsf{T}$. For spatial tensor $\mathbf{Z}$, the 31×31 low-pass relation is

$$[\Phi_{31}(\mathbf{Z})]_{b,c,r,s} = \frac{1}{31^2} \sum_{a=-15}^{15} \sum_{q=-15}^{15} Z_{b,c,r-a,s-q}. \tag{2}$$

With zero padding, this accumulation preserves broad color and luminance while suppressing local variation. Set $\mathbf{L} = \Phi_{31}(\mathbf{W}^\circ)$, $\lambda_{b,r,s} = \sum_{c=1}^{3} \gamma_c W^\circ_{b,c,r,s}$, and $\boldsymbol{\lambda}^{\text{lo}} = \Phi_{31}(\boldsymbol{\lambda})$; the evidence tensor is

$$\mathbf{E} = \text{cat}_{\text{ch}}\Big(\mathbf{W}^\circ, \mathbf{L}, \mathbf{W}^\circ - \mathbf{L}, \boldsymbol{\lambda}, \boldsymbol{\lambda}^{\text{lo}}\Big). \tag{3}$$

Thus, $\mathbf{E} \in \mathbb{R}^{B\times 11\times H_e\times W_e}$, ordered as raw RGB, low-pass RGB, RGB residual, luminance, and low-pass luminance (3 + 3 + 3 + 1 + 1).

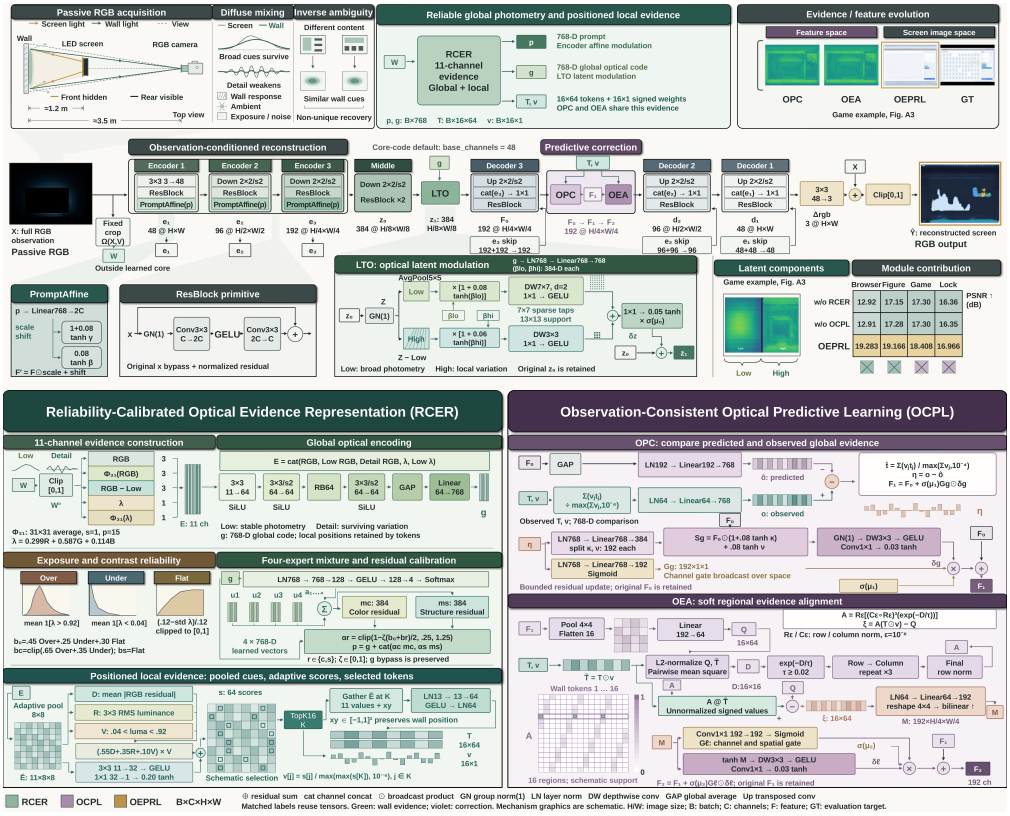

Figure 2: OEPRL combines an observation-conditioned encoder–decoder with RCER evidence formation, latent modulation, and sequential OPC–OEA correction before RGB readout.

Reliability-calibrated global evidence. Let $M = H_e W_e$, $\bar{\lambda}_b = M^{-1} \sum_{r,s} \lambda_{b,r,s}$, and $\sigma_{\lambda,b} = [(M-1)^{-1} \sum_{r,s} (\lambda_{b,r,s} - \bar{\lambda}_b)^2]^{1/2}$. RCER measures overexposure and underexposure directly from the current observation:

$$\rho_b^{\text{over}} = \frac{1}{M} \sum_{r,s} \mathbf{1}[\lambda_{b,r,s} > 0.92], \quad \rho_b^{\text{under}} = \frac{1}{M} \sum_{r,s} \mathbf{1}[\lambda_{b,r,s} < 0.04]. \tag{4}$$

Loss of contrast is measured relative to the contrast threshold 0.12:

$$\rho_b^{\text{flat}} = \text{clip}_{[0,1]} \left(\frac{0.12 - \sigma_{\lambda,b}}{0.12} \right). \tag{5}$$

The three statistics quantify saturation, signal loss, and spatial-contrast loss. The overall score ρ_b^0 uses weights 0.45, 0.25, and 0.30; ρ_b^{c} uses over/underexposure weights 0.65/0.35 and is clipped to $[0, 1]$, while $\rho_b^{\text{s}} = \rho_b^{\text{flat}}$. With learned reliability strength $\zeta \in [0, 1]$, color and structural evidence are calibrated by

$$\alpha_b^{\upsilon} = \text{clip}_{[0.25,1.25]} \left(1 - \frac{\zeta}{2} (\rho_b^0 + \rho_b^{\upsilon}) \right), \qquad \upsilon \in \{\text{c}, \text{s}\}. \tag{6}$$

Thus, unreliable exposure primarily attenuates color conditioning, whereas weak contrast attenuates structural conditioning.

A learned projection Ψ_g maps the evidence tensor to $\mathbf{g}_b \in \mathbb{R}^{768}$. Exponentiating $[\Psi_m(\mathbf{g}_b)]_\varphi$ and normalizing over $\varphi \in \{1, \ldots, 4\}$ gives convex coefficients $a_{b,\varphi}$. With $\mathbf{m}_b^{\text{c}} = \sum_{\varphi=1}^4 a_{b,\varphi} \mathbf{u}_\varphi^{\text{c}}$ and $\mathbf{m}_b^{\text{s}} = \sum_{\varphi=1}^4 a_{b,\varphi} \mathbf{u}_\varphi^{\text{s}}$, the calibrated prompt is

$$\mathbf{p}_b = \mathbf{g}_b + \text{cat}_{\text{ch}} \left(\alpha_b^{\text{c}} \mathbf{m}_b^{\text{c}}, \alpha_b^{\text{s}} \mathbf{m}_b^{\text{s}} \right). \tag{7}$$

The prompt residual contains color and structural halves and applies bounded channel-affine modulation with scale 0.08 at each encoder stage.

The global code guides low- and high-frequency latent processing via the Latent Transport Operator (LTO). Let $\overline{\mathbf{Z}} = \mathcal{N}_z(\mathbf{Z}^{(0)})$, $\mathbf{Z}^{\mathrm{lo}} = \Phi_5(\overline{\mathbf{Z}})$, $\mathbf{Z}^{\mathrm{hi}} = \overline{\mathbf{Z}} - \mathbf{Z}^{\mathrm{lo}}$, and $(\boldsymbol{\beta}_b^{\mathrm{lo}}, \boldsymbol{\beta}_b^{\mathrm{hi}}) = \Psi_\beta(\mathbf{g}_b)$. The bounded gates are $\mathbf{G}^{\mathrm{lo}} = 1 + 0.08 \tanh \boldsymbol{\beta}^{\mathrm{lo}}$ and $\mathbf{G}^{\mathrm{hi}} = 1 + 0.06 \tanh \boldsymbol{\beta}^{\mathrm{hi}}$; their frequency-selective branches are

$$\mathbf{U}^{\mathrm{lo}} = \mathcal{B}_{\mathrm{lo}}(\mathbf{G}^{\mathrm{lo}} \odot \mathbf{Z}^{\mathrm{lo}}), \qquad \mathbf{U}^{\mathrm{hi}} = \mathcal{B}_{\mathrm{hi}}(\mathbf{G}^{\mathrm{hi}} \odot \mathbf{Z}^{\mathrm{hi}}). \tag{8}$$

The branches contribute through a bounded latent residual:

$$\mathbf{Z}^{(1)} = \mathbf{Z}^{(0)} + 0.05\, \sigma(\mu_0) \tanh\Big(\Delta_z(\mathbf{U}^{\mathrm{lo}} + \mathbf{U}^{\mathrm{hi}})\Big). \tag{9}$$

Equations 8–9 trace $\mathbf{E} \to \mathbf{g} \to \mathbf{Z}^{(1)}$: separate optical gates condition complementary low- and high-frequency features before fusion into the decoder input.

Positioned local evidence. Evidence-Adaptive Tokenization (EAT) retains optical values and positions from informative wall regions. Let $\mathcal{P}_{h\times w}$ denote adaptive average pooling to an $h \times w$ lattice. RCER forms $\overline{\mathbf{E}} = \mathcal{P}_{8\times 8}(\mathbf{E})$; valid exposure at j is $e_{b,j} = \mathbf{1}[0.04 < \overline{E}_{b,10,j} < 0.92]$. The mean absolute RGB residual and local root-mean-square luminance are

$$\delta^{\mathrm{rgb}}_{b,j} = \frac{1}{3}\sum_{m=7}^{9} |\overline{E}_{b,m,j}|, \qquad \delta^{\mathrm{rms}}_{b,j} = \left(\frac{1}{9}\sum_{k\in\mathcal{N}_3(j)} \overline{E}^2_{b,10,k}\right)^{1/2}. \tag{10}$$

Set $\delta^{\mathrm{val}}_{b,j} = e_{b,j}$ and $(w_{\mathrm{rgb}}, w_{\mathrm{rms}}, w_{\mathrm{val}}) = (0.55, 0.35, 0.10)$. We combine these fixed optical scores and add a bounded learned residual:

$$s_{b,j} = e_{b,j} \sum_{q\in\{\mathrm{rgb,rms,val}\}} w_q \delta^q_{b,j} + 0.20 \tanh\Big([\Delta_s(\overline{\mathbf{E}}_b)]_j\Big). \tag{11}$$

Let $\mathcal{K}_b = \mathrm{TopK}(\{s_{b,j}\}_{j=1}^{64}, 16)$ and let $\boldsymbol{\pi}_j \in [-1,1]^2$ be the normalized grid coordinate. The selected values and their positions form the local optical tokens

$$\mathbf{t}_{b,j} = \Pi_t\Big(\mathrm{cat}_{\mathrm{ch}}(\overline{\mathbf{E}}_{b,:,j}, \boldsymbol{\pi}_j)\Big) \in \mathbb{R}^{64}, \qquad j \in \mathcal{K}_b. \tag{12}$$

Each token combines local optical values with wall position. Its signed weight is $\omega_{b,j} = s_{b,j}/\max\{\max_{k\in\mathcal{K}_b} s_{b,k}, 10^{-6}\}$ for the global and regional evidence aggregates.

3.3 Observation-Consistent Optical Predictive Learning

Since wall observations can match multiple screen contents, OCPL forms both correction targets from current tokens $\mathcal{T}_b = \{(\mathbf{t}_{b,j}, \omega_{b,j})\}_{j\in\mathcal{K}_b}$, anchoring decoder updates to measured evidence.

Global predictive correction. Let $\mathbf{F}^{(0)} \in \mathbb{R}^{B\times C_d\times H_d\times W_d}$ be the deepest decoder feature before correction. OPC first forms an evidence-weighted summary of the observed wall tokens:

$$\bar{\mathbf{t}}_b = \left\{\frac{\sum_{j\in\mathcal{K}_b} \omega_{b,j} t_{b,j,d}}{\max\{\sum_{j\in\mathcal{K}_b} \omega_{b,j}, 10^{-4}\}}\right\}_{d=1}^{64}. \tag{13}$$

Spatial averaging gives the decoder summary:

$$\bar{\mathbf{f}}_b = \left\{\frac{1}{H_d W_d}\sum_{u=1}^{H_d}\sum_{v=1}^{W_d} F^{(0)}_{b,c,u,v}\right\}_{c=1}^{C_d}. \tag{14}$$

Their difference defines the global prediction error:

$$\boldsymbol{\eta}_b = \Psi_o(\bar{\mathbf{t}}_b) - \Psi_f(\bar{\mathbf{f}}_b). \tag{15}$$

The global error compares a target projected from selected wall evidence with the decoder summary's prediction. From $[\boldsymbol{\kappa}_b, \boldsymbol{\nu}_b] = \Psi_\eta(\boldsymbol{\eta}_b)$, define $\mathbf{S}_{\mathrm{g}} = \mathbf{F}^{(0)} \odot (1 + 0.08 \tanh \boldsymbol{\kappa}) + 0.08 \tanh \boldsymbol{\nu}$; the bounded global feedback is

$$\mathbf{F}^{(1)} = \mathbf{F}^{(0)} + 0.03\, \sigma(\mu_1)\, \sigma(\Psi_c(\boldsymbol{\eta})) \odot \tanh\big(\Delta_{\mathrm{g}}(\mathbf{S}_{\mathrm{g}})\big). \tag{16}$$

Local optical-evidence alignment. OEA pools globally corrected $\mathbf{F}^{(1)}$ to 4×4 screen cells and projects them to $\mathbf{Q}_b \in \mathbb{R}^{16\times 64}$, with i-th row $\mathbf{Q}_{b,i,:}$. For $\mathbf{z} \in \mathbb{R}^{64}$, let $[\mathcal{N}_{\varepsilon_{\text{norm}}}(\mathbf{z})]_d = z_d / \max\{(\sum_{h=1}^{64} z_h^2)^{1/2}, \varepsilon_{\text{norm}}\}$, where $\varepsilon_{\text{norm}} = 10^{-12}$, and set $\widetilde{\mathbf{t}}_{b,j} = \omega_{b,j}\mathbf{t}_{b,j}$. The component-wise matching cost is

$$D_{b,i,j} = \frac{1}{64}\sum_{d=1}^{64}\left([\mathcal{N}_{\varepsilon_{\text{norm}}}(\mathbf{Q}_{b,i,:})]_d - [\mathcal{N}_{\varepsilon_{\text{norm}}}(\widetilde{\mathbf{t}}_{b,j})]_d\right)^2. \tag{17}$$

Distances yield positive affinities at effective temperature $\bar{\tau} = \max\{\tau, 0.02\}$. Let $\mathcal{R}_{\varepsilon_{\text{den}}}$ and $C_{\varepsilon_{\text{den}}}$ divide entries by row and column sums floored at $\varepsilon_{\text{den}} = 10^{-6}$. Their alternating composition produces the normalized regional transport plan

$$\mathbf{A} = \mathcal{R}_{\varepsilon_{\text{den}}}\left((C_{\varepsilon_{\text{den}}} \circ \mathcal{R}_{\varepsilon_{\text{den}}})^3(\exp(-\mathbf{D}/\bar{\tau}))\right). \tag{18}$$

The plan gathers evidence from multiple wall regions for each screen region:

$$\chi_{b,i} = \sum_{j\in\mathcal{K}_b} A_{b,i,j}\omega_{b,j}\mathbf{t}_{b,j}. \tag{19}$$

The regional error $\boldsymbol{\xi}_{b,i} = \chi_{b,i} - \mathbf{Q}_{b,i,:}$ is projected, reshaped to a 4×4 lattice, and bilinearly interpolated to decoder resolution, producing $\mathbf{M}$; OEA applies the second bounded feedback to $\mathbf{F}^{(1)}$:

$$\mathbf{F}^{(2)} = \mathbf{F}^{(1)} + 0.03\,\sigma(\mu_2)\,\sigma(\Psi_1(\mathbf{M}))\odot\tanh(\Delta_1(\tanh\mathbf{M})). \tag{20}$$

OEA uses this regional discrepancy to refine the feature already corrected by OPC. The remaining decoder combines $\mathbf{F}^{(2)}$ with prompt-conditioned skip features and predicts an RGB residual, yielding $\widehat{\mathbf{Y}} = \text{clip}_{\mathcal{I}}(\mathbf{X} + \Delta_{\text{rgb}})$.

Training. We jointly learn the evidence representation and predictive corrections with the screen-reconstruction objective. The training objective combines ℓ_1, Laplacian, and LPIPS reconstruction terms with output-level distillation from a fixed teacher. The global and regional prediction errors provide feedback within the reconstruction pathway; Appendix B.3 gives the complete training objective and optimization details.

Table 1: Quantitative comparison on Browser, Figure, Game, and Lock. Metrics are evaluated in the valid screen-content region. Best and second-best results are highlighted in red and blue, respectively.

Method	Source	Browser			Figure			Game			Lock		
		LPIPS↓	SSIM↑	PSNR↑	LPIPS↓	SSIM↑	PSNR↑	LPIPS↓	SSIM↑	PSNR↑	LPIPS↓	SSIM↑	PSNR↑
Passive Non-Line-of-Sight Reconstruction													
NLOS-LTM[Zhang et al. (2025)]	TIP'25	0.6546	0.5479	14.588	0.7389	0.5283	13.287	0.7232	0.5405	12.836	0.7770	0.4052	10.889
All-in-One and Universal Image Restoration													
PromptIR[Potlapalli et al. (2023)]	NeurIPS'23	0.4621	0.6696	16.816	0.6198	0.6913	18.757	**0.5708**	0.6599	17.784	**0.6374**	0.5936	15.342
InstructIR[Conde et al. (2024)]	ECCV'24	0.4756	**0.7173**	**18.569**	0.6334	0.6756	18.002	0.5967	0.6590	18.117	0.6489	0.5892	**16.490**
AdaIR[Cui et al. (2025)]	ICLR'25	0.4680	0.6614	16.725	0.6228	0.6690	17.930	0.5754	0.6394	17.436	0.6455	0.5729	15.168
FoundIR[Li et al. (2025)]	ICCV'25	0.6186	0.6304	15.038	0.6618	0.6907	17.388	0.6645	0.6168	16.802	0.6734	0.5771	14.444
OneRestore[Guo et al. (2024b)]	ECCV'24	0.7475	0.4394	8.986	0.7044	0.5863	12.529	0.7474	0.5062	10.313	0.7212	0.5221	12.237
General-Purpose Image Restoration													
AST[Zhou et al. (2024)]	CVPR'24	0.5120	0.6537	16.243	0.6324	0.6386	17.891	0.6158	0.6453	17.456	0.6920	0.5366	15.072
ConvIR[Cui et al. (2024)]	TPAMI'24	0.5840	0.6070	15.261	0.6293	0.7151	18.540	0.6013	0.6515	17.642	0.6867	0.5925	14.911
IRNeXt[Cui et al. (2023)]	ICML'23	0.5487	0.6320	15.986	0.6326	0.6679	17.479	0.5735	**0.6681**	18.136	0.6785	0.6082	16.134
SFHformer[Jiang et al. (2024)]	ECCV'24	0.7660	0.4688	11.408	0.7134	0.5970	13.205	0.7598	0.4620	10.010	0.7404	0.5095	12.461
Uformer[Wang et al. (2022)]	CVPR'22	0.5036	0.6590	16.616	0.6260	0.6187	17.586	0.6142	0.6470	17.547	0.6743	0.5652	15.149
MIRNetv2[Zamir et al. (2023)]	TPAMI'23	0.5132	0.6591	16.431	0.6536	0.7133	18.340	0.6120	0.6559	17.679	0.6575	0.6042	15.211
NAFNet[Chen et al. (2022)]	ECCV'22	**0.4605**	0.6660	17.028	0.6216	0.6477	17.729	0.5759	0.6587	**18.160**	0.6637	0.5619	15.242
DeepSN-Net[Deng et al. (2025)]	TPAMI'25	0.6910	0.4446	11.845	0.6920	0.4993	14.401	0.7390	0.4440	10.868	0.7711	0.4228	12.836
DnCNN[Zhang et al. (2017)]	TIP'17	0.6931	0.4397	8.650	0.6639	0.5738	14.204	0.7258	0.4275	8.738	0.7221	0.4787	11.818
U-Net[Ronneberger et al. (2015)]	MICCAI'15	0.7931	0.3389	7.793	0.6675	0.5658	11.815	0.7581	0.4715	10.285	0.7618	0.4874	12.180
Related Degradations and Domains													
INFWIDE[Zhang et al. (2023)]	TIP'23	0.5558	0.6269	15.310	0.6174	**0.7195**	**19.054**	0.6330	0.6408	16.807	0.7334	0.5224	11.764
MetaWeather[Kim et al. (2024)]	ECCV'24	0.4987	0.7078	18.499	0.6674	0.6677	17.926	0.6264	0.6303	17.831	0.7150	0.5252	15.719
Retinexformer[Cai et al. (2023)]	ICCV'23	0.4916	0.6554	16.889	0.6186	0.6905	17.895	0.5924	0.6556	17.925	0.6506	0.5586	14.600
Pixel2Pixel[Ma et al. (2025)]	TPAMI'25	0.6757	0.4208	10.504	0.6379	0.6145	15.476	0.6917	0.4502	11.140	0.7303	0.5178	12.405
DocRes[Zhang et al. (2024)]	CVPR'24	0.4740	0.6530	16.237	**0.6108**	0.7184	18.772	0.5795	0.6472	17.528	0.6467	**0.6094**	16.357
DEA-Net[Chen et al. (2024)]	TIP'24	0.4941	0.6633	16.587	0.6425	0.7145	18.179	0.5879	0.6579	17.729	0.6742	0.6069	15.962
DehazeFormer[Song et al. (2023)]	TIP'23	0.5156	0.6515	16.567	0.6157	0.7086	18.917	0.6074	0.6494	17.774	0.6687	0.5375	14.873
DarkIR[Feijoo et al. (2025)]	CVPR'25	0.9154	0.0541	5.047	0.9290	0.0384	4.185	0.9361	0.0409	4.465	0.8040	0.0949	8.787
OEPRL	**Ours**	**0.4457**	**0.7408**	**19.283**	**0.5805**	**0.7196**	**19.166**	**0.5543**	**0.6708**	**18.408**	**0.6326**	**0.6095**	**16.966**

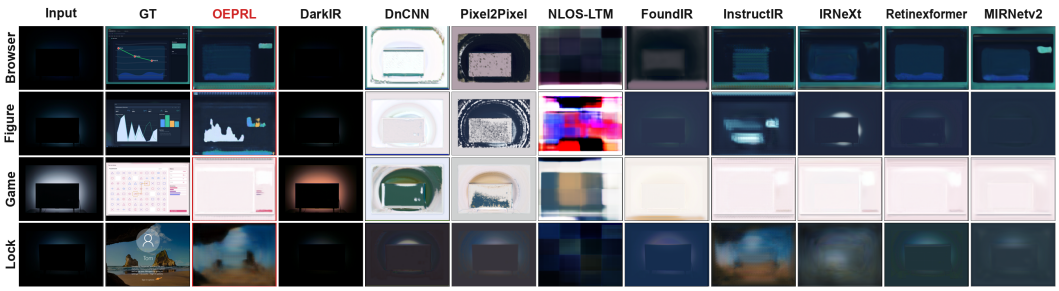

Figure 3: Qualitative comparison on Browser, Figure, Game, and Lock. Each row presents one input–target pair and the corresponding reconstructions from OEPRL and the comparison methods.

4 Experiments and Results

4.1 Experimental Setup

Acquisition and datasets. We use a passive RGB camera to observe the rear of the hidden display and its diffuse reflection on a relay wall, while the displayed pixels remain outside the camera field of view. The screen and camera are approximately 1.2 m and 3.5 m from the wall, respectively. We evaluate Browser, Figure, Game, and Lock, which span web layouts, graphical content, game interfaces, and natural lock-screen imagery. Browser, Figure, and Game each contain 810/90/100 training/validation/test pairs, while Lock contains 891/99/270. Each category is trained and evaluated independently using fixed splits with no cross-split duplicates. Inputs are resized with preserved aspect ratio to a 512×384 canvas; the model receives the passive observation and its deterministically extracted wall crop, and reconstructs RGB content within the valid output region. Checkpoints are selected on the validation split.

Evaluation. We report dataset-level LPIPS ↓ Zhang et al. (2018), SSIM ↑ Wang et al. (2004), and PSNR ↑ Huynh-Thu & Ghanbari (2008) over the valid screen-content regions.

Baselines. We compare OEPRL with passive indirect-reconstruction methods, all-in-one restoration frameworks, general image-restoration backbones, and degradation-specific models. Representative approaches include NLOS-LTM Zhang et al. (2025), INFWIDE Zhang et al. (2023), PromptIR Potlapalli et al. (2023), and Uformer Wang et al. (2022); additional restoration baselines include FoundIR, AST, ConvIR, IRNeXt, MIRNetv2, Retinexformer, DocRes, and DEA-Net Li et al. (2025); Zhou et al. (2024); Cui et al. (2024; 2023); Zamir et al. (2023); Cai et al. (2023); Zhang et al. (2024); Chen et al. (2024). The complete comparison set is listed in Table 1. All methods use the same paired data, splits, input/output resolution, valid evaluation regions, and validation-based model-selection rule.

4.2 Comparison with State-of-the-Art Methods

Table 1 shows a consistent improvement in hidden-screen reconstruction across perceptual similarity, structural agreement, and pixel fidelity: OEPRL ranks first in all twelve category–metric comparisons. The strongest competing methods vary across categories and criteria, while OEPRL combines these advantages within the same reconstruction framework. On Browser, it improves over the strongest competing results by 0.0148 LPIPS, 0.0235 SSIM, and 0.714 dB PSNR. This joint improvement extends from web and graphical layouts to game interfaces and natural lock-screen imagery. NLOS-LTM learns a light-transport representation to modulate reconstruction and regularizes it through joint reconstruction and reprojection learning Zhang et al. (2025). OEPRL uses reliability-calibrated wall evidence to guide sequential decoder corrections, reducing Browser LPIPS from NLOS-LTM's 0.6546 to 0.4457 in our hidden-screen evaluation (Table 1).

Figure 3 shows the screen's principal regions recovered from wall light. OEPRL reconstructs the page frame and dominant horizontal region on Browser, the light graphical profiles and colored bar regions on Figure, the bright main panel and surrounding interface regions on Game, and the broad

color organization and central foreground on Lock. Several comparison methods retain the dark observation pattern, illumination halos, or misplaced color regions. OEPRL more clearly organizes the recovered brightness and color into the screen's principal regions. The gain is therefore expressed as screen content: page structure, graphical regions, interface layout, and foreground–background organization emerge from diffuse wall light.

4.3 Ablation Study

Table 2 isolates the two operations behind recovery: RCER organizes wall evidence and OCPL uses it for reconstruction correction. Tables A1–A2 trace their internal contributions.

Removing RCER or OCPL worsens reconstruction across all four categories and all three metrics. On Browser, RCER removal lowers PSNR from 19.283 to 12.92 dB, with OCPL removal producing a comparable reduction. RCER organizes wall cues as usable evidence; OCPL converts evidence discrepancies into reconstruction feedback.

Table 2: Removal and replacement of RCER and OCPL. Red identifies the complete OEPRL model; blue marks the best alternative within each variant group for each metric.

Method	Source venue	Browser			Figure			Game			Lock		
		LPIPS↓	SSIM↑	PSNR↑	LPIPS↓	SSIM↑	PSNR↑	LPIPS↓	SSIM↑	PSNR↑	LPIPS↓	SSIM↑	PSNR↑
RCER Variants													
w/o RCER	–	0.6897	0.5591	12.92	0.6373	0.6439	17.15	0.6160	0.5939	17.30	0.6550	0.5855	16.36
RCER→FcaNet	ICCV'21	0.6472	**0.5919**	14.27	0.6265	0.6565	18.14	**0.6137**	0.5771	17.37	0.6557	0.5853	16.38
RCER→Coordinate Attention	CVPR'21	**0.6433**	0.5901	**14.38**	**0.6249**	**0.6570**	**18.25**	0.6145	0.5790	17.35	**0.6542**	0.5806	**16.67**
RCER→SimAM	ICML'21	0.6473	0.5915	14.22	0.6258	0.6564	18.15	0.6141	0.5859	17.34	0.6561	0.5851	16.41
OCPL Variants													
w/o OCPL	–	0.6900	0.5591	12.91	0.6345	0.6456	17.28	0.6160	0.5945	17.30	0.6547	0.5859	16.35
OCPL→Restormer-MDTA	CVPR'22	0.6800	0.5708	13.22	0.6301	0.6545	17.63	0.6140	0.6049	17.48	0.6544	0.5860	16.39
OCPL→PromptIR	NeurIPS'23	0.6815	0.5690	13.19	0.6320	0.6516	17.50	0.6150	0.6037	17.46	0.6547	0.5860	16.37
OCPL→DiffIR	ICCV'23	0.6796	0.5724	13.24	0.6318	0.6529	17.54	0.6143	**0.6063**	**17.50**	0.6548	**0.5861**	16.38
OEPRL	–	**0.4457**	**0.7408**	**19.283**	**0.5805**	**0.7196**	**19.166**	**0.5543**	**0.6708**	**18.408**	**0.6326**	**0.6095**	**16.966**

The replacement test compares RCER's optical-evidence representation with established attention mechanisms. FcaNet emphasizes frequency channels Qin et al. (2021), Coordinate Attention retains directional position Hou et al. (2021), and SimAM estimates neuron importance Yang et al. (2021). RCER's exposure- and contrast-calibrated, positioned evidence raises Browser SSIM from 0.5901–0.5919 to 0.7408 (Table 2); Figure 4 shows cleaner page and game regions for OEPRL.

Restormer models long-range feature interactions, PromptIR conditions on degradation, and DiffIR estimates a compact restoration prior Zamir et al. (2022); Potlapalli et al. (2023); Xia et al. (2023); with OCPL's sequential predictive correction and regional correspondence, OEPRL reaches 19.283 dB PSNR on Browser versus 13.19–13.24 dB for their replacements (Table 2).

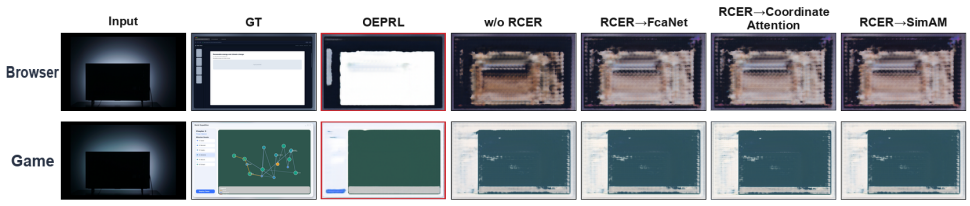

Figure 4: RCER removal and replacement on Browser and Game examples. Columns show the input, ground truth, OEPRL, RCER removal, and RCER replacement with FcaNet, Coordinate Attention, and SimAM, respectively.

The supplementary tests connect the gains to wall evidence: spatial occlusions identify influential regions (Figure A3), EAT interventions concentrate support in selected evidence (Table A3), and the representation remains strongest under a shared U-Net from clean to corrupted observations (Table A4). These tests identify the wall evidence RCER organizes for OCPL's predictive correction.

4.4 Robustness to Observation Variations

Having recovered four types of hidden-screen content, we next examine how this capability responds to changes in the wall measurements. Under additive Gaussian noise on Lock, OEPRL leads LPIPS, SSIM, and PSNR at every level from 20 to 40 dB SNR, including the strongest noise condition. Appendix C follows the same recovery question through changes in illumination, viewing geometry, relay-surface response, blur, shake, and lens configuration.

Table 3: Reconstruction results on Lock under additive Gaussian noise. Column headers denote signal-to-noise ratio in dB; PSNR is reported in dB. Best and second-best results are highlighted in red and blue, respectively.

Method	20 dB			25 dB			30 dB			35 dB			40 dB		
	LPIPS↓	SSIM↑	PSNR (dB)↑	LPIPS↓	SSIM↑	PSNR (dB)↑	LPIPS↓	SSIM↑	PSNR (dB)↑	LPIPS↓	SSIM↑	PSNR (dB)↑	LPIPS↓	SSIM↑	PSNR (dB)↑
Passive Non-Line-of-Sight Reconstruction															
NLOS-LTM	0.7862	0.2978	9.73	0.7814	0.3281	9.97	0.7775	0.3655	10.34	0.7767	0.3921	10.72	0.7771	0.4021	10.86
All-in-One and Universal Image Restoration															
InstructIR	**0.6582**	**0.5721**	**16.48**	**0.6515**	**0.5828**	**16.49**	**0.6496**	**0.5869**	**16.49**	**0.6491**	**0.5884**	**16.49**	**0.6489**	**0.5890**	**16.49**
OneRestore	0.7299	0.5095	12.16	0.7231	0.5178	12.16	0.7227	0.5208	12.16	0.7235	0.5219	12.15	0.7239	0.5223	12.15
General-Purpose Image Restoration															
SFHformer	0.7424	0.5050	12.39	0.7410	0.5082	12.40	0.7421	0.5093	12.40	0.7431	0.5097	12.40	0.7435	0.5098	12.40
Uformer	0.6849	0.5540	15.07	0.6802	0.5613	15.08	0.6785	0.5640	15.08	0.6780	0.5649	15.08	0.6779	0.5653	15.08
NAFNet	0.6808	0.5442	15.17	0.6711	0.5557	15.18	0.6681	0.5602	15.19	0.6672	0.5619	15.19	0.6669	0.5625	15.19
DeepSN-Net	0.7824	0.4161	12.75	0.7771	0.4207	12.76	0.7752	0.4222	12.76	0.7745	0.4228	12.76	0.7742	0.4229	12.76
DnCNN	0.7322	0.4645	11.67	0.7273	0.4715	11.68	0.7262	0.4748	11.70	0.7256	0.4769	11.73	0.7250	0.4781	11.75
U-Net	0.7728	0.4763	12.04	0.7665	0.4839	12.04	0.7641	0.4856	12.05	0.7640	0.4867	12.08	0.7642	0.4875	12.10
Related Degradations and Domains															
INFWIDE	0.7427	0.5041	12.52	0.7368	0.5089	12.52	0.7360	0.5108	12.52	0.7361	0.5114	12.53	0.7361	0.5117	12.53
MetaWeather	0.7156	0.5222	15.70	0.7153	0.5241	15.71	0.7152	0.5247	15.72	0.7151	0.5250	15.72	0.7150	0.5252	15.72
Pixel2Pixel	0.7395	0.5152	12.31	0.7361	0.5166	12.31	0.7345	0.5173	12.31	0.7339	0.5176	12.32	0.7336	0.5177	12.32
DehazeFormer	0.6809	0.5238	14.78	0.6744	0.5326	14.80	0.6726	0.5358	14.80	0.6722	0.5370	14.81	0.6721	0.5373	14.81
DarkIR	0.8142	0.0934	8.73	0.8096	0.0930	8.73	0.8080	0.0928	8.73	0.8074	0.0927	8.73	0.8072	0.0927	8.73
OEPRL	**0.6365**	**0.5988**	**17.04**	**0.6296**	**0.6096**	**17.06**	**0.6274**	**0.6138**	**17.07**	**0.6267**	**0.6154**	**17.07**	**0.6264**	**0.6159**	**17.07**

Across the noise sweep, PSNR remains within 17.04–17.07 dB, while perceptual and structural agreement improve as the wall measurements become cleaner (Figure 5). Cleaner wall evidence improves perceptual and structural recovery; OEPRL retains its comparative advantage at the strongest noise level.

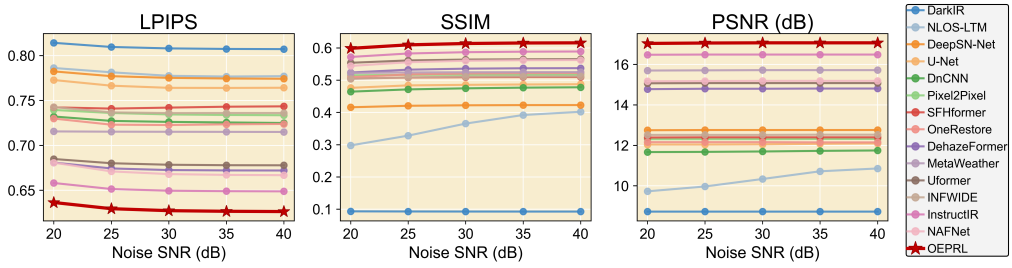

Figure 5: LPIPS, SSIM, and PSNR on Lock under additive Gaussian noise. The emphasized curve denotes OEPRL.

5 Conclusion

This study demonstrates the initial feasibility of recovering hidden-screen content from diffuse wall light captured by an ordinary RGB camera. OEPRL achieves this through a connected evidence-to-reconstruction pathway: RCER organizes the mixed observation into reliability-calibrated global and positioned local evidence, and OCPL turns evidence prediction and regional correspondence into sequential decoder corrections. Across Browser, Figure, Game, and Lock, OEPRL ranks first in all twelve LPIPS, SSIM, and PSNR comparisons. Component ablations, spatial interventions, and evidence-selection tests connect the recovery gain to the organization and use of the observed wall signal. The same optical evidence guides both feature formation and the corrections that produce the final image. The recovered brightness distributions, dominant colors, regional layouts, and salient contours answer the opening question: an ordinary RGB camera can recover information about what a hidden screen displays by observing the light it casts onto a visible wall.

REFERENCES

Mahmoud Assran, Quentin Duval, Ishan Misra, Piotr Bojanowski, Pascal Vincent, Michael Rabbat, Yann LeCun, and Nicolas Ballas. Self-supervised learning from images with a joint-embedding predictive architecture. In *Proceedings of the IEEE/CVF Conference on Computer Vision and Pattern Recognition*, pp. 15619–15629, 2023.

M. Batarseh, S. Sukhov, Z. Shen, H. Gemar, R. Rezvani, and A. Dogariu. Passive sensing around the corner using spatial coherence. *Nature Communications*, 9:3629, 2018. doi: 10.1038/s41467-018-05985-w.

Katherine L. Bouman, Vickie Ye, Adam B. Yedidia, Frédo Durand, Gregory W. Wornell, Antonio Torralba, and William T. Freeman. Turning corners into cameras: Principles and methods. In *Proceedings of the IEEE International Conference on Computer Vision*, pp. 2289–2297, 2017. doi: 10.1109/ICCV.2017.249.

Yuanhao Cai, Hao Bian, Jing Lin, Haoqian Wang, Radu Timofte, and Yulun Zhang. Retinexformer: One-stage Retinex-based transformer for low-light image enhancement. In *Proceedings of the IEEE/CVF International Conference on Computer Vision*, pp. 12470–12479, 2023. doi: 10.1109/ICCV51070.2023.01149. URL https://doi.org/10.1109/ICCV51070.2023.01149.

Liangyu Chen, Xiaojie Chu, Xiangyu Zhang, and Jian Sun. Simple baselines for image restoration. In *Computer Vision – ECCV 2022*, pp. 17–33, 2022. doi: 10.1007/978-3-031-20071-7_2. URL https://doi.org/10.1007/978-3-031-20071-7_2.

Wenzheng Chen, Fangyin Wei, Kiriakos N. Kutulakos, Szymon Rusinkiewicz, and Felix Heide. Learned feature embeddings for non-line-of-sight imaging and recognition. *ACM Transactions on Graphics*, 39(6):1–18, 2020. doi: 10.1145/3414685.3417825. URL https://doi.org/10.1145/3414685.3417825.

Zixuan Chen, Zewei He, and Zhe-Ming Lu. DEA-Net: Single image dehazing based on detail-enhanced convolution and content-guided attention. *IEEE Transactions on Image Processing*, 33: 1002–1015, 2024. doi: 10.1109/TIP.2024.3354108. URL https://doi.org/10.1109/TIP.2024.3354108.

Marcos V. Conde, Gregor Geigle, and Radu Timofte. InstructIR: High-quality image restoration following human instructions. In *Computer Vision – ECCV 2024*, pp. 1–21, 2024. doi: 10.1007/978-3-031-72764-1_1. URL https://doi.org/10.1007/978-3-031-72764-1_1.

Yuning Cui, Wenqi Ren, Sining Yang, Xiaochun Cao, and Alois Knoll. IRNeXt: Rethinking convolutional network design for image restoration. In *Proceedings of the 40th International Conference on Machine Learning*, volume 202 of *Proceedings of Machine Learning Research*, pp. 6545–6564. PMLR, 2023. URL https://proceedings.mlr.press/v202/cui23d.html.

Yuning Cui, Wenqi Ren, Xiaochun Cao, and Alois Knoll. Revitalizing convolutional network for image restoration. *IEEE Transactions on Pattern Analysis and Machine Intelligence*, 46 (12):9423–9438, 2024. doi: 10.1109/TPAMI.2024.3419007. URL https://doi.org/10.1109/TPAMI.2024.3419007.

Yuning Cui, Syed Waqas Zamir, Salman Khan, Alois Knoll, Mubarak Shah, and Fahad Shahbaz Khan. AdaIR: Adaptive all-in-one image restoration via frequency mining and modulation. In *The Thirteenth International Conference on Learning Representations*, 2025. URL https://openreview.net/forum?id=M5t0WvjfCg.

Robinson Czajkowski and John Murray-Bruce. Two-edge-resolved three-dimensional non-line-of-sight imaging with an ordinary camera. *Nature Communications*, 15(1):1162, 2024. doi: 10.1038/s41467-024-45397-7. URL https://doi.org/10.1038/s41467-024-45397-7.

Xin Deng, Chenxiao Zhang, Lai Jiang, Jingyuan Xia, and Mai Xu. DeepSN-Net: Deep semi-smooth Newton driven network for blind image restoration. *IEEE Transactions on Pattern Analysis and Machine Intelligence*, 47(4):2632–2646, 2025. doi: 10.1109/TPAMI.2024.3525089. URL https://doi.org/10.1109/TPAMI.2024.3525089.

Daniele Faccio, Andreas Velten, and Gordon Wetzstein. Non-line-of-sight imaging. *Nature Reviews Physics*, 2(6):318–327, 2020. doi: 10.1038/s42254-020-0174-8. URL https://doi.org/10.1038/s42254-020-0174-8.

Mohsen Fayyaz, Soroush Abbasi Koohpayegani, Farnoush Rezaei Jafari, Sunando Sengupta, Hamid Reza Vaezi Joze, Eric Sommerlade, Hamed Pirsiavash, and Jürgen Gall. Adaptive token sampling for efficient vision transformers. In *Computer Vision – ECCV 2022*, pp. 396–414, 2022. doi: 10.1007/978-3-031-20083-0_24.

Daniel Feijoo, Juan C. Benito, Alvaro Garcia, and Marcos V. Conde. DarkIR: Robust low-light image restoration. In *Proceedings of the IEEE/CVF Conference on Computer Vision and Pattern Recognition*, pp. 10879–10889, 2025. doi: 10.1109/CVPR52734.2025.01016. URL https://doi.org/10.1109/CVPR52734.2025.01016.

Ruixu Geng, Yang Hu, Zhi Lu, Cong Yu, Houqiang Li, Hengyu Zhang, and Yan Chen. Passive non-line-of-sight imaging using optimal transport. *IEEE Transactions on Image Processing*, 31: 110–124, 2022. doi: 10.1109/TIP.2021.3128312.

Hang Guo, Jinmin Li, Tao Dai, Zhihao Ouyang, Xudong Ren, and Shu-Tao Xia. MambaIR: A simple baseline for image restoration with state-space model. In *Computer Vision – ECCV 2024*, pp. 222–241, 2024a. doi: 10.1007/978-3-031-72649-1_13.

Yu Guo, Yuan Gao, Yuxu Lu, Huilin Zhu, Ryan Wen Liu, and Shengfeng He. OneRestore: A universal restoration framework for composite degradation. In *Computer Vision – ECCV 2024*, pp. 255–272, 2024b. doi: 10.1007/978-3-031-72655-2_15. URL https://doi.org/10.1007/978-3-031-72655-2_15.

Qibin Hou, Daquan Zhou, and Jiashi Feng. Coordinate attention for efficient mobile network design. In *Proceedings of the IEEE/CVF Conference on Computer Vision and Pattern Recognition*, pp. 13713–13722, 2021. doi: 10.1109/CVPR46437.2021.01350.

Q. Huynh-Thu and M. Ghanbari. Scope of validity of PSNR in image/video quality assessment. *Electronics Letters*, 44(13):800–801, 2008. doi: 10.1049/el:20080522. URL https://doi.org/10.1049/el:20080522.

Xingyu Jiang, Xiuhui Zhang, Ning Gao, and Yue Deng. When fast Fourier transform meets transformer for image restoration. In *Computer Vision – ECCV 2024*, pp. 381–402, 2024. doi: 10.1007/978-3-031-72995-9_22. URL https://doi.org/10.1007/978-3-031-72995-9_22.

Youngrae Kim, Younggeol Cho, Thanh-Tung Nguyen, Seunghoon Hong, and Dongman Lee. MetaWeather: Few-shot weather-degraded image restoration. In *Computer Vision – ECCV 2024*, pp. 206–222, 2024. doi: 10.1007/978-3-031-73464-9_13. URL https://doi.org/10.1007/978-3-031-73464-9_13.

Hao Li, Xiang Chen, Jiangxin Dong, Jinhui Tang, and Jinshan Pan. FoundIR: Unleashing million-scale training data to advance foundation models for image restoration. In *Proceedings of the IEEE/CVF International Conference on Computer Vision*, pp. 12626–12636, 2025. doi: 10.1109/ICCV51701.2025.01173. URL https://doi.org/10.1109/ICCV51701.2025.01173.

Philipp Lindenberger, Paul-Edouard Sarlin, and Marc Pollefeys. LightGlue: Local feature matching at light speed. In *Proceedings of the IEEE/CVF International Conference on Computer Vision*, pp. 17627–17638, 2023. doi: 10.1109/ICCV51070.2023.01616.

Qing Ma, Junjun Jiang, Xiong Zhou, Pengwei Liang, Xianming Liu, and Jiayi Ma. Pixel2Pixel: A pixelwise approach for zero-shot single image denoising. *IEEE Transactions on Pattern Analysis and Machine Intelligence*, 47(6):4614–4629, 2025. doi: 10.1109/TPAMI.2025.3546870. URL https://doi.org/10.1109/TPAMI.2025.3546870.

Gonzalo Mena, David Belanger, Scott Linderman, and Jasper Snoek. Learning latent permutations with Gumbel-Sinkhorn networks. In *International Conference on Learning Representations*, 2018. URL https://openreview.net/forum?id=Byt3oJ-0W.

Vaishnav Potlapalli, Syed Waqas Zamir, Salman Khan, and Fahad Shahbaz Khan. PromptIR: Prompting for all-in-one image restoration. In *Advances in Neural Information Processing Systems*, volume 36, pp. 71275–71293, 2023. doi: 10.52202/075280-3121. URL https://doi.org/10.52202/075280-3121.

Kuldeep Purohit, Maitreya Suin, A. N. Rajagopalan, and Vishnu Naresh Boddeti. Spatially-adaptive image restoration using distortion-guided networks. In *2021 IEEE/CVF International Conference on Computer Vision*, pp. 2289–2299, 2021. doi: 10.1109/ICCV48922.2021.00231. URL https://doi.org/10.1109/ICCV48922.2021.00231.

Zequn Qin, Pengyi Zhang, Fei Wu, and Xi Li. FcaNet: Frequency channel attention networks. In *Proceedings of the IEEE/CVF International Conference on Computer Vision*, pp. 783–792, 2021. doi: 10.1109/ICCV48922.2021.00082.

Rajesh P. N. Rao and Dana H. Ballard. Predictive coding in the visual cortex: A functional interpretation of some extra-classical receptive-field effects. *Nature Neuroscience*, 2(1):79–87, 1999. doi: 10.1038/4580.

Olaf Ronneberger, Philipp Fischer, and Thomas Brox. U-Net: Convolutional networks for biomedical image segmentation. In *Medical Image Computing and Computer-Assisted Intervention – MICCAI 2015*, pp. 234–241, 2015. doi: 10.1007/978-3-319-24574-4_28. URL https://doi.org/10.1007/978-3-319-24574-4_28.

Michael Ryoo, AJ Piergiovanni, Anurag Arnab, Mostafa Dehghani, and Anelia Angelova. TokenLearner: Adaptive space-time tokenization for videos. In *Advances in Neural Information Processing Systems*, volume 34, pp. 12786–12797, 2021.

Charles Saunders, John Murray-Bruce, and Vivek K. Goyal. Computational periscopy with an ordinary digital camera. *Nature*, 565(7740):472–475, 2019. doi: 10.1038/s41586-018-0868-6. URL https://doi.org/10.1038/s41586-018-0868-6.

Yuda Song, Zhuqing He, Hui Qian, and Xin Du. Vision transformers for single image dehazing. *IEEE Transactions on Image Processing*, 32:1927–1941, 2023. doi: 10.1109/TIP.2023.3256763. URL https://doi.org/10.1109/TIP.2023.3256763.

Jiaming Sun, Zehong Shen, Yuang Wang, Hujun Bao, and Xiaowei Zhou. LoFTR: Detector-free local feature matching with transformers. In *Proceedings of the IEEE/CVF Conference on Computer Vision and Pattern Recognition*, pp. 8922–8931, 2021. doi: 10.1109/CVPR46437.2021.00881.

Kenichiro Tanaka, Yasuhiro Mukaigawa, and Achuta Kadambi. Polarized non-line-of-sight imaging. In *Proceedings of the IEEE/CVF Conference on Computer Vision and Pattern Recognition*, pp. 2136–2145, 2020. doi: 10.1109/CVPR42600.2020.00221.

Andreas Velten, Thomas Willwacher, Otkrist Gupta, Ashok Veeraraghavan, Moungi G. Bawendi, and Ramesh Raskar. Recovering three-dimensional shape around a corner using ultrafast time-of-flight imaging. *Nature Communications*, 3:745, 2012. doi: 10.1038/ncomms1747.

Zhendong Wang, Xiaodong Cun, Jianmin Bao, Wengang Zhou, Jianzhuang Liu, and Houqiang Li. Uformer: A general u-shaped transformer for image restoration. In *Proceedings of the IEEE/CVF Conference on Computer Vision and Pattern Recognition*, pp. 17662–17672, 2022. doi: 10.1109/CVPR52688.2022.01716. URL https://doi.org/10.1109/CVPR52688.2022.01716.

Zhou Wang, Alan C. Bovik, Hamid R. Sheikh, and Eero P. Simoncelli. Image quality assessment: From error visibility to structural similarity. *IEEE Transactions on Image Processing*, 13(4):600–612, 2004. doi: 10.1109/TIP.2003.819861. URL https://doi.org/10.1109/TIP.2003.819861.

Bin Xia, Yulun Zhang, Shiyin Wang, Yitong Wang, Xinglong Wu, Yapeng Tian, Wenming Yang, and Luc Van Gool. DiffIR: Efficient diffusion model for image restoration. In *Proceedings of the IEEE/CVF International Conference on Computer Vision*, pp. 13095–13105, 2023. doi: 10.1109/ICCV51070.2023.01204.

Lingxiao Yang, Ru-Yuan Zhang, Lida Li, and Xiaohua Xie. SimAM: A simple, parameter-free attention module for convolutional neural networks. In *Proceedings of the 38th International Conference on Machine Learning*, volume 139 of *Proceedings of Machine Learning Research*, pp. 11863–11874, 2021.

Mingde Yao, Ruikang Xu, Yuanshen Guan, Jie Huang, and Zhiwei Xiong. Neural degradation representation learning for all-in-one image restoration. *IEEE Transactions on Image Processing*, 33:5408–5423, 2024. doi: 10.1109/TIP.2024.3456583. URL https://doi.org/10.1109/TIP.2024.3456583.

Syed Waqas Zamir, Aditya Arora, Salman Khan, Munawar Hayat, Fahad Shahbaz Khan, and Ming-Hsuan Yang. Restormer: Efficient transformer for high-resolution image restoration. In *Proceedings of the IEEE/CVF Conference on Computer Vision and Pattern Recognition*, pp. 5728–5739, 2022. doi: 10.1109/CVPR52688.2022.00564.

Syed Waqas Zamir, Aditya Arora, Salman Khan, Munawar Hayat, Fahad Shahbaz Khan, Ming-Hsuan Yang, and Ling Shao. Learning enriched features for fast image restoration and enhancement. *IEEE Transactions on Pattern Analysis and Machine Intelligence*, 45(2):1934–1948, 2023. doi: 10.1109/TPAMI.2022.3167175. URL https://doi.org/10.1109/TPAMI.2022.3167175.

Jiarui Zhang, Ruixu Geng, Xiaolong Du, Yan Chen, Houqiang Li, and Yang Hu. Passive non-line-of-sight imaging with light transport modulation. *IEEE Transactions on Image Processing*, 34: 410–424, 2025. doi: 10.1109/TIP.2024.3518097. URL https://doi.org/10.1109/TIP.2024.3518097.

Jiaxin Zhang, Dezhi Peng, Chongyu Liu, Peirong Zhang, and Lianwen Jin. DocRes: A generalist model toward unifying document image restoration tasks. In *Proceedings of the IEEE/CVF Conference on Computer Vision and Pattern Recognition*, pp. 15654–15664, 2024. doi: 10.1109/CVPR52733.2024.01482. URL https://doi.org/10.1109/CVPR52733.2024.01482.

Kai Zhang, Wangmeng Zuo, Yunjin Chen, Deyu Meng, and Lei Zhang. Beyond a Gaussian denoiser: Residual learning of deep CNN for image denoising. *IEEE Transactions on Image Processing*, 26 (7):3142–3155, 2017. doi: 10.1109/TIP.2017.2662206. URL https://doi.org/10.1109/TIP.2017.2662206.

Richard Zhang, Phillip Isola, Alexei A. Efros, Eli Shechtman, and Oliver Wang. The unreasonable effectiveness of deep features as a perceptual metric. In *Proceedings of the IEEE/CVF Conference on Computer Vision and Pattern Recognition*, pp. 586–595, 2018. doi: 10.1109/CVPR.2018.00068. URL https://doi.org/10.1109/CVPR.2018.00068.

Zhihong Zhang, Yuxiao Cheng, Jinli Suo, Liheng Bian, and Qionghai Dai. INFWIDE: Image and feature space wiener deconvolution network for non-blind image deblurring in low-light conditions. *IEEE Transactions on Image Processing*, 32:1390–1402, 2023. doi: 10.1109/TIP.2023.3244417. URL https://doi.org/10.1109/TIP.2023.3244417.

Shihao Zhou, Duosheng Chen, Jinshan Pan, Jinglei Shi, and Jufeng Yang. Adapt or perish: Adaptive sparse transformer with attentive feature refinement for image restoration. In *Proceedings of the IEEE/CVF Conference on Computer Vision and Pattern Recognition*, pp. 2952–2963, 2024. doi: 10.1109/CVPR52733.2024.00285. URL https://doi.org/10.1109/CVPR52733.2024.00285.

APPENDIX FOR OEPRL: HIDDEN SCREEN RECONSTRUCTION FROM DIFFUSE WALL REFLECTIONS

Supplementary Material for Optical-Evidence Predictive Representation Learning for Hidden Screen Reconstruction from Diffuse Wall Reflections

A SCENE AND ACQUISITION DETAILS

A.1 PHYSICAL GEOMETRY AND RECONSTRUCTION INPUTS

The hidden display and the RGB camera are approximately 1.2 m and 3.5 m from the relay wall, respectively. The camera faces the wall and the rear of the screen while the displayed pixels remain outside its direct view. Light emitted by the screen is mixed through screen-to-wall-to-camera propagation, leaving broad color and luminance organization in the visible wall response. Figure 1 shows the acquisition geometry and the camera-side observation.

The supplementary acquisition photographs show the wall and display rear observed by the camera. In the office setup, the LED display faces the relay wall and the camera records the illuminated wall surface together with the rear of the display from the same indoor arrangement. The display front therefore remains outside the camera's direct view throughout acquisition. Figure A1 combines the documented geometry with two views of the arrangement.

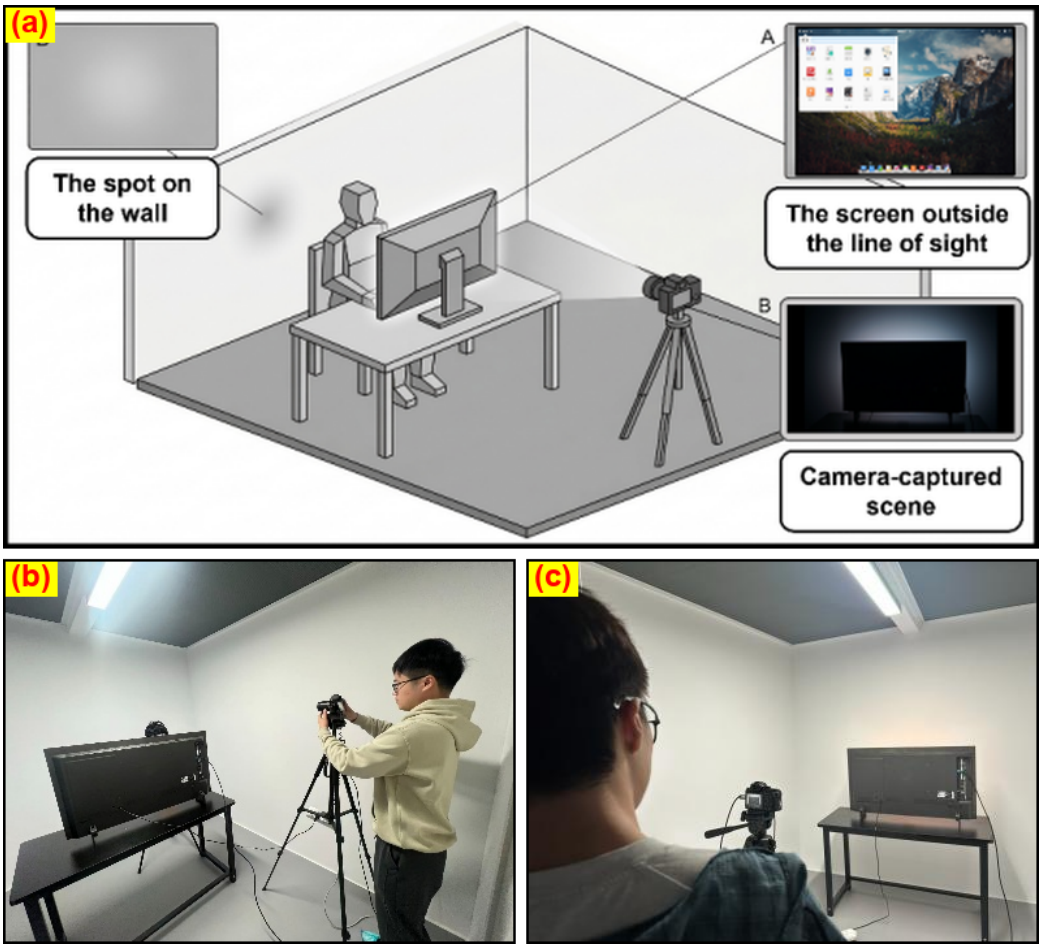

Figure A1: Supplementary views of the computer-screen acquisition scene. (a) Schematic of the hidden display, diffuse relay wall, and camera-side observation path. (b) Oblique view of the display–wall–camera arrangement. (c) View from behind the camera toward the rear of the display and the illuminated wall.

We summarize the indirect observation process as

$$\mathbf{X} = \mathcal{X}(\mathbf{Y}; \mathbf{R}_{\text{wall}}, \ell) + \mathbf{N}. \tag{21}$$

Here, $\mathcal{I} = [0, 1]$ is the normalized image-value domain, B is the batch axis, C_x and C_y are the observation and target color-channel axes, and H, W are the common image height and width. The full passive RGB observation is $\mathbf{X} \in \mathcal{I}^{B\times C_x\times H\times W}$, while $\mathbf{Y} \in \mathcal{I}^{B\times C_y\times H\times W}$ is the paired hidden-screen RGB target. The variables $\mathbf{R}_{\text{wall}}$, ℓ, and $\mathbf{N}$ denote relay-surface response, ambient illumination, and residual sensing disturbance, and $\mathcal{X}$ summarizes the indirect image-formation process. At inference, reconstruction uses the observed image, geometric metadata, and learned parameters.

Deterministic preprocessing localizes the wall region from the current observation:

$$\begin{aligned} \lambda_x &= \Gamma(\mathbf{X}), \\ \varpi &= \arg\max_{\iota} \Phi_0(\lambda_x)_\iota, \\ \mathbf{W} &= \Omega(\mathbf{X}, V) = \Phi_7(\mathbf{X}, \varpi, V). \end{aligned} \tag{22}$$

Here, the fixed luminance operator Γ maps the full observation $\mathbf{X}$ to $\lambda_x \in \mathbb{R}^{B\times 1\times H\times W}$. The fixed operator Φ_0 applies a thirty-one by thirty-one local average, and ι ranges over the valid nonblack spatial positions of each sample. The maximum gives one location ϖ in the discrete image domain. The operator Ω extracts and rectifies the wall crop using the localized response and geometric metadata, producing $\mathbf{W} \in \mathcal{I}^{B\times C_x\times H_e\times W_e}$. The metadata $V \in \mathbb{R}^{B\times 4}$ stores the geometric information used for wall-region extraction and output placement. The operators Γ, Φ_0, Ω, and Φ_7 are deterministic.

The valid box specifies the output region and its aspect ratio and selects the region used for evaluation.

A.2 Pairing, Preprocessing, and Evaluation Scope

We train and evaluate category-specific models for Browser, Figure, Game, and Lock. Browser, Figure, and Game each contain 810 training, 90 validation, and 100 test pairs, while Lock contains 891 training, 99 validation, and 270 test pairs. Browser emphasizes page frames, columns, and large color regions; Figure emphasizes regular graphical regions and principal contours; Game emphasizes complex color organization, canvases, and control regions; and Lock emphasizes smooth color tone, natural backgrounds, and salient subjects. We use fixed splits with random seed 42 and no exact duplicate samples across splits. Inputs and targets are converted to RGB, resized with Lanczos interpolation while preserving aspect ratio, and centered on a 512×384 canvas with black padding.

We pair each wall observation with the screen image displayed during acquisition. Figure A2 shows representative input–target strips for the four categories used in this paper. The wall-side inputs retain broad illumination patterns and regional color cues, whereas the paired targets expose the screen layouts that OEPRL must recover. These four categories define the complete dataset scope of the study.

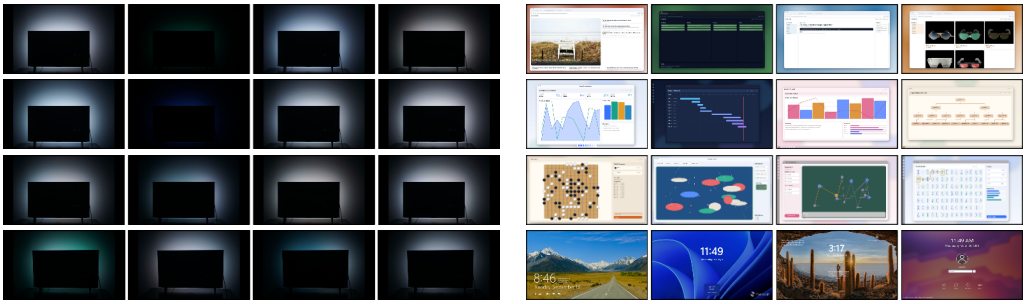

Figure A2: Representative input–target pairs from Browser, Figure, Game, and Lock, ordered from top to bottom. Each row contains four wall observations on the left and their four paired screen targets on the right, in corresponding column order.

For sample ς and metric $\jmath$, we evaluate the reconstruction within the valid screen-content region:

$$\upsilon_{\varsigma,J} = Q_J\left(\widehat{\mathbf{Y}}_\varsigma\big|_{\mathcal{B}(V_\varsigma)}, \mathbf{Y}_\varsigma\big|_{\mathcal{B}(V_\varsigma)}\right). \tag{23}$$

Here, $\widehat{\mathbf{Y}}_\varsigma \in \mathcal{I}^{C_y\times H\times W}$ is the reconstruction for sample ς, $\mathbf{Y}_\varsigma$ is its paired target in the same domain, and the fixed operator $\mathcal{B}$ maps metadata V_ς to the valid screen-content region. The metric operator Q_J returns LPIPS, SSIM, or PSNR, and $\upsilon_{\varsigma,J} \in \mathbb{R}$ is the resulting evaluation value. Lower LPIPS is preferred Zhang et al. (2018), whereas higher SSIM and PSNR are preferred Wang et al. (2004); Huynh-Thu & Ghanbari (2008). For each sample, we compare the reconstruction with its paired target within the valid screen-content region and aggregate the metric values at the dataset level.

We select checkpoints by validation LPIPS. Differences no greater than 0.001 are treated as ties and resolved by SSIM, PSNR, and the earlier epoch, in that order. The selected checkpoint is then evaluated on the test set. All methods share the same pairings, fixed splits, canvas size, valid regions, selection procedure, and evaluation protocol.

B Mechanism and Formula Derivations

B.1 Reliability-Calibrated Optical Evidence and Tokenization

The prepared wall crop supplies RCER's global and local optical evidence. RCER forms a fixed multiscale decomposition before any learned global or local mapping:

$$\begin{aligned}\mathbf{W}^\circ &= \mathrm{clip}_{\mathcal{I}}(\mathbf{W}),\\ \mathbf{E} &= [\mathbf{W}^\circ, \Phi_{31}(\mathbf{W}^\circ), \mathbf{W}^\circ - \Phi_{31}(\mathbf{W}^\circ), \Gamma(\mathbf{W}^\circ), \Phi_{31}(\Gamma(\mathbf{W}^\circ))] \in \mathbb{R}^{B\times 11\times H_e\times W_e}.\end{aligned} \tag{24}$$

Here, $\mathbf{W}$ is the observation-derived crop defined in Appendix A.1. Componentwise clipping produces $\mathbf{W}^\circ \in \mathcal{I}^{B\times C_x\times H_e\times W_e}$, and $\mathbf{E}$ is the eleven-channel evidence tensor. The fixed thirty-one by thirty-one low-pass operator Φ_{31} preserves broad color and luminance information, while the fixed luminance operator Γ isolates intensity structure. The concatenation contains raw RGB, low-pass RGB, RGB residual, luminance, and low-pass luminance with channel counts of three, three, three, one, and one. All terms are deterministic functions of $\mathbf{W}$.

Exposure and contrast statistics are measured from the wall luminance and grouped into the reliability descriptor used by the prompt pathway:

$$\begin{aligned}\lambda_w &= \Gamma(\mathbf{W}^\circ), & \rho^{\mathrm{over}} &= \mathrm{mean}\,\mathbf{1}[\lambda_w > 0.92],\\ \rho^{\mathrm{under}} &= \mathrm{mean}\,\mathbf{1}[\lambda_w < 0.04], & \sigma_\lambda &= \mathrm{std}(\lambda_w),\\ \rho^{\mathrm{flat}} &= \mathrm{clip}\left(\frac{0.12-\sigma_\lambda}{0.12}, 0, 1\right), & \boldsymbol{\rho} &= \mathcal{F}_1(\rho^{\mathrm{over}}, \rho^{\mathrm{under}}, \rho^{\mathrm{flat}}).\end{aligned} \tag{25}$$

Here, $\lambda_w \in \mathbb{R}^{B\times 1\times H_e\times W_e}$ is wall luminance. The scalars $\rho^{\mathrm{over}}, \rho^{\mathrm{under}}, \sigma_\lambda, \rho^{\mathrm{flat}} \in \mathbb{R}^{B\times 1}$ respectively denote the per-sample overexposure ratio, underexposure ratio, luminance standard deviation, and clipped low-contrast score. The indicator, mean, standard-deviation, and clipping operators are fixed, as are the displayed threshold values. First, Γ forms luminance from $\mathbf{W}^\circ$; next, the fixed statistics summarize exposure and contrast; finally, the deterministic map $\mathcal{F}_1$ produces descriptor $\boldsymbol{\rho} \in \mathbb{R}^{B\times D_b}$ for the color and structural residual subspaces. Every quantity is computed from $\mathbf{W}$.

The global evidence encoder and learned expert mixture produce a calibrated prompt:

$$\begin{aligned}\mathbf{g} &= \Psi_g(\mathbf{E};\theta_1),\\ a &= \mathcal{M}(\mathbf{g};\theta_2),\\ r &= \sum_{\varphi\in J} a_\varphi u_\varphi,\\ \mathbf{p} &= \mathbf{g} + \mathcal{S}(r, \boldsymbol{\rho};\theta_3).\end{aligned} \tag{26}$$

Here, learned encoder Ψ_g with parameters θ_1 first maps $\mathbf{E}$ to global optical code $\mathbf{g} \in \mathbb{R}^{B\times D}$. Learned mixer $\mathcal{M}$ with parameters θ_2 next produces nonnegative weights $a \in \mathbb{R}^{B\times|J|}$ that sum to one over expert set J. The index φ identifies one learned expert vector $u_\varphi \in \mathbb{R}^D$, and their weighted sum is residual $r \in \mathbb{R}^{B\times D}$. Learned calibration map $\mathcal{S}$ with parameters θ_3 then uses observation-derived $\boldsymbol{\rho}$ to rescale residual subspaces and produces prompt $\mathbf{p} \in \mathbb{R}^{B\times D}$. The three parameter sets and expert vectors are learned; $\mathbf{E}$ and $\boldsymbol{\rho}$ are observation-derived.

The calibrated prompt applies a learned bounded channel-affine transformation at each conditioned encoder stage:

$$\widetilde{h} = h \otimes \left[1 + \alpha_7 \tanh\big(\Psi_{11}(\mathbf{p};\theta_{20})\big)\right] + \alpha_7 \tanh\big(\Psi_{12}(\mathbf{p};\theta_{20})\big). \tag{27}$$

Here, $h \in \mathbb{R}^{B\times C_h\times H_h\times W_h}$ is an encoder activation computed from the observation. A learned affine projection with stage-specific parameters θ_{20} is split into channel maps Ψ_{11} and Ψ_{12}, each returning a vector in $\mathbb{R}^{B\times C_h}$. Their hyperbolic tangents are multiplied by the scale $\alpha_7 = 0.08$, broadcast over H_h, W_h, and applied multiplicatively and additively to produce conditioned activation $\widetilde{h}$. The operator $\otimes$ denotes broadcast elementwise multiplication.

The local scorer pools evidence to the candidate grid and combines fixed optical cues with a bounded learned residual:

$$\begin{aligned} \bar{\mathbf{E}} &= \mathcal{P}_{8\times8}(\mathbf{E}), \\ \bar{s} &= \mathcal{F}_2(\bar{\mathbf{E}}) + \alpha_0 \tanh\big(\Delta_s(\bar{\mathbf{E}};\theta_4)\big), \\ s &= \mathrm{vec}(\bar{s}). \end{aligned} \tag{28}$$

Here, fixed adaptive average operator $\mathcal{P}_{8\times8}$ first maps $\mathbf{E}$ to pooled evidence $\bar{\mathbf{E}} \in \mathbb{R}^{B\times11\times8\times8}$. The fixed score operator $\mathcal{F}_2$ combines channelwise mean absolute RGB-residual magnitude, local root-mean-square luminance, and binary valid-exposure evidence. We use weights of 0.55, 0.35, and 0.10 and gate their sum by valid exposure. Learned residual map Δ_s with parameters θ_4 contributes a bounded field in the same domain, and $\alpha_0 = 0.20$. Their sum produces $\bar{s} \in \mathbb{R}^{B\times1\times8\times8}$, and vectorization gives $s \in \mathbb{R}^{B\times64}$.

Selection preserves regional values, coordinates, and normalized scores for later prediction:

$$\begin{aligned} \mathcal{K} &= \mathrm{TopK}(s), \\ t_j &= \Pi_t([\bar{\mathbf{E}}_j, \boldsymbol{\pi}_j];\theta_5) \in \mathbb{R}^{D_t}, \\ \varepsilon_{\mathrm{den}} &= 10^{-6}, \\ \omega_j &= \frac{s_j}{\max(\max_{k\in\mathcal{K}} s_k, \varepsilon_{\mathrm{den}})}, \quad j \in \mathcal{K}. \end{aligned} \tag{29}$$

Here, top selection produces index set $\mathcal{K}$ with sixteen elements. For selected wall-region index $j \in \mathcal{K}$, pooled evidence $\bar{\mathbf{E}}_j \in \mathbb{R}^{11}$ and normalized coordinate $\boldsymbol{\pi}_j \in \mathbb{R}^2$ are gathered and concatenated. Learned projection Π_t with parameters θ_5 maps that vector to token $t_j \in \mathbb{R}^{D_t}$, where $D_t = 64$. The scalar s_j is its regional score, and safeguard $\varepsilon_{\mathrm{den}}$ lower-bounds the normalization denominator to produce the signed evidence weight ω_j. Stacking these scalars yields $\omega \in \mathbb{R}^{B\times16\times1}$, whose singleton axis broadcasts across each token.

Together, the calibrated prompt, global code, and positioned tokens provide the reconstruction pathway with complementary forms of wall evidence. RCER passes $\mathbf{p}$ to the encoder, $\mathbf{g}$ to the middle latent operator, and (t, ω) to the two predictive corrections.

B.2 Middle Latent Transport

After prompt-conditioned encoding, the middle feature is normalized and decomposed into complementary low-frequency and high-frequency components:

$$\begin{aligned} \bar{z} &= \mathcal{N}_z(\mathbf{Z}^{(0)}; \theta_{21}), \\ z_l &= \Phi_5(\bar{z}), \\ z_h &= \bar{z} - z_l. \end{aligned} \tag{30}$$

Here, $\mathbf{Z}^{(0)} \in \mathbb{R}^{B\times C\times H_z\times W_z}$ is the middle activation. The operator $\mathcal{N}_z$ computes one-group normalization and applies learned channel-affine parameters θ_{21}, producing $\bar{z}$ in the same domain. The five by five local average Φ_5 then produces low-frequency component z_l, and subtraction produces complementary high-frequency residual z_h.

The global optical code provides separate learned gates for the two components:

$$\begin{aligned} (\beta_l, \beta_h) &= \Psi_\beta(\mathbf{g}; \theta_6), \\ \tilde{z}_l &= \mathcal{B}_{\text{lo}}\big((1 + \alpha_1 \tanh \beta_l) \otimes z_l; \theta_7\big), \\ \tilde{z}_h &= \mathcal{B}_{\text{hi}}\big((1 + \alpha_2 \tanh \beta_h) \otimes z_h; \theta_8\big). \end{aligned} \tag{31}$$

Here, learned map Ψ_β with parameters θ_6 maps global code $\mathbf{g}$ to channel gates $\beta_l, \beta_h \in \mathbb{R}^{B\times C}$. The gates are broadcast over spatial locations through $\otimes$ and applied to z_l and z_h before branch processing. Learned branch maps $\mathcal{B}_{\text{lo}}$ and $\mathcal{B}_{\text{hi}}$, parameterized by θ_7 and θ_8, then apply spatial filtering, pointwise transformation, and nonlinear activation to produce $\tilde{z}_l, \tilde{z}_h \in \mathbb{R}^{B\times C\times H_z\times W_z}$. The fixed scales α_1 and α_2 are 0.08 and 0.06.

The branch sum is mapped to a bounded residual before being mixed into the original middle feature:

$$\begin{aligned} \delta_1 &= \alpha_3 \tanh\big(\Delta_z(\tilde{z}_l + \tilde{z}_h; \theta_9)\big), \\ \mathbf{Z}^{(1)} &= \mathbf{Z}^{(0)} + \sigma(\mu_0)\delta_1. \end{aligned} \tag{32}$$

Here, learned map Δ_z with parameters θ_9 fuses $\tilde{z}_l$ and $\tilde{z}_h$. The hyperbolic tangent and scale $\alpha_3 = 0.05$ produce bounded residual $\delta_1 \in \mathbb{R}^{B\times C\times H_z\times W_z}$. Learned scalar $\mu_0 \in \mathbb{R}$ controls residual mixing through logistic function σ, yielding $\mathbf{Z}^{(1)}$ in the same domain as $\mathbf{Z}^{(0)}$.

The latent operator carries global optical context into complementary low- and high-frequency feature branches before decoding.

B.3 Sequential Global and Local Predictive Corrections

At the deepest decoder stage, OPC predicts an observation-derived global target built from the selected wall tokens:

$$\begin{aligned} \varepsilon_2 &= 10^{-4}, \\ \hat{o} &= \Psi_f(\Phi_4(\mathbf{F}^{(0)}); \theta_{10}), \\ o &= \Psi_o\left(\frac{\sum_{j\in\mathcal{K}} \omega_j t_j}{\max(\sum_{j\in\mathcal{K}} \omega_j, \varepsilon_2)}; \theta_{11}\right), \\ \eta &= o - \hat{o}. \end{aligned} \tag{33}$$

Here, $\mathbf{F}^{(0)} \in \mathbb{R}^{B\times C_d\times H_d\times W_d}$ is the decoder feature before correction. Global pooling Φ_4 removes its spatial axes, and learned predictor Ψ_f with parameters θ_{10} produces $\hat{o} \in \mathbb{R}^{B\times D_o}$. For selected wall-region index $j \in \mathcal{K}$, token $t_j \in \mathbb{R}^{D_t}$ is weighted by signed scalar ω_j. Summation and lower bound ε_2 form their aggregate, which learned projection Ψ_o with parameters θ_{11} maps to target $o \in \mathbb{R}^{B\times D_o}$. Subtraction produces global error $\eta \in \mathbb{R}^{B\times D_o}$. The OPC target o is projected from the aggregated local tokens, while the global code $\mathbf{g}$ conditions the latent operator.

The global error modulates the decoder feature and produces the first bounded correction:

$$
\begin{aligned}
(\kappa, \nu) &= \Psi_\eta(\eta; \theta_{12}), \\
\mathbf{S}_g &= \mathbf{F}^{(0)} \otimes (1 + \alpha_4 \tanh \kappa) + \alpha_4 \tanh \nu, \\
\delta_2 &= \alpha_5 \tanh\big(\Delta_{\mathrm{g}}(\mathbf{S}_g; \theta_{13})\big), \\
\mathbf{F}^{(1)} &= \mathbf{F}^{(0)} + \sigma(\mu_1)\sigma(\Psi_c(\eta; \theta_{14})) \otimes \delta_2.
\end{aligned}
\tag{34}
$$

Here, learned map Ψ_η with parameters θ_{12} produces channel modulation vectors $\kappa, \nu \in \mathbb{R}^{B \times C_d}$ from η. Broadcasting through $\otimes$ with scale $\alpha_4 = 0.08$ forms $\mathbf{S}_g \in \mathbb{R}^{B \times C_d \times H_d \times W_d}$. Learned spatial map Δ_{g} with parameters θ_{13} then produces residual δ_2 in the same domain, bounded by the hyperbolic tangent and scale $\alpha_5 = 0.03$. Learned map Ψ_c with parameters θ_{14} produces a channel gate, and learned scalar $\mu_1 \in \mathbb{R}$ controls residual mixing. The final sum yields $\mathbf{F}^{(1)}$ in the same domain as $\mathbf{F}^{(0)}$.

OEA operates on the globally corrected feature $\mathbf{F}^{(1)}$ and compares normalized screen and wall tokens with mean squared distance:

$$
\begin{aligned}
q_i &= \Pi_2(\mathcal{P}_{4\times4}(\mathbf{F}^{(1)})_i; \theta_{15}), \qquad \tilde{t}_j = \omega_j t_j, \qquad \varepsilon_{\mathrm{norm}} = 10^{-12}, \\
\bar{q}_i &= \frac{q_i}{\max(\|q_i\|_2, \varepsilon_{\mathrm{norm}})}, \qquad \bar{t}_j = \frac{\tilde{t}_j}{\max(\|\tilde{t}_j\|_2, \varepsilon_{\mathrm{norm}})}, \\
d_{i,j} &= \frac{1}{D_t}\|\bar{q}_i - \bar{t}_j\|_2^2.
\end{aligned}
\tag{35}
$$

Adaptive average pooling $\mathcal{P}_{4\times4}$ maps $\mathbf{F}^{(1)}$ to a four by four screen-region grid, so $N_s = 16$. Learned projection Π_2 with parameters θ_{15} produces screen token $q_i \in \mathbb{R}^{D_t}$. Selected wall-region index j identifies token $t_j \in \mathbb{R}^{D_t}$ and signed score ω_j, whose product is $\tilde{t}_j \in \mathbb{R}^{D_t}$. The positive constant $\varepsilon_{\mathrm{norm}} = 10^{-12}$ safeguards the Euclidean-norm denominator. The mean squared distance is scalar $d_{i,j} \in \mathbb{R}_{\geq 0}$.

The learned temperature parameter is lower bounded before the distances are converted to an affinity:

$$
\begin{aligned}
\varepsilon_3 &= 0.02, \\
\bar{\tau} &= \max(\tau, \varepsilon_3), \\
A^{(0)}_{i,j} &= \exp(-d_{i,j}/\bar{\tau}).
\end{aligned}
\tag{36}
$$

Here, $\tau \in \mathbb{R}$ is a learned scalar. Safeguard ε_3 and the maximum produce positive effective temperature $\bar{\tau}$, and the exponential maps distances to initial affinity $A^{(0)} \in \mathbb{R}_+^{B \times N_s \times N}$. The dimensions N_s and N are the screen-token and selected wall-token counts.

The affinity is alternately normalized across rows and columns and then receives the final row normalization used for readout:

$$
\begin{aligned}
A^{(k_{\mathrm{it}}+\frac{1}{2})}_{i,j} &= \frac{A^{(k_{\mathrm{it}})}_{i,j}}{\max(\sum_{j'} A^{(k_{\mathrm{it}})}_{i,j'}, \varepsilon_{\mathrm{den}})}, \\
A^{(k_{\mathrm{it}}+1)}_{i,j} &= \frac{A^{(k_{\mathrm{it}}+\frac{1}{2})}_{i,j}}{\max(\sum_{i'} A^{(k_{\mathrm{it}}+\frac{1}{2})}_{i',j}, \varepsilon_{\mathrm{den}})}, \qquad k_{\mathrm{it}} \in \{0, \ldots, R-1\}, \\
A_{i,j} &= \frac{A^{(R)}_{i,j}}{\max(\sum_{j'} A^{(R)}_{i,j'}, \varepsilon_{\mathrm{den}})}.
\end{aligned}
\tag{37}
$$

Here, k_{it} indexes the alternating steps, and we perform $R = 3$ alternating normalization steps. The indices i and j retain their screen-region and selected wall-region meanings, and $\varepsilon_{\mathrm{den}} = 10^{-6}$ is the safeguard defined for score normalization. The first line performs row normalization over wall

tokens; the second performs column normalization over screen tokens; and the final line performs the row normalization used for readout. These operations implement Sinkhorn-style soft matching Mena et al. (2018).

The normalized plan aggregates wall evidence and forms a local token error:

$$\begin{aligned} \chi_i &= \sum_j A_{i,j} \tilde{t}_j, \\ \xi_i &= \chi_i - q_i. \end{aligned} \tag{38}$$

Weighted aggregation uses row $A_{i,:}$ and wall tokens $\tilde{t}_j$ to produce aligned target $\chi_i \in \mathbb{R}^{D_t}$ for screen-region index i. Subtraction then produces local token error $\xi_i \in \mathbb{R}^{D_t}$.

The local errors are projected to the decoder lattice and applied as the second bounded update:

$$\begin{aligned} \vartheta &= \Pi_3(\xi; \theta_{16}), \\ m_0 &= \mathrm{reshape}(\vartheta^{\mathsf{T}}), \\ m &= \Phi_6(m_0), \\ \gamma_2 &= \sigma\big(\Psi_1(m; \theta_{18})\big), \\ \delta_3 &= \alpha_6 \tanh\big(\Delta_1(\tanh m; \theta_{17})\big), \\ \mathbf{F}^{(2)} &= \mathbf{F}^{(1)} + \sigma(\mu_2)\gamma_2 \otimes \delta_3. \end{aligned} \tag{39}$$

Here, $\xi \in \mathbb{R}^{B\times N_s \times D_t}$ stacks the local errors. Learned normalization and linear projection Π_3 with parameters θ_{16} produce $\vartheta \in \mathbb{R}^{B\times N_s \times C_d}$. Transposition and reshaping produce the four by four channel-first lattice $m_0 \in \mathbb{R}^{B\times C_d \times 4\times 4}$, and Φ_6 bilinearly interpolates it to $m \in \mathbb{R}^{B\times C_d \times H_d \times W_d}$. Learned maps Ψ_1 and Δ_1 produce the spatial gate and bounded correction with scale $\alpha_6 = 0.03$. Learned scalar $\mu_2 \in \mathbb{R}$ controls residual mixing, and the final line applies the correction to $\mathbf{F}^{(1)}$ so that OEA follows OPC sequentially.

The remaining decoder and residual head produce the RGB reconstruction:

$$\widehat{\mathbf{Y}} = \mathrm{clip}\big(\mathbf{X} + \Psi_{10}(\mathbf{F}^{(2)}, \mathbf{X}, \mathbf{p}; \theta_{19})\big). \tag{40}$$

Here, learned operator Ψ_{10} with parameters θ_{19} represents the remaining decoder and RGB residual head. It maps corrected feature $\mathbf{F}^{(2)}$, skip information derived from $\mathbf{X}$, and prompt $\mathbf{p}$ to an RGB residual in $\mathbb{R}^{B\times C_y \times H\times W}$. Addition combines that residual with observation $\mathbf{X}$, and clipping produces reconstruction $\widehat{\mathbf{Y}} \in \mathcal{I}^{B\times C_y \times H\times W}$.

We train OEPRL end to end with an image objective combining ℓ_1, Laplacian, and LPIPS terms with weights 1, 0.05, and 0.02. A frozen InstructIR teacher initialized from the checkpoint used to initialize the student backbone receives the same wall observation and region metadata as the student and supplies output-level ℓ_1 and LPIPS constraints whose weights decay from 0.04 to 0.015 and from 0.004 to 0.0015, respectively. Training uses AdamW with a base learning rate of 4×10^{-5}, weight decay 10^{-4}, mixed precision, gradient clipping at 1.0, and random seed 42. The global and regional prediction errors provide observation-derived feedback within the forward reconstruction pathway. The complete pathway proceeds from wall-evidence formation and prompt-conditioned encoding to latent transport, sequential global and regional correction, and RGB reconstruction. The same observed optical evidence thus informs both feature formation and the corrections that produce the hidden-screen estimate.

C Additional Experimental Results

C.1 Internal Component Ablations

The internal ablations test where each operation contributes along OEPRL's path from wall-evidence representation to reconstruction correction. EAT and LTO variants test how local selection and

latent transport organize wall evidence, while OPC and OEA variants test how global prediction and regional correspondence carry that evidence into the decoder. Each variant is compared with the complete model recorded within the same ablation group.

Table A1: EAT and LTO removal and replacement ablations. The OEPRL row is the complete-model reference recorded within this ablation group.

Method	Source	Browser			Figure			Game			Lock		
		LPIPS↓	SSIM↑	PSNR↑	LPIPS↓	SSIM↑	PSNR↑	LPIPS↓	SSIM↑	PSNR↑	LPIPS↓	SSIM↑	PSNR↑
EAT Variants													
w/o EAT	–	**0.4513**	**0.7359**	**19.12**	**0.5866**	**0.6935**	**18.99**	**0.5612**	**0.6649**	**18.21**	**0.6401**	**0.5999**	**16.75**
EAT→Adaptive Token Sampling	ECCV'22	0.4525	0.7353	19.08	0.5879	0.6928	18.95	0.5626	0.6641	18.17	0.6416	0.5990	16.70
EAT→TokenLearner	NeurIPS'21	0.4529	0.7347	19.07	0.5884	0.6921	18.93	0.5631	0.6633	18.14	0.6422	0.5982	16.68
LTO Variants													
w/o LTO	–	0.4552	0.7330	19.01	0.5909	0.6902	18.87	0.5659	0.6612	18.08	0.6452	0.5959	16.61
LTO→NAFBlock	ECCV'22	0.4579	0.7305	18.90	0.5939	0.6874	18.75	0.5692	0.6582	17.95	0.6488	0.5925	16.46
LTO→Restormer-MDTA	CVPR'22	0.4590	0.7296	18.87	0.5952	0.6865	18.71	0.5706	0.6572	17.90	0.6504	0.5915	16.41
OEPRL	–	**0.4457**	**0.7408**	**19.28**	**0.5804**	**0.6989**	**19.17**	**0.5543**	**0.6708**	**18.41**	**0.6326**	**0.6063**	**16.97**

The representation ablations in Table A1 trace the gain through evidence selection and latent transport. Removing EAT or LTO lowers quality across all four categories, and the complete model leads their replacement variants. On Figure, removing LTO produces the largest LPIPS increase among the four internal removals, highlighting the value of using the observed wall response to condition complementary low- and high-frequency features. The next comparison follows this organized evidence into the decoder's global and regional corrections.

Table A2: OPC and OEA removal and replacement ablations. The OEPRL row is the complete-model reference recorded within this ablation group.

Method	Source	Browser			Figure			Game			Lock		
		LPIPS↓	SSIM↑	PSNR↑	LPIPS↓	SSIM↑	PSNR↑	LPIPS↓	SSIM↑	PSNR↑	LPIPS↓	SSIM↑	PSNR↑
OPC Variants													
w/o OPC	–	**0.4518**	**0.7356**	**19.10**	**0.5872**	**0.6931**	**18.97**	**0.5618**	**0.6644**	**18.19**	**0.6408**	**0.5994**	**16.73**
OPC→Restormer-MDTA	CVPR'22	0.4567	0.7316	18.96	0.5926	0.6887	18.81	0.5678	0.6596	18.01	0.6473	0.5941	16.53
OPC→PromptIR	NeurIPS'23	0.4574	0.7311	18.92	0.5934	0.6881	18.77	0.5686	0.6589	17.97	0.6482	0.5934	16.49
OEA Variants													
w/o OEA	–	0.4527	0.7350	19.07	0.5882	0.6924	18.94	0.5629	0.6637	18.16	0.6420	0.5985	16.69
OEA→LoFTR	CVPR'21	0.4535	0.7344	19.05	0.5890	0.6918	18.91	0.5638	0.6630	18.12	0.6429	0.5978	16.65
OEA→LightGlue	ICCV'23	0.4581	0.7305	18.89	0.5942	0.6875	18.74	0.5695	0.6583	17.93	0.6492	0.5927	16.45
OEPRL	–	**0.4457**	**0.7408**	**19.28**	**0.5804**	**0.6989**	**19.17**	**0.5543**	**0.6708**	**18.41**	**0.6326**	**0.6063**	**16.97**

The correction ablations in Table A2 complete the two-stage analysis. Removing OPC or OEA lowers quality across all four categories, and OEPRL remains strongest among the removal and replacement variants. LoFTR establishes coarse-to-fine dense image correspondences Sun et al. (2021), while LightGlue matches sparse local features across images Lindenberger et al. (2023). OEA gathers evidence from multiple wall regions for each screen region and converts the resulting discrepancy into decoder correction, giving OEPRL 16.97 dB PSNR on Lock compared with 16.65 dB and 16.45 dB for the LoFTR- and LightGlue-based replacement variants, respectively. OEPRL achieves the strongest reconstruction by coupling wall-evidence selection and alignment with observation-conditioned latent features.

C.2 Spatial Evidence Intervention

Spatial intervention tests the premise behind positioned optical evidence: a diffuse wall pattern carries reconstruction support through localized regions whose contributions remain spatially organized. We apply local occlusions at nine positions arranged on a 3×3 grid and compare the resulting reconstructions with the complete-observation output.

Wall regions differ in their influence on the reconstructed screen. Occluding the upper-middle or middle-right wall region introduces pronounced fragmentation into the recovered dark screen region, while occluding the central dark area has a much smaller visual effect. Useful support is therefore distributed unevenly across the surrounding wall illumination.

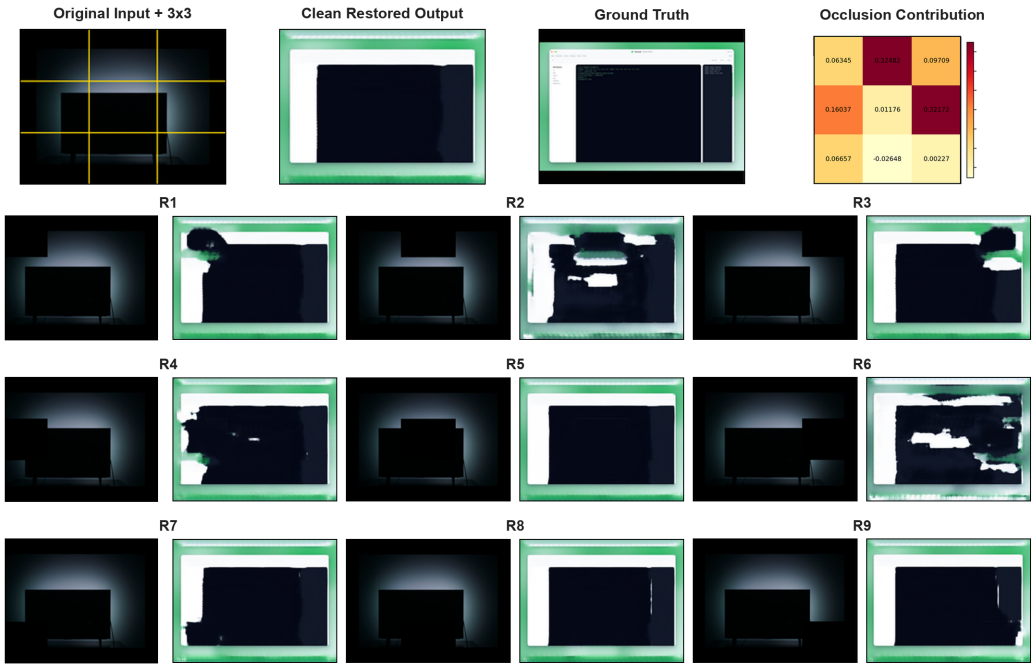

Figure A3: Nine-region intervention for spatially positioned wall evidence. Local occlusions are placed at nine positions on a fixed 3×3 grid; the first row contains the input, reconstruction, target, and contribution heat map, and the remaining rows show the nine local occlusions. Regions that produce larger output changes are the regions whose optical evidence most strongly influences the reconstruction.

This finding gives positioned evidence a concrete role: the representation should retain both the local optical response and its location. We next test whether EAT concentrates its limited tokens on this useful support.

C.3 Evidence Selection Test

Adaptive Token Sampling scores and samples informative tokens for visual recognition Fayyaz et al. (2022), while TokenLearner learns a compact set of visual tokens Ryoo et al. (2021). EAT retains 16 optically scored wall regions with their positions, giving OEPRL a Browser LPIPS of 0.4457 versus 0.4525 with Adaptive Token Sampling and 0.4529 with TokenLearner in our replacement test (Table A1). To test evidence concentration, we apply deletion and keep-only interventions to low-score, random, matched-random, and EAT Top-K regions under a fixed encoder, decoder, and evaluation setting.

Table A3: Evidence concentration test for Evidence-Adaptive Tokenization (EAT). Each selection rule is evaluated in deletion and keep-only modes under the same trained model and evaluation setting. Signed changes are perturbed minus clean values, and the PSNR drop is clean minus perturbed PSNR. The EAT Top-K row gives the largest deletion change and the strongest keep-only LPIPS and SSIM, showing that the selected wall regions carry concentrated reconstruction evidence. Mean PSNR drop is the unweighted mean across the four content categories. The EAT row is highlighted to identify the proposed selection rule.

Selection rule	Deletion change			Keep-only performance			PSNR drop by dataset (dB)				Mean drop
	LPIPSΔ	SSIMΔ	PSNRΔ	LPIPS$\downarrow$	SSIM$\uparrow$	PSNR$\uparrow$	Browser	Figure	Game	Lock	
Low-score	0.0227	-0.0265	-1.5282	0.6663	0.5773	14.4875	2.2083	0.6162	1.6892	1.5993	1.5282
Random	0.0371	-0.0451	-1.7983	0.6448	0.5946	15.1515	3.4943	0.7489	2.0665	0.8834	1.7983
Matched Random	0.0400	-0.0427	-1.5035	0.6454	0.5937	14.9430	3.2099	0.5545	1.3544	0.8952	1.5035
EAT Top-K	**0.0606**	**-0.0659**	**-2.4936**	**0.6364**	**0.6025**	15.1473	**4.6522**	**0.9404**	**2.6361**	**1.7459**	**2.4936**

The deletion and keep-only tests identify the same useful wall support from opposite directions. Removing EAT-selected regions produces the largest mean PSNR drop, 2.4936 dB, together with the largest perceptual and structural changes; retaining them alone gives the best LPIPS and SSIM

among the selection rules. The selected regions therefore contribute strongly to the complete reconstruction and preserve useful screen information on their own. Residual magnitude captures local variation, luminance describes regional brightness, valid exposure favors usable measurements, and the learned term adapts their combination. EAT therefore selects regions according to the optical information they can contribute to hidden-screen recovery.

C.4 Reliability-Gated Evidence Stability

The next test examines whether RCER's reliability-calibrated evidence representation retains its reconstruction advantage as low-confidence wall regions become progressively corrupted. We test this mechanism by injecting heteroscedastic noise into low-confidence evidence and sweeping its scale s under a shared U-Net decoder.

Table A4: Stability under heteroscedastic corruption of low-confidence wall evidence. All variants use the same U-Net encoder–decoder, data, reconstruction head, and evaluation procedure, with the representation block as the controlled variable. Noise with scale s is injected into low-confidence regions. The proposed representation leads LPIPS, SSIM, and PSNR at every tested level; red and blue denote the best and second-best values.

Method	Source	Clean			s = 0.08			s = 0.12			s = 0.16			s = 0.20		
		LPIPS↓	SSIM↑	PSNR↑	LPIPS↓	SSIM↑	PSNR↑	LPIPS↓	SSIM↑	PSNR↑	LPIPS↓	SSIM↑	PSNR↑	LPIPS↓	SSIM↑	PSNR↑
U-Net + NAFBlock	ECCV'22	0.6919	0.6256	16.667	0.7205	0.5692	14.432	0.7551	0.5305	12.091	0.7765	0.5053	10.314	0.7824	0.4920	9.596
U-Net + Restormer MDTA	CVPR'22	0.6967	0.6100	15.749	0.7406	0.5333	12.229	0.7598	0.5138	10.955	0.7755	0.4993	10.218	0.7859	0.4851	9.661
U-Net + PromptIR Block	NeurIPS'23	0.6881	**0.6273**	**16.742**	**0.7003**	**0.5854**	**15.404**	**0.7227**	**0.5394**	**13.592**	**0.7454**	0.4957	**11.859**	**0.7532**	0.4739	**10.613**
U-Net + MambaIR-style SSM	ECCV'24	0.6838	0.6262	16.576	0.7257	0.5457	13.257	0.7486	0.4993	10.638	0.7681	0.4698	9.598	0.7936	0.4435	8.933
U-Net + RCER	**Ours**	**0.6709**	**0.6280**	**16.824**	**0.6859**	**0.5950**	**15.527**	**0.7047**	**0.5640**	**14.054**	**0.7258**	**0.5237**	**12.248**	**0.7440**	**0.4977**	**10.983**

PromptIR conditions restoration on degradation-aware prompts Potlapalli et al. (2023), while MambaIR combines state-space modeling with local enhancement and channel attention Guo et al. (2024a). With the same U-Net encoder–decoder and reconstruction head, RCER's calibrated wall representation leads all three metrics at every tested level and reaches 10.983 dB PSNR at $s = 0.20$, compared with 10.613 dB for the PromptIR block and 8.933 dB for the MambaIR-style state-space module (Table A4). Together with the selection test, this connects the reconstruction gain to two complementary operations: concentrating useful wall regions and representing their optical cues effectively under corruption. The next visualization follows these organized cues through latent conditioning, global prediction, and regional alignment into the recovered screen.

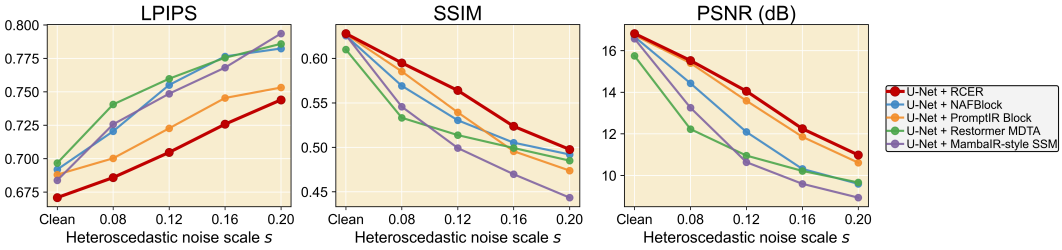

Figure A4: Metric curves corresponding to Table A4. As heteroscedastic noise in low-confidence evidence increases, the proposed representation maintains the lowest LPIPS and the highest SSIM and PSNR across all tested levels. This consistent lead supports the stability of evidence-aware representation under the shared U-Net decoder and evaluation setting.

C.5 Feature Evolution Through OEPRL

Feature evolution exposes how the calibrated evidence is converted into a screen reconstruction. The visualization follows each sample from EAT tokens through low/high latent transport, global OPC correction, local OEA correction, and final RGB recovery.

Figure A5 connects the selected wall evidence to the recovered screen in one sequence. EAT locates the retained optical support, and the low/high panels show the complementary latent branches that receive global conditioning. OPC then uses a global evidence discrepancy to update the decoder, after which OEA supplies regional corrections to the updated state. By the RGB output, these wall-derived cues support browser layout, graphical regions, game-panel organization, and the foreground–background structure of the lock screen. The sequence connects the optical evidence selected at the wall to the screen content that becomes recoverable.

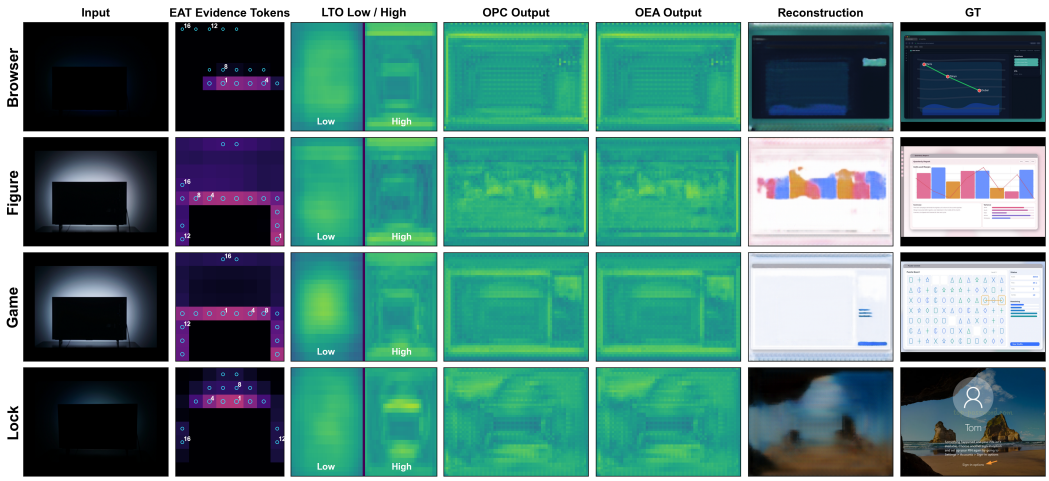

Figure A5: Evidence and feature evolution through OEPRL. Columns show the input, selected EAT locations, low- and high-frequency latent features, OPC and OEA outputs, reconstruction, and ground truth. Each feature panel shows the root-mean-square channel energy normalized by that tensor's RMS scale and displayed on a shared logarithmic range. Rows show Browser, Figure, Game, and Lock from top to bottom.

C.6 Training Resource Profile

Table A5 compares training time, energy, and peak memory under a fixed workload. OEPRL uses 81.4 s, 4.168 Wh, and 7.858 GiB.

Table A5: Training time, energy, and peak memory of the compared reconstruction models under a fixed workload of three epochs on 240 training pairs, with 32 validation pairs, 32 test pairs, and effective batch size 8.

Method	Source	Time (s) ↓	Energy (Wh) ↓	Peak memory (GiB) ↓
Passive Non-Line-of-Sight Reconstruction				
NLOS-LTM	TIP'25	37.2	1.579	3.972
All-in-One and Universal Image Restoration				
PromptIR	NeurIPS'23	168.6	10.821	11.636
InstructIR	ECCV'24	55.6	2.852	8.446
AdaIR	ICLR'25	282.9	20.814	10.718
FoundIR	ICCV'25	163.9	11.974	11.194
OneRestore	ECCV'24	76.9	4.194	14.069
General-Purpose Image Restoration				
AST	CVPR'24	71.5	4.225	19.415
ConvIR	TPAMI'24	155.1	11.593	13.054
IRNeXt	ICML'23	131.1	9.713	10.907
SFHformer	ECCV'24	173.0	13.162	13.718
Uformer	CVPR'22	64.5	3.731	18.970
MIRNetv2	TPAMI'23	278.8	23.355	15.640
NAFNet	ECCV'22	54.2	2.857	8.704
DeepSN-Net	TPAMI'25	60.7	3.589	9.136
DnCNN	TIP'17	48.6	2.786	7.569
U-Net	MICCAI'15	54.5	2.913	5.909
Related Degradations and Domains				
INFWIDE	TIP'23	290.0	23.707	13.790
MetaWeather	ECCV'24	86.1	3.396	6.431
Retinexformer	ICCV'23	84.0	5.459	19.272
Pixel2Pixel	TPAMI'25	27.9	1.163	2.255
DocRes	CVPR'24	94.2	5.766	12.866
DEA-Net	TIP'24	78.8	5.080	7.538
DehazeFormer	TIP'23	58.7	3.670	12.423
DarkIR	CVPR'25	70.0	3.933	12.472
OEPRL	**Ours**	**81.4**	**4.168**	**7.858**

C.7 BRIGHTNESS REDUCTION

Brightness reduction makes the screen-induced wall pattern fainter. We examine which parts of the hidden screen remain recoverable as this optical evidence weakens.



Figure A6: Representative views of the screen–wall setup under different lighting conditions.

The setup views relate the brightness change to the recorded wall response. The Figure comparison below follows the reconstruction of graphical content across the reduction levels; the Lock comparison then tests whether the same change preserves the organization of natural screen imagery. In both cases, the relevant signal is the light reflected from the wall into the camera.

Table A6: Figure point estimates under increasing brightness reduction. Best and second-best values are highlighted in red and blue, respectively. The corresponding trend is shown in Figure A7.

Method	4%			8%			12%			16%			20%		
	LPIPS↓	SSIM↑	PSNR (dB)↑	LPIPS↓	SSIM↑	PSNR (dB)↑	LPIPS↓	SSIM↑	PSNR (dB)↑	LPIPS↓	SSIM↑	PSNR (dB)↑	LPIPS↓	SSIM↑	PSNR (dB)↑
Passive Non-Line-of-Sight Reconstruction															
NLOS-LTM	0.7331	0.5330	13.57	0.7335	0.5338	13.58	0.7334	0.5350	13.59	0.7361	0.5340	13.49	0.7430	0.5323	13.32
All-in-One and Universal Image Restoration															
InstructIR	0.6338	0.6759	18.09	0.6350	0.6761	18.15	0.6368	0.6762	18.22	0.6392	0.6764	18.27	0.6418	0.6766	18.30
OneRestore	0.7187	0.5709	12.20	0.7199	0.5733	12.26	0.7209	0.5758	12.32	0.7211	0.5786	12.38	0.7215	0.5815	12.42
General-Purpose Image Restoration															
SFHformer	0.7360	0.5778	12.71	0.7358	0.5790	12.71	0.7353	0.5801	12.71	0.7348	0.5813	12.71	0.7343	0.5824	12.71
Uformer	0.6413	0.6069	17.12	0.6407	0.6092	17.20	0.6398	0.6120	17.29	0.6395	0.6150	17.34	**0.6394**	0.6179	17.39
NAFNet	0.6349	0.6344	17.58	0.6349	0.6359	17.67	**0.6361**	0.6382	17.61	**0.6387**	0.6405	17.38	0.6425	0.6422	16.99
DeepSN-Net	0.7093	0.4832	13.65	0.7088	0.4854	13.62	0.7084	0.4872	13.59	0.7083	0.4887	13.54	0.7083	0.4899	13.49
DnCNN	0.6887	0.5509	13.41	0.6891	0.5512	13.41	0.6894	0.5512	13.40	0.6893	0.5514	13.40	0.6888	0.5516	13.39
U-Net	0.6914	0.5469	11.45	0.6920	0.5478	11.45	0.6927	0.5484	11.45	0.6936	0.5490	11.45	0.6951	0.5498	11.45
Related Degradations and Domains															
INFWIDE	0.6371	**0.7040**	**18.87**	0.6378	**0.7045**	**18.87**	0.6394	**0.7050**	**18.86**	0.6411	**0.7050**	**18.81**	0.6426	**0.7041**	**18.79**
MetaWeather	0.6681	0.6672	17.93	0.6688	0.6668	17.94	0.6700	0.6662	17.94	0.6718	0.6650	17.94	0.6742	0.6634	17.93
Pixel2Pixel	0.6739	0.5668	13.24	0.6740	0.5665	13.24	0.6757	0.5655	13.25	0.6723	0.5751	13.33	0.6701	0.5803	13.63
DehazeFormer	**0.6297**	0.6858	18.34	**0.6325**	0.6766	17.70	0.6366	0.6692	17.05	0.6411	0.6636	16.77	0.6462	0.6592	16.60
DarkIR	0.9291	0.0364	4.40	0.9322	0.0358	4.37	0.9350	0.0351	4.34	0.9380	0.0343	4.31	0.9410	0.0335	4.28
OEPRL	**0.5778**	**0.7114**	**19.25**	**0.5840**	**0.7119**	**19.11**	**0.5904**	**0.7124**	**18.97**	**0.6027**	**0.7124**	**18.93**	**0.6154**	**0.7115**	**18.91**

Reducing the brightness of the wall pattern leaves Figure's principal organization recoverable. OEPRL remains first in all three metrics, while SSIM stays within 0.7114–0.7124 across the five levels. The narrow SSIM range indicates that the graphical arrangement remains recoverable as the wall pattern becomes fainter.

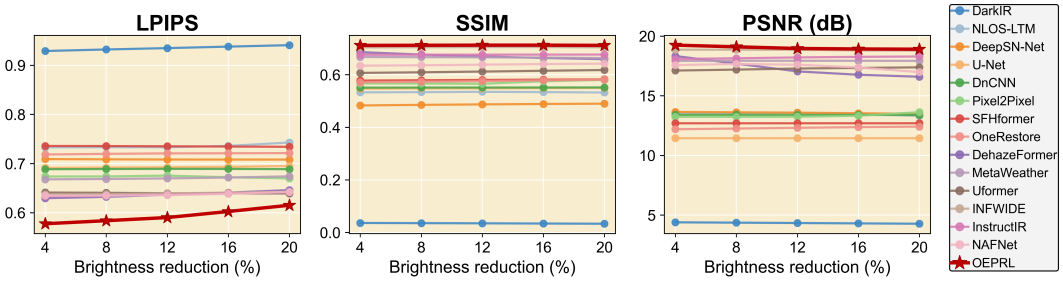

Figure A7: Figure trends under increasing brightness reduction. The curves report LPIPS, SSIM, and PSNR across the conditions in Table A6. Markers denote the evaluated settings.

The Figure curves show complementary responses in the three metrics. Structural agreement varies little across the sweep, while perceptual distance increases as the pattern becomes fainter. Thus, the stable SSIM accompanies preserved graphical arrangement even as perceptual differences grow. The following Lock results test this relationship on natural content.

Table A7: Lock point estimates under increasing brightness reduction. Best and second-best values are highlighted in red and blue, respectively. The corresponding trend is shown in Figure A8.

Method	4%			8%			12%			16%			20%		
	LPIPS↓	SSIM↑	PSNR (dB)↑	LPIPS↓	SSIM↑	PSNR (dB)↑	LPIPS↓	SSIM↑	PSNR (dB)↑	LPIPS↓	SSIM↑	PSNR (dB)↑	LPIPS↓	SSIM↑	PSNR (dB)↑
Passive Non-Line-of-Sight Reconstruction															
NLOS-LTM	0.7773	0.4140	10.87	0.7778	0.4138	10.86	0.7785	0.4124	10.82	0.7792	0.4101	10.78	0.7798	0.4070	10.73
All-in-One and Universal Image Restoration															
InstructIR	**0.6511**	**0.5819**	**16.37**	**0.6516**	**0.5824**	**16.38**	**0.6532**	**0.5831**	**16.34**	**0.6544**	**0.5833**	**16.25**	**0.6566**	**0.5822**	**16.13**
OneRestore	0.7241	0.5232	12.15	0.7242	0.5236	12.14	0.7243	0.5241	12.13	0.7245	0.5246	12.12	0.7247	0.5251	12.11
General-Purpose Image Restoration															
SFHformer	0.7431	0.5127	12.42	0.7427	0.5145	12.41	0.7421	0.5164	12.40	0.7417	0.5182	12.40	0.7414	0.5199	12.39
Uformer	0.6769	0.5647	15.08	0.6779	0.5654	15.11	0.6794	0.5655	15.11	0.6805	0.5652	15.08	0.6830	0.5643	15.02
NAFNet	0.6663	0.5647	15.15	0.6665	0.5658	15.12	0.6669	0.5669	15.06	0.6670	0.5679	14.97	0.6679	0.5686	14.88
DeepSN-Net	0.7727	0.4249	12.73	0.7722	0.4280	12.71	0.7716	0.4310	12.69	0.7709	0.4339	12.66	0.7704	0.4368	12.63
DnCNN	0.7241	0.4797	11.74	0.7242	0.4801	11.72	0.7244	0.4803	11.71	0.7246	0.4808	11.70	0.7250	0.4813	11.68
U-Net	0.7594	0.4912	12.13	0.7594	0.4916	12.11	0.7597	0.4921	12.09	0.7597	0.4929	12.08	0.7598	0.4931	12.06
Related Degradations and Domains															
INFWIDE	0.7357	0.5070	12.52	0.7358	0.5082	12.51	0.7360	0.5094	12.49	0.7373	0.5107	12.47	0.7401	0.5118	12.46
MetaWeather	0.7164	0.5113	15.52	0.7192	0.5098	15.49	0.7228	0.5071	15.42	0.7267	0.5039	15.30	0.7319	0.5012	15.18
Pixel2Pixel	0.7321	0.5178	12.30	0.7321	0.5184	12.29	0.7324	0.5190	12.28	0.7323	0.5197	12.27	0.7324	0.5203	12.26
DehazeFormer	0.6732	0.5327	14.69	0.6743	0.5324	14.65	0.6756	0.5316	14.56	0.6770	0.5305	14.45	0.6791	0.5292	14.31
DarkIR	0.8079	0.0910	8.71	0.8094	0.0906	8.70	0.8110	0.0901	8.68	0.8125	0.0896	8.67	0.8141	0.0891	8.66
OEPRL	**0.6300**	**0.6121**	**16.88**	**0.6308**	**0.6127**	**16.83**	**0.6330**	**0.6125**	**16.72**	**0.6352**	**0.6122**	**16.55**	**0.6384**	**0.6114**	**16.36**

Natural lock-screen content remains recoverable throughout the brightness sweep: OEPRL leads every metric, with SSIM within 0.6114–0.6127.

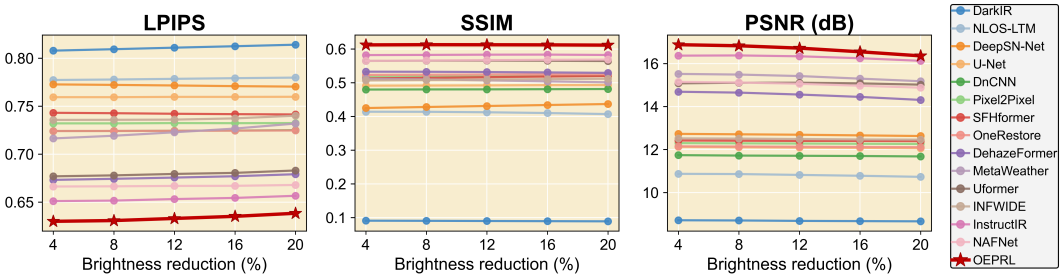

Figure A8: Lock trends under increasing brightness reduction. The curves report LPIPS, SSIM, and PSNR across the conditions in Table A7. Markers denote the evaluated settings.

Figure A9 shows that the broad sky–ground colors and the central foreground remain recognizable throughout the brightness sweep. The stable structural scores therefore correspond to a visible result: a fainter wall pattern still supports the organization of the hidden screen.

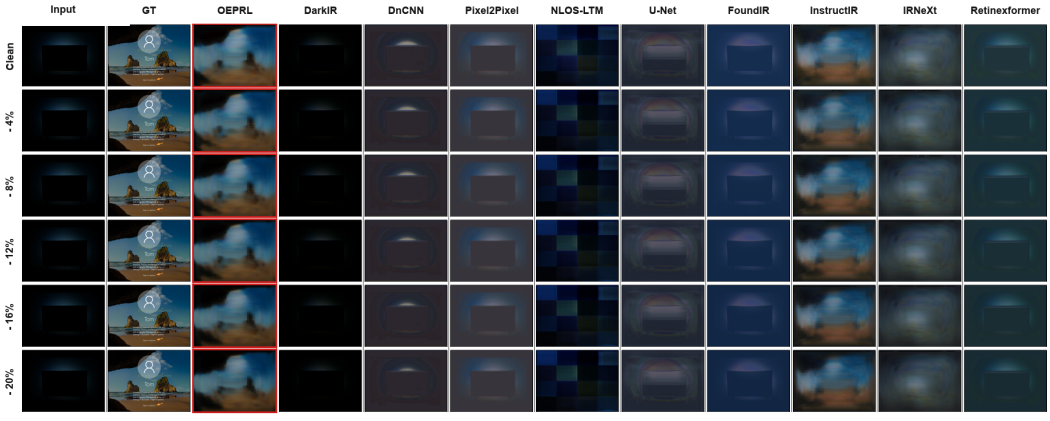

Figure A9: A Lock example under increasing brightness reduction. Rows show the reference observation and reductions of 4%, 8%, 12%, 16%, and 20%.

C.8 Gaussian Sensor Noise

Sensor noise introduces local fluctuations into the wall response. The question is whether the surviving color and spatial cues still support coherent screen regions.

Table A8: Figure point estimates under additive Gaussian noise. Best and second-best values are highlighted in red and blue, respectively. The corresponding trend is shown in Figure A10.

Method	20 dB			25 dB			30 dB			35 dB			40 dB		
	LPIPS↓	SSIM↑	PSNR (dB)↑	LPIPS↓	SSIM↑	PSNR (dB)↑	LPIPS↓	SSIM↑	PSNR (dB)↑	LPIPS↓	SSIM↑	PSNR (dB)↑	LPIPS↓	SSIM↑	PSNR (dB)↑
Passive Non-Line-of-Sight Reconstruction															
NLOS-LTM	0.7754	0.5092	11.60	0.7601	0.5146	12.16	0.7431	0.5250	13.06	0.7403	0.5270	13.21	0.7394	0.5278	13.26
All-in-One and Universal Image Restoration															
InstructIR	0.6838	0.6143	18.00	0.6509	0.6520	18.01	0.6390	0.6673	18.00	0.6354	0.6727	18.00	0.6341	0.6745	18.00
OneRestore	0.7357	0.5121	11.89	0.7227	0.5473	12.03	0.7183	0.5613	12.09	0.7176	0.5661	12.12	0.7177	0.5678	12.13
General-Purpose Image Restoration															
SFHformer	0.7824	0.5454	12.69	0.7523	0.5657	12.70	0.7399	0.5730	12.70	0.7367	0.5754	12.70	0.7362	0.5762	12.70
Uformer	0.7137	0.5274	16.96	0.6677	0.5741	16.99	0.6494	0.5936	17.00	0.6445	0.6006	17.00	0.6432	0.6028	17.00
NAFNet	0.6949	0.5698	17.32	0.6561	0.6091	17.34	0.6415	0.6266	17.35	0.6379	0.6331	17.35	0.6370	0.6353	17.36
DeepSN-Net	0.7927	0.4035	13.64	0.7441	0.4509	13.68	0.7225	0.4707	13.69	0.7145	0.4778	13.70	0.7118	0.4801	13.70
DnCNN	0.7486	0.4949	13.13	0.7128	0.5259	13.09	0.6986	0.5196	13.27	0.6895	0.5432	13.37	0.6885	0.5496	13.39
U-Net	0.6986	0.5384	12.17	0.6929	0.5448	11.74	0.6912	0.5467	11.54	0.6909	0.5468	11.47	0.6909	0.5465	11.44
Related Degradations and Domains															
INFWIDE	0.7773	0.6080	13.24	0.7169	0.6474	15.10	0.6883	0.6685	16.47	0.6531	**0.6956**	18.45	0.6368	**0.7040**	**18.86**
MetaWeather	0.6693	0.6646	17.92	0.6682	0.6667	17.92	0.6677	0.6674	17.92	0.6675	0.6676	17.92	0.6675	0.6677	17.93
Pixel2Pixel	0.7322	0.5059	13.79	0.7268	0.5304	14.31	0.7176	0.5532	14.69	0.7130	0.5647	14.86	0.7134	0.5612	14.82
DehazeFormer	**0.6343**	**0.6843**	**18.52**	**0.6297**	**0.6922**	**18.67**	**0.6290**	**0.6946**	**18.70**	**0.6284**	0.6953	**18.71**	**0.6281**	0.6954	18.71
DarkIR	0.9577	0.0369	4.45	0.9387	0.0378	4.45	0.9314	0.0380	4.44	0.9289	0.0381	4.44	0.9280	0.0381	4.44
OEPRL	**0.6145**	**0.6922**	**18.96**	**0.5890**	**0.6999**	**19.16**	**0.5786**	**0.7022**	**19.28**	**0.5763**	**0.7036**	**19.26**	**0.5752**	**0.7114**	**19.27**

The noise experiment tests a different change: the wall signal is increasingly mixed with random corruption. OEPRL leads all three metrics at 20 dB SNR, the strongest noise level in this sweep. As SNR rises to 40 dB, LPIPS improves from 0.6145 to 0.5752 and SSIM from 0.6922 to 0.7114. The method therefore benefits from cleaner optical evidence while already preserving a comparative advantage when that evidence is strongly corrupted.

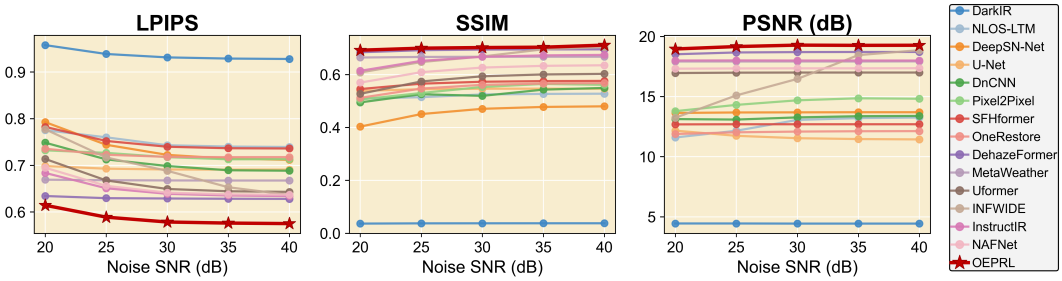

Figure A10: Figure trends under additive Gaussian noise. The curves report LPIPS, SSIM, and PSNR across the conditions in Table A8. Markers denote the evaluated settings.

The light graphical profiles and colored regions on the right remain visible as noise increases. Their organization within the dark screen background shows which graphical information survives the corrupted wall observation.

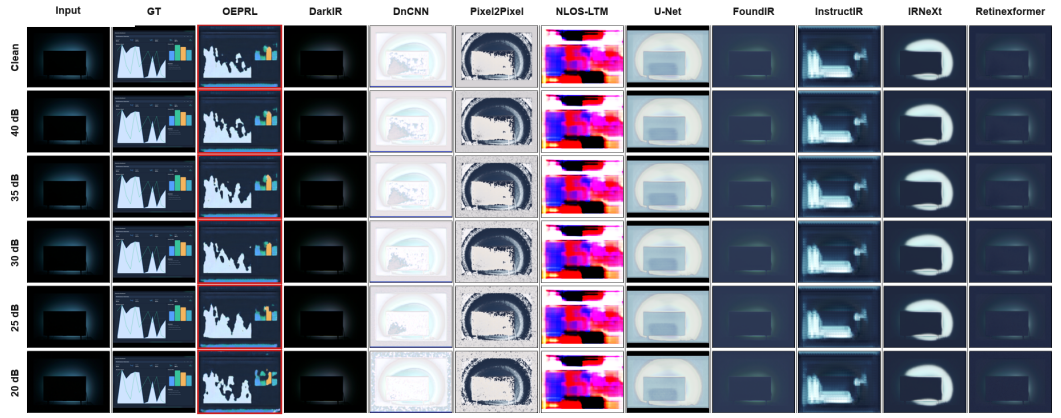

Figure A11: A Figure example under additive Gaussian noise. Rows show the reference observation followed by 40, 35, 30, 25, and 20 dB SNR.

C.9 CAMERA–WALL DISTANCE RATIO

Camera–wall distance changes the apparent size and spatial sampling of the wall response. Figure and Lock provide complementary content cases for testing whether the screen content remains recoverable as the observation geometry changes.

Figure A12 records the physical distance sweep with floor markers and a fixed relay wall.

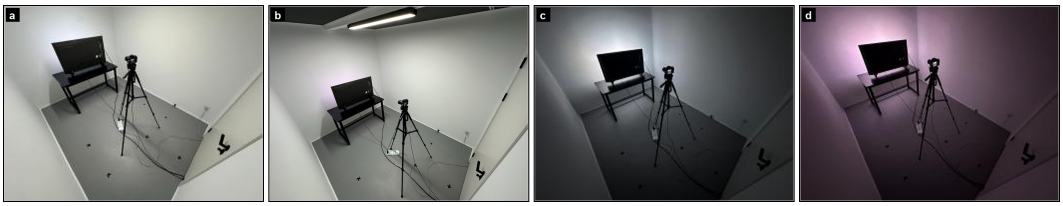

Figure A12: Representative camera placements relative to the fixed display and relay wall.

Moving the camera changes both the apparent extent and sampling density of the diffuse response while preserving the hidden-screen acquisition boundary. The associated curves and tables therefore measure how effectively the evidence pathway carries screen organization across this geometric change.

Table A9: Figure point estimates under varying camera–wall distance ratio. Best and second-best values are highlighted in red and blue, respectively. The corresponding trend is shown in Figure A13.

Method	1.5×			2.0×			2.5×			3.0×			3.5×		
	LPIPS↓	SSIM↑	PSNR (dB)↑	LPIPS↓	SSIM↑	PSNR (dB)↑	LPIPS↓	SSIM↑	PSNR (dB)↑	LPIPS↓	SSIM↑	PSNR (dB)↑	LPIPS↓	SSIM↑	PSNR (dB)↑
Passive Non-Line-of-Sight Reconstruction															
NLOS-LTM	0.7365	0.5297	13.38	0.7369	0.5290	13.35	0.7381	0.5280	13.30	0.7397	0.5268	13.22	0.7417	0.5255	13.15
All-in-One and Universal Image Restoration															
InstructIR	0.6387	0.6799	18.01	0.6386	0.6806	18.01	0.6378	0.6789	18.01	0.6405	0.6765	18.01	0.6407	0.6733	18.02
OneRestore	0.7196	0.5689	12.15	0.7214	0.5695	12.15	0.7222	0.5691	12.15	0.7231	0.5685	12.14	0.7241	0.5665	12.14
General-Purpose Image Restoration															
SFHformer	0.7387	0.5774	12.70	0.7391	0.5771	12.70	0.7417	0.5773	12.70	0.7426	0.5769	12.70	0.7450	0.5760	12.69
Uformer	0.6490	0.6066	17.04	0.6517	0.6077	17.06	0.6561	0.6071	17.07	0.6615	0.6055	17.08	0.6659	0.6027	17.09
NAFNet	0.6411	0.6373	17.41	0.6442	0.6387	17.42	0.6491	0.6377	17.43	0.6528	0.6360	17.44	0.6544	0.6334	17.43
DeepSN-Net	0.7143	0.4826	13.69	0.7127	0.4822	13.70	0.7144	0.4816	13.69	0.7218	0.4807	13.70	0.7253	0.4789	13.70
DnCNN	0.6869	0.5509	13.39	0.6859	0.5483	13.39	0.6868	0.5442	13.39	0.6867	0.5366	13.38	0.6918	0.5271	13.36
U-Net	0.6915	0.5461	11.46	0.6921	0.5459	11.47	0.6932	0.5458	11.51	0.6945	0.5454	11.52	0.6958	0.5450	11.55
Related Degradations and Domains															
INFWIDE	0.6408	**0.6993**	**18.69**	0.6531	**0.6958**	18.51	0.6646	**0.6953**	**18.25**	0.6787	**0.6853**	17.39	0.7038	0.6754	16.48
MetaWeather	0.6678	0.6678	17.92	0.6677	0.6676	17.92	0.6677	0.6677	17.90	0.6669	0.6678	17.89	0.6677	0.6675	17.88
Pixel2Pixel	0.6710	0.5715	14.36	0.7235	0.5308	14.09	0.7406	0.5130	13.92	0.7462	0.5036	13.78	0.7495	0.4957	13.62
DehazeFormer	**0.6289**	0.6923	18.63	**0.6302**	0.6941	**18.69**	**0.6326**	0.6820	18.04	**0.6332**	0.6821	**18.16**	**0.6360**	**0.6805**	**18.03**
DarkIR	0.9361	0.0375	4.44	0.9425	0.0375	4.43	0.9455	0.0376	4.43	0.9518	0.0378	4.44	0.9543	0.0379	4.44
OEPRL	**0.5761**	**0.7069**	**19.25**	**0.5769**	**0.7039**	**19.20**	**0.5807**	**0.7029**	**19.16**	**0.5839**	**0.6972**	**19.04**	**0.5895**	**0.6926**	**19.03**

After signal-quality changes, the distance settings test recovery under changes in the apparent size and spatial sampling of the wall response. OEPRL remains first in all three metrics on Figure and Lock, with Figure PSNR between 19.03 and 19.25 dB (Tables A9–A10).

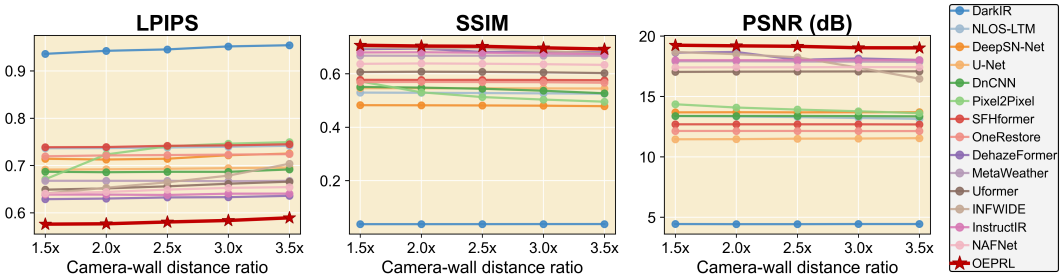

Figure A13: Figure trends under varying camera–wall distance ratio. The curves report LPIPS, SSIM, and PSNR across the conditions in Table A9. Markers denote the evaluated settings.

Across the Figure distance sweep, LPIPS changes from 0.5761 to 0.5895 and SSIM from 0.7069 to 0.6926, alongside the narrow PSNR range. OEPRL leads each metric throughout these changes in observation scale. The Lock experiment below examines the corresponding recovery of natural color transitions and foreground–background structure.

Table A10: Lock point estimates under varying camera–wall distance ratio. Best and second-best values are highlighted in red and blue, respectively. The corresponding trend is shown in Figure A14.

Method	1.5×			2.0×			2.5×			3.0×			3.5×		
	LPIPS↓	SSIM↑	PSNR (dB)↑	LPIPS↓	SSIM↑	PSNR (dB)↑	LPIPS↓	SSIM↑	PSNR (dB)↑	LPIPS↓	SSIM↑	PSNR (dB)↑	LPIPS↓	SSIM↑	PSNR (dB)↑
Passive Non-Line-of-Sight Reconstruction															
NLOS-LTM	0.7771	0.4025	10.82	0.7765	0.3812	10.59	0.7789	0.3375	10.11	0.7827	0.3058	9.78	0.7861	0.2823	9.55
All-in-One and Universal Image Restoration															
InstructIR	**0.6511**	**0.5885**	**16.46**	**0.6507**	**0.5861**	**16.44**	**0.6516**	**0.5837**	**16.40**	**0.6532**	**0.5801**	**16.36**	**0.6583**	**0.5642**	**16.08**
OneRestore	0.7276	0.5222	12.15	0.7296	0.5217	12.15	0.7298	0.5205	12.15	0.7279	0.5187	12.15	0.7261	0.5160	12.14
General-Purpose Image Restoration															
SFHformer	0.7434	0.5112	12.41	0.7423	0.5109	12.41	0.7450	0.5122	12.41	0.7435	0.5121	12.40	0.7433	0.5115	12.40
Uformer	0.6792	0.5658	15.09	0.6788	0.5652	15.10	0.6804	0.5641	15.09	0.6820	0.5617	15.05	0.6845	0.5577	15.02
NAFNet	0.6678	0.5637	15.18	0.6675	0.5634	15.18	0.6685	0.5621	15.18	0.6709	0.5602	15.18	0.6746	0.5565	15.17
DeepSN-Net	0.7791	0.4230	12.75	0.7796	0.4232	12.75	0.7832	0.4231	12.75	0.7865	0.4225	12.75	0.7898	0.4213	12.74
DnCNN	0.7274	0.4789	11.75	0.7290	0.4778	11.72	0.7271	0.4754	11.68	0.7293	0.4733	11.67	0.7293	0.4708	11.67
U-Net	0.7605	0.4884	12.05	0.7613	0.4870	11.96	0.7657	0.4858	11.94	0.7643	0.4859	11.89	0.7634	0.4836	11.85
Related Degradations and Domains															
INFWIDE	0.7391	0.5091	12.53	0.7410	0.5080	12.53	0.7401	0.5070	12.52	0.7403	0.5061	12.52	0.7393	0.5053	12.52
MetaWeather	0.7154	0.5173	15.60	0.7159	0.5151	15.58	0.7162	0.5135	15.56	0.7173	0.5114	15.53	0.7174	0.5090	15.50
Pixel2Pixel	0.7322	0.5175	12.31	0.7320	0.5174	12.31	0.7335	0.5170	12.30	0.7363	0.5166	12.30	0.7401	0.5156	12.29
DehazeFormer	0.6726	0.5349	14.75	0.6711	0.5345	14.72	0.6722	0.5328	14.72	0.6741	0.5296	14.72	0.6778	0.5246	14.72
DarkIR	0.8101	0.0920	8.72	0.8116	0.0921	8.72	0.8146	0.0923	8.72	0.8165	0.0926	8.72	0.8184	0.0930	8.73
OEPRL	**0.6277**	**0.6157**	**17.01**	**0.6288**	**0.6147**	**16.87**	**0.6300**	**0.6096**	**16.74**	**0.6339**	**0.6022**	**16.47**	**0.6401**	**0.5884**	**16.17**

Lock confirms that the distance result also holds for natural screen imagery. OEPRL leads every distance setting in perceptual, structural, and pixel-level agreement, extending the recovery advantage across both content type and observation scale.

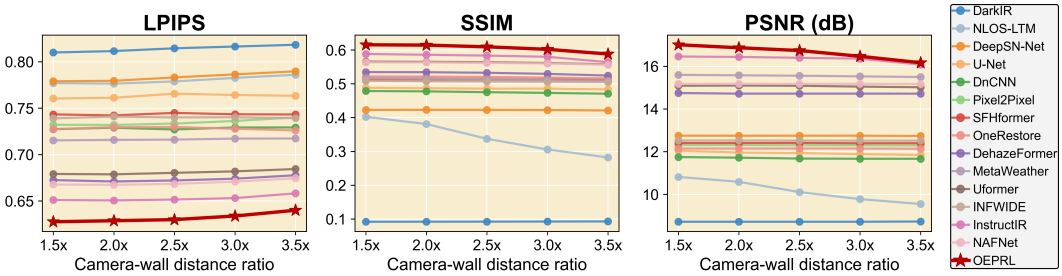

Figure A14: Lock trends under varying camera–wall distance ratio. The curves report LPIPS, SSIM, and PSNR across the conditions in Table A10. Markers denote the evaluated settings.

In Figure A15, the reconstructed chart regions retain distinct colors within the bright page, while several comparison outputs merge the page into a largely uniform region. The advantage is therefore visible in the screen's regional organization as the wall response changes in apparent scale.

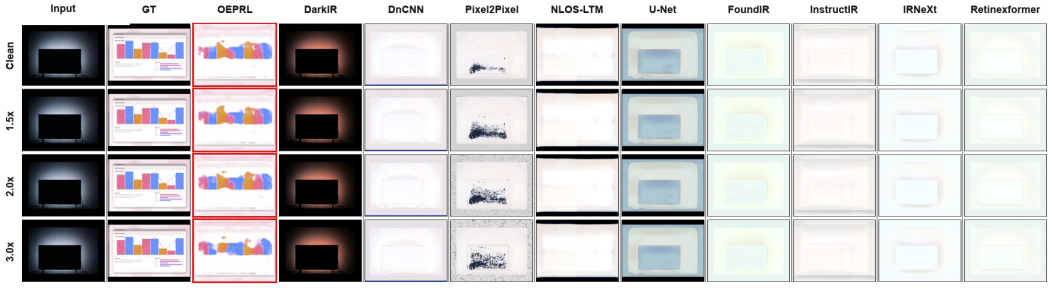

Figure A15: A Figure example at selected distance settings. Rows show the reference observation and the 1.5×, 2.0×, and 3.0× settings.

C.10 Camera Position

Vertical and horizontal camera offsets translate the measured wall pattern within the observation geometry. The two sweeps test whether useful screen organization remains recoverable when wall evidence appears at displaced image locations.

The representative views in Figure A16 document displaced camera placements relative to the display and relay wall.



Figure A16: Camera placements at three vertical positions relative to the fixed display and relay wall.

Such motion shifts where the wall response is sampled in the image. The reconstruction must therefore carry evidence observed at displaced wall positions into the screen regions being recovered.

Table A11: Figure point estimates under vertical position perturbation. Best and second-best values are highlighted in red and blue, respectively. The corresponding trend is shown in Figure A17.

Method	D15%			D10%			D5%			D2%			U2%			U5%			U10%			U15%		
	LPIPS↓	SSIM↑	PSNR (dB)↑	LPIPS↓	SSIM↑	PSNR (dB)↑	LPIPS↓	SSIM↑	PSNR (dB)↑	LPIPS↓	SSIM↑	PSNR (dB)↑	LPIPS↓	SSIM↑	PSNR (dB)↑	LPIPS↓	SSIM↑	PSNR (dB)↑	LPIPS↓	SSIM↑	PSNR (dB)↑	LPIPS↓	SSIM↑	PSNR (dB)↑
Passive Non-Line-of-Sight Reconstruction																								
NLOS-LTM	0.7709	0.5141	12.07	0.7501	0.5198	12.94	0.7376	0.5274	13.45	0.7369	0.5284	13.40	0.7412	0.5278	13.15	0.7432	0.5275	13.04	0.7456	0.5279	12.68	0.7637	0.5364	11.80
All-in-One and Universal Image Restoration																								
InstructIR	**0.6294**	0.6519	17.49	**0.6404**	0.6538	**17.55**	0.6398	0.6621	17.75	0.6376	0.6597	17.73	**0.6344**	0.6618	17.80	0.6396	0.6635	17.81	**0.6338**	0.6630	17.69	**0.6383**	0.6618	17.55
OneRestore	0.7250	0.5689	12.11	0.7261	0.5668	12.08	0.7235	0.5658	12.10	0.7187	0.5675	12.13	0.7155	0.5698	12.16	0.7153	0.5711	12.18	0.7208	0.5761	12.24	0.7248	0.5786	12.23
General-Purpose Image Restoration																								
SFHformer	0.7436	0.5691	12.61	0.7448	0.5724	12.71	0.7376	0.5703	12.68	0.7347	0.5752	12.70	0.7425	0.5739	12.69	0.7398	0.5731	12.64	0.7421	0.5766	12.58	0.7512	0.5796	12.54
Uformer	0.6577	0.6005	16.52	0.6656	0.5710	12.87	0.6491	0.6050	16.95	0.6459	0.6026	16.92	0.6409	0.6072	16.99	0.6428	0.6115	17.05	0.6506	0.6229	17.15	0.6584	0.6252	17.08
NAFNet	0.6372	0.6365	17.58	0.6425	0.6383	17.42	**0.6372**	0.6359	17.38	0.6381	0.6380	17.40	0.6350	0.6410	17.43	**0.6359**	0.6418	17.45	0.6422	0.6477	17.46	0.6513	0.6489	**17.62**
DeepSN-Net	0.7064	0.4746	13.25	0.7155	0.4735	13.38	0.7134	0.4756	13.51	0.7150	0.4780	13.64	0.7065	0.4806	13.66	0.7058	0.4799	13.54	0.7117	0.4859	13.44	0.7163	0.4897	13.45
DnCNN	0.7067	0.5536	13.28	0.7002	0.5499	13.29	0.6900	0.5518	13.34	0.6866	0.5497	13.37	0.6839	0.5513	13.38	0.6877	0.5574	13.39	0.6920	0.5634	13.39	0.6964	0.5659	13.38
U-Net	0.7146	0.5475	11.00	0.7059	0.5462	11.17	0.7000	0.5464	11.36	0.6911	0.5435	11.43	0.6937	0.5467	11.39	0.6987	0.5508	11.33	0.7116	0.5563	11.16	0.7235	0.5583	11.02
Related Degradations and Domains																								
INFWIDE	0.7323	0.6267	14.68	0.7215	**0.6670**	15.88	0.7205	0.6672	15.27	**0.6333**	**0.6973**	**18.79**	0.6483	**0.6961**	**18.57**	0.7256	0.6043	13.78	0.7025	0.6505	15.55	0.6853	**0.6884**	17.53
MetaWeather	0.8210	0.4571	14.35	0.8296	0.4525	14.13	0.7537	0.5510	17.33	0.6908	0.6177	17.86	0.6883	0.6296	17.79	0.7815	0.5223	15.82	0.8292	0.4843	14.08	0.8432	0.4732	12.90
Pixel2Pixel	0.6764	0.5901	14.21	0.6714	0.5930	14.48	0.6573	0.5966	14.75	0.6583	0.5920	14.84	0.6606	0.5928	14.83	0.6630	0.5988	14.74	0.6745	0.5990	14.50	0.6813	0.6010	14.27
DehazeFormer	0.6667	**0.6655**	**17.67**	0.6613	0.6598	17.47	0.6589	**0.6699**	**17.79**	0.6501	0.6883	18.11	0.6535	0.6867	18.15	0.6609	**0.6909**	**17.87**	0.6579	**0.6775**	**17.95**	0.6693	0.6696	17.52
DarkIR	0.9188	0.0318	4.31	0.9184	0.0352	4.38	0.9213	0.0379	4.43	0.9231	0.0384	4.44	0.9271	0.0382	4.44	0.9363	0.0367	4.42	0.9417	0.0344	4.37	0.9450	0.0328	4.34
OEPRL	**0.6257**	**0.6690**	**17.79**	**0.6366**	**0.6705**	**17.67**	**0.6357**	**0.6734**	**17.91**	**0.6295**	**0.7008**	**18.91**	**0.6306**	**0.6996**	**18.69**	**0.6292**	**0.6944**	**18.03**	**0.6300**	**0.6810**	**18.07**	**0.6345**	**0.6919**	**17.74**

Vertical displacement changes where the wall evidence appears in the observation. OEPRL remains first in every metric for both upward and downward offsets. The qualitative example shows the corresponding recovery of graphical regions within the hidden screen, connecting a displaced observation to the content being reconstructed.

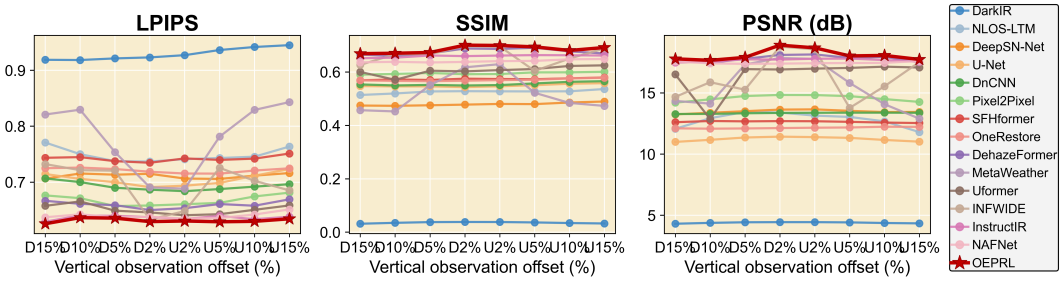

Figure A17: Figure trends under vertical camera-position perturbations. The curves report LPIPS, SSIM, and PSNR across the conditions in Table A11. Markers denote the evaluated settings.

The upward and downward settings provide separate views of the effect of displacement. OEPRL remains first on the Figure metrics in both directions, linking the comparison to displaced wall evidence rather than to a single favorable offset. The Lock table extends the same test to natural screen content.

Table A12: Lock point estimates under vertical position perturbation. Best and second-best values are highlighted in red and blue, respectively. The corresponding trend is shown in Figure A18.

Method	D15%			D10%			D5%			D2%			U2%			U5%			U10%			U15%		
	LPIPS↓	SSIM↑	PSNR (dB)↑	LPIPS↓	SSIM↑	PSNR (dB)↑	LPIPS↓	SSIM↑	PSNR (dB)↑	LPIPS↓	SSIM↑	PSNR (dB)↑	LPIPS↓	SSIM↑	PSNR (dB)↑	LPIPS↓	SSIM↑	PSNR (dB)↑	LPIPS↓	SSIM↑	PSNR (dB)↑	LPIPS↓	SSIM↑	PSNR (dB)↑
Passive Non-Line-of-Sight Reconstruction																								
NLOS-LTM	0.7870	0.3955	10.35	0.7827	0.3970	10.60	0.7801	0.4073	10.87	0.7775	0.4024	10.86	0.7783	0.4104	10.96	0.7796	0.4112	10.91	0.7858	0.4197	10.92	0.7878	0.4228	10.84
All-in-One and Universal Image Restoration																								
InstructIR	0.7040	0.4474	13.60	0.6898	0.5332	14.77	**0.6663**	**0.5668**	**15.78**	**0.6743**	0.5375	**15.17**	**0.6728**	0.5271	**15.06**	0.6893	0.4483	13.71	0.6844	0.4990	14.22	0.6818	0.5476	15.01
OneRestore	0.7301	0.5213	12.05	0.7271	0.5214	12.09	0.7258	0.5224	12.13	0.7240	0.5223	12.14	0.7225	0.5221	12.15	0.7221	0.5223	12.15	0.7226	0.5228	12.15	0.7245	0.5234	12.13
General-Purpose Image Restoration																								
SFHformer	0.7596	0.4987	12.12	0.7544	0.5010	12.19	0.7529	0.5006	12.26	0.7459	0.5071	12.37	0.7445	0.5073	12.37	0.7447	0.5020	12.30	0.7485	0.5020	12.19	0.7552	0.5009	12.09
Uformer	0.7315	0.4799	11.63	0.7300	0.4748	11.86	0.7067	0.5137	13.37	0.7177	0.5001	12.41	0.7091	0.4843	12.32	0.6934	0.5067	13.51	0.7147	0.4697	12.38	0.7143	0.4617	11.96
NAFNet	**0.6752**	**0.5576**	**14.97**	0.6729	**0.5553**	**15.02**	0.6729	0.5589	15.16	0.6756	**0.5541**	15.03	0.6745	**0.5541**	15.04	**0.6712**	**0.5577**	**15.10**	**0.6686**	**0.5567**	**15.04**	**0.6670**	**0.5599**	**15.06**
DeepSN-Net	0.7940	0.4082	12.15	0.7877	0.4009	12.21	0.7802	0.4083	12.41	0.7758	0.4166	12.60	0.7804	0.4188	12.76	0.7802	0.4109	12.58	0.7794	0.4012	12.09	0.7861	0.4058	12.15
DnCNN	0.7262	0.4788	11.63	0.7256	0.4788	11.69	0.7262	0.4791	11.73	0.7250	0.4791	11.75	0.7235	0.4786	11.75	0.7225	0.4790	11.75	0.7209	0.4801	11.74	0.7202	0.4818	11.73
U-Net	0.7574	0.4884	11.94	0.7619	0.4878	11.99	0.7636	0.4875	12.03	0.7640	0.4878	12.07	0.7631	0.4886	12.10	0.7618	0.4877	12.08	0.7571	0.4909	12.09	0.7566	0.4924	12.06
Related Degradations and Domains																								
INFWIDE	0.8533	0.0696	8.44	0.8533	0.0696	8.44	0.8533	0.0696	8.44	0.8533	0.0696	8.44	0.8533	0.0696	8.44	0.8533	0.0696	8.44	0.8533	0.0696	8.44	0.8533	0.0696	8.44
MetaWeather	0.8266	0.2861	10.86	0.8044	0.3817	11.79	0.7741	0.4097	12.46	0.7336	0.4787	14.38	0.7209	0.4769	14.81	0.7365	0.4460	13.98	0.7629	0.3732	12.32	0.7847	0.3290	12.15
Pixel2Pixel	0.7349	0.5149	12.14	0.7332	0.5160	12.22	0.7334	0.5176	12.28	0.7327	0.5177	12.31	0.7317	0.5174	12.32	0.7314	0.5174	12.31	0.7312	0.5173	12.28	0.7315	0.5173	12.25
DehazeFormer	0.6779	0.5233	14.58	**0.6713**	0.5241	14.70	0.6742	0.5186	14.66	0.6748	0.5211	14.75	0.6737	0.5188	14.72	0.6745	0.5143	14.62	0.6714	0.5213	14.68	0.6706	0.5241	14.64
DarkIR	0.8158	0.0866	8.64	0.8109	0.0895	8.69	0.8081	0.0916	8.71	0.8067	0.0923	8.73	0.8058	0.0930	8.73	0.8055	0.0931	8.73	0.8062	0.0924	8.73	0.8073	0.0915	8.72
OEPRL	**0.6711**	**0.5611**	**15.09**	**0.6672**	**0.5568**	**15.14**	**0.6594**	**0.5849**	**15.90**	**0.6685**	**0.5685**	**15.45**	**0.6649**	**0.5608**	**15.27**	**0.6699**	**0.5612**	**15.22**	**0.6672**	**0.5602**	**15.16**	**0.6629**	**0.5634**	**15.18**

The same advantage extends to Lock across both displacement directions. OEPRL reaches 15.09 dB PSNR at D15% and 15.18 dB at U15%, leading the three metrics at both endpoints.

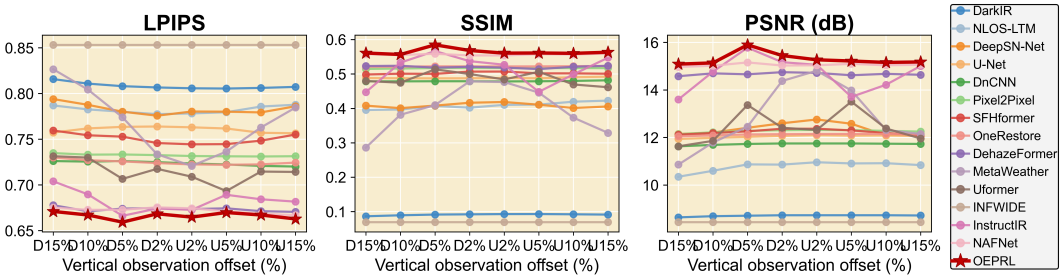

Figure A18: Lock trends under vertical camera-position perturbations. The curves report LPIPS, SSIM, and PSNR across the conditions in Table A12. Markers denote the evaluated settings.

In the Figure example (Figure A19), displaced wall observations continue to yield chart-related color structure within the dark interface.

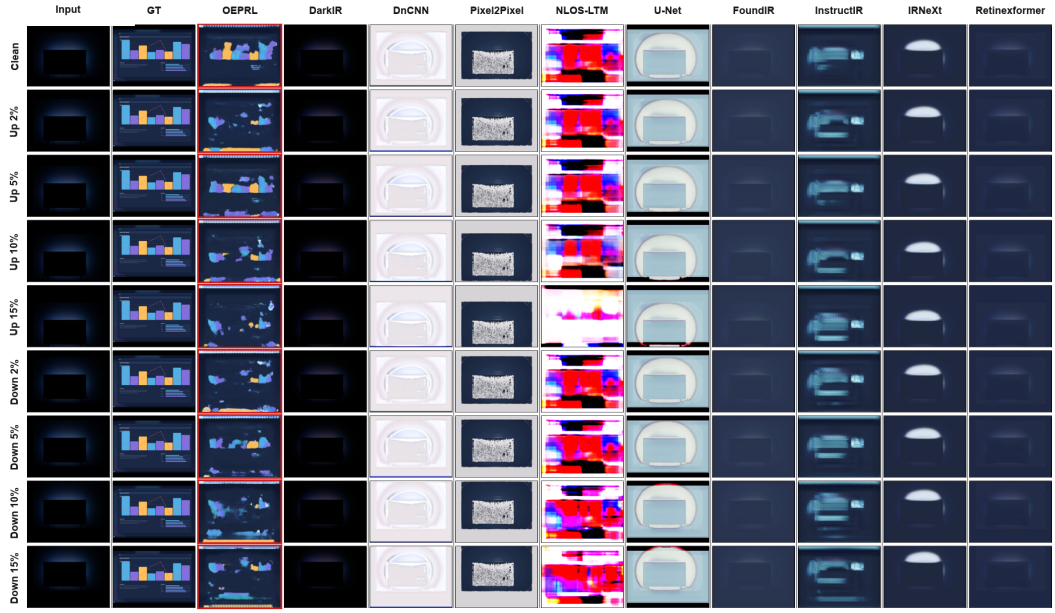

Figure A19: A Figure example under vertical observation offsets. Rows show the reference, upward offsets of 2%, 5%, 10%, and 15%, and downward offsets of 2%, 5%, 10%, and 15%.

Horizontal offsets test the same observation-to-content relationship along a second axis.

Table A13: Figure point estimates under horizontal position perturbation. Best and second-best values are highlighted in red and blue, respectively. The corresponding trend is shown in Figure A20.

Method	L15%			L10%			L5%			L2%			R2%			R5%			R10%			R15%		
	LPIPS↓	SSIM↑	PSNR (dB)↑	LPIPS↓	SSIM↑	PSNR (dB)↑	LPIPS↓	SSIM↑	PSNR (dB)↑	LPIPS↓	SSIM↑	PSNR (dB)↑	LPIPS↓	SSIM↑	PSNR (dB)↑	LPIPS↓	SSIM↑	PSNR (dB)↑	LPIPS↓	SSIM↑	PSNR (dB)↑	LPIPS↓	SSIM↑	PSNR (dB)↑
Passive Non-Line-of-Sight Reconstruction																								
NLOS-LTM	0.7478	0.5516	12.97	0.7330	0.5514	13.73	0.7319	0.5398	13.68	0.7352	0.5335	13.52	0.7434	0.5240	13.07	0.7493	0.5185	12.77	0.7566	0.5126	12.31	0.7700	0.5119	11.71
All-in-One and Universal Image Restoration																								
InstructIR	0.6368	0.6656	17.81	0.6371	0.6700	17.84	0.6374	0.6709	17.91	0.6340	0.6720	17.97	0.6337	0.6720	17.98	0.6314	0.6685	17.91	0.6331	0.6661	17.78	0.6384	0.6635	17.89
OneRestore	0.7223	0.5685	12.10	0.7245	0.5683	12.12	0.7245	0.5685	12.14	0.7223	0.5684	12.13	0.7183	0.5694	12.16	0.7154	0.5686	12.15	0.7137	0.5695	12.14	0.7178	0.5680	12.12
General-Purpose Image Restoration																								
SFHformer	0.7330	0.5716	12.66	0.7342	0.5734	12.63	0.7308	0.5757	12.65	0.7325	0.5739	12.68	0.7347	0.5738	12.72	0.7325	0.5724	12.69	0.7321	0.5737	12.70	0.7324	0.5730	12.72
Uformer	0.6859	0.5456	11.22	0.6535	0.6033	16.94	0.6528	0.6024	16.97	0.6459	0.6035	16.99	0.6434	0.6037	17.00	0.6443	0.6047	17.03	0.6472	0.6089	17.01	0.6933	0.5472	11.09
NAFNet	0.6393	0.6308	17.56	0.6405	0.6348	17.40	0.6398	0.6353	17.34	0.6377	0.6365	17.36	0.6348	0.6352	17.35	0.6335	0.6351	17.36	0.6327	0.6366	17.44	0.6394	0.6338	17.66
DeepSN-Net	0.7198	0.4742	13.52	0.7168	0.4750	13.58	0.7171	0.4768	13.61	0.7129	0.4773	13.65	0.7098	0.4776	13.64	0.7104	0.4759	13.61	0.7157	0.4772	13.57	0.7202	0.4759	13.55
DnCNN	0.7006	0.5576	13.34	0.7009	0.5558	13.32	0.6977	0.5535	13.35	0.6909	0.5521	13.38	0.6895	0.5528	13.39	0.6925	0.5532	13.37	0.6994	0.5569	13.32	0.7055	0.5579	13.33
U-Net	0.7125	0.5479	11.20	0.7121	0.5477	11.31	0.7025	0.5441	11.36	0.6950	0.5450	11.40	0.6963	0.5457	11.40	0.6998	0.5454	11.43	0.7064	0.5493	11.38	0.7183	0.5486	11.24
Related Degradations and Domains																								
INFWIDE	0.6722	0.6868	17.76	0.6618	0.6923	18.11	0.6479	0.7000	18.55	0.6424	0.7023	18.70	0.6424	0.7023	18.67	0.6607	0.6967	18.51	0.6858	0.6793	17.37	0.6883	0.6833	17.55
MetaWeather	0.8680	0.4550	12.88	0.8418	0.4748	14.02	0.7761	0.5187	16.06	0.6798	0.6389	17.96	0.6756	0.6409	18.02	0.7453	0.5603	17.09	0.7888	0.5222	15.81	0.8257	0.5019	14.30
Pixel2Pixel	0.6803	0.5993	14.50	0.6742	0.6011	14.69	0.6678	0.5971	14.83	0.6618	0.5949	14.85	0.6572	0.5947	14.88	0.6628	0.5966	14.87	0.6704	0.5999	14.69	0.6817	0.5964	14.47
DehazeFormer	0.6612	0.6766	17.73	0.6615	0.6839	17.85	0.6513	0.6853	18.18	0.6467	0.6878	18.28	0.6547	0.6869	18.21	0.6490	0.6851	18.22	0.6556	0.6853	18.07	0.6691	0.6831	17.87
DarkIR	0.9367	0.0368	4.41	0.9384	0.0384	4.43	0.9340	0.0386	4.44	0.9345	0.0383	4.44	0.9276	0.0381	4.44	0.9332	0.0380	4.44	0.9366	0.0372	4.43	0.9399	0.0350	4.40
OEPRL	0.6223	0.6903	17.94	0.6155	0.6958	18.12	0.6123	0.7035	18.67	0.6023	0.7058	18.82	0.5961	0.7058	18.73	0.6028	0.7002	18.53	0.6099	0.6888	18.15	0.6232	0.6868	18.01

OEPRL leads every Figure metric, and the image sequence retains recognizable graphical color organization across lateral shifts.

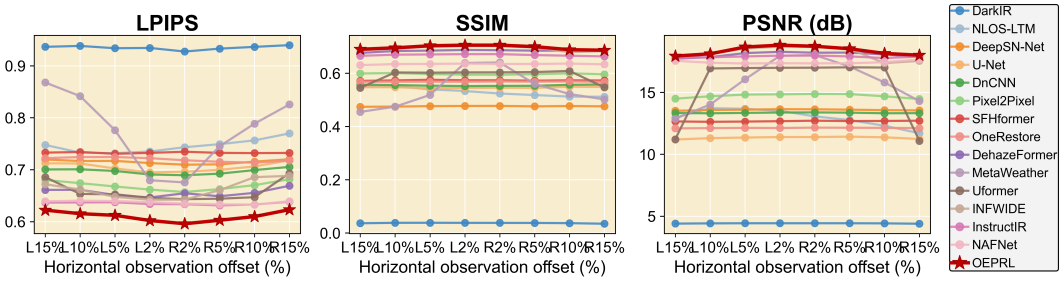

Figure A20: Figure trends under horizontal camera-position perturbations. The curves report LPIPS, SSIM, and PSNR across the conditions in Table A13. Markers denote the evaluated settings.

The lateral Figure curves preserve OEPRL's lead across both displacement directions. The agreement of the perceptual, structural, and pixel-level comparisons shows that the advantage is visible under several measures of reconstruction quality. The following Lock comparison examines how this result extends to natural image organization.

Table A14: Lock point estimates under horizontal position perturbation. Best and second-best values are highlighted in red and blue, respectively. The corresponding trend is shown in Figure A21.

Method	L15%			L10%			L5%			L2%			R2%			R5%			R10%			R15%		
	LPIPS↓	SSIM↑	PSNR (dB)↑	LPIPS↓	SSIM↑	PSNR (dB)↑	LPIPS↓	SSIM↑	PSNR (dB)↑	LPIPS↓	SSIM↑	PSNR (dB)↑	LPIPS↓	SSIM↑	PSNR (dB)↑	LPIPS↓	SSIM↑	PSNR (dB)↑	LPIPS↓	SSIM↑	PSNR (dB)↑	LPIPS↓	SSIM↑	PSNR (dB)↑
Passive Non-Line-of-Sight Reconstruction																								
NLOS-LTM	0.7816	0.3913	10.42	0.7784	0.3968	10.57	0.7770	0.3998	10.72	0.7770	0.4030	10.83	0.7771	0.4067	10.91	0.7785	0.4022	10.79	0.7817	0.3992	10.61	0.7852	0.3978	10.43
All-in-One and Universal Image Restoration																								
InstructIR	0.6934	0.5294	14.76	0.6839	0.5450	**15.24**	**0.6619**	**0.5760**	**16.10**	**0.6526**	**0.5854**	**16.38**	**0.6531**	**0.5870**	**16.40**	**0.6572**	**0.5838**	**16.29**	0.6737	0.5598	**15.57**	0.6837	0.5449	**15.19**
OneRestore	0.7282	0.5210	12.09	0.7275	0.5221	12.12	0.7273	0.5221	12.14	0.7266	0.5224	12.15	0.7264	0.5225	12.15	0.7263	0.5223	12.15	0.7281	0.5224	12.14	0.7274	0.5214	12.11
General-Purpose Image Restoration																								
SFHformer	0.7571	0.4977	12.09	0.7540	0.5022	12.20	0.7500	0.5060	12.34	0.7467	0.5087	12.41	0.7449	0.5071	12.30	0.7465	0.5027	12.13	0.7493	0.4982	11.96	0.7563	0.4971	11.95
Uformer	0.7060	0.5263	13.41	0.6985	0.5357	14.06	0.6896	0.5482	14.56	0.6888	0.5500	14.59	0.6856	0.5500	14.65	0.6890	0.5483	14.60	0.6935	0.5440	14.41	0.6956	0.5341	13.92
NAFNet	**0.6737**	**0.5619**	**15.03**	**0.6698**	**0.5625**	15.17	0.6662	0.5624	15.18	0.6663	0.5624	15.19	0.6675	0.5623	15.19	0.6675	0.5623	15.19	**0.6678**	**0.5625**	15.18	**0.6692**	**0.5624**	15.14
DeepSN-Net	0.7981	0.4057	12.20	0.7912	0.4084	12.35	0.7850	0.4153	12.60	0.7786	0.4211	12.73	0.7793	0.4191	12.70	0.7808	0.4087	12.45	0.7880	0.4034	12.24	0.7960	0.4050	12.26
DnCNN	0.7240	0.4786	11.70	0.7239	0.4791	11.73	0.7245	0.4785	11.74	0.7249	0.4787	11.75	0.7262	0.4788	11.75	0.7250	0.4790	11.75	0.7235	0.4797	11.75	0.7224	0.4797	11.73
U-Net	0.7590	0.4878	12.00	0.7617	0.4882	12.05	0.7638	0.4879	12.09	0.7644	0.4881	12.11	0.7655	0.4880	12.12	0.7654	0.4880	12.12	0.7627	0.4884	12.09	0.7586	0.4878	12.05
Related Degradations and Domains																								
INFWIDE	0.8533	0.0696	8.44	0.8533	0.0696	8.44	0.8533	0.0696	8.44	0.8533	0.0696	8.44	0.8533	0.0696	8.44	0.8533	0.0696	8.44	0.8533	0.0696	8.44	0.8533	0.0696	8.44
MetaWeather	0.7968	0.3892	12.29	0.7796	0.4211	12.90	0.7617	0.4358	13.40	0.7485	0.4611	13.99	0.7427	0.4725	14.39	0.7481	0.4624	14.23	0.7709	0.3974	12.83	0.7920	0.3728	12.33
Pixel2Pixel	0.7338	0.5152	12.21	0.7341	0.5170	12.27	0.7335	0.5174	12.30	0.7341	0.5176	12.31	0.7347	0.5177	12.32	0.7338	0.5176	12.31	0.7330	0.5173	12.29	0.7324	0.5157	12.25
DehazeFormer	0.6762	0.5339	14.62	0.6733	0.5356	14.72	0.6745	0.5348	14.77	0.6709	0.5365	14.78	0.6739	0.5354	14.81	0.6726	0.5363	14.79	0.6747	0.5365	14.76	0.6792	0.5329	14.71
DarkIR	0.8142	0.0913	8.70	0.8111	0.0924	8.72	0.8088	0.0928	8.73	0.8080	0.0927	8.73	0.8080	0.0926	8.73	0.8085	0.0925	8.73	0.8104	0.0920	8.72	0.8118	0.0911	8.72
OEPRL	**0.6696**	**0.5654**	**15.15**	**0.6658**	**0.5686**	**15.55**	**0.6447**	**0.5959**	**16.49**	**0.6360**	**0.6028**	**16.79**	**0.6358**	**0.6039**	**16.84**	**0.6412**	**0.5997**	**16.61**	**0.6620**	**0.5820**	**15.89**	**0.6652**	**0.5721**	**15.51**

OEPRL also leads every horizontal-offset condition on Lock. Together with the vertical sweep, this establishes a reconstruction advantage across displacement in both image directions and across graphical and natural content.

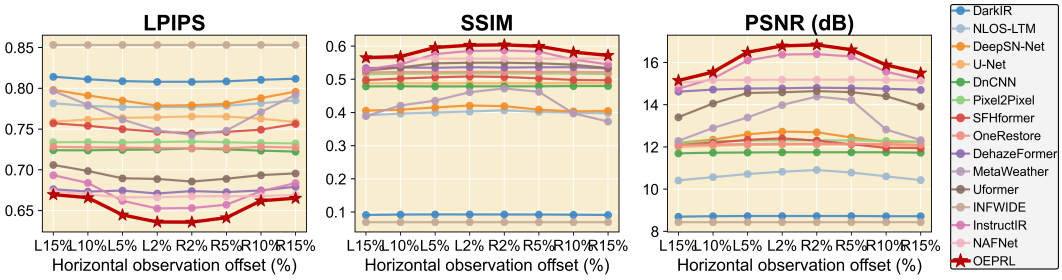

Figure A21: Lock trends under horizontal camera-position perturbations. The curves report LPIPS, SSIM, and PSNR across the conditions in Table A14. Markers denote the evaluated settings.

The Lock results retain this advantage at both ends of the lateral sweep. At the leftmost setting, OEPRL reaches 15.15 dB PSNR with 0.5654 SSIM; at the rightmost setting, it reaches 15.51 dB with 0.5721 SSIM. Together with the corresponding Figure comparison, these endpoint results show that the leading reconstruction extends to displaced observations in either direction. The next image sequence makes the graphical organization associated with these geometric tests visible at the level of individual screen regions.

OEPRL retains recognizable chart-color organization within the bright page as the observation shifts laterally. Together with Figure A19, the example shows recovery from displaced wall evidence along both image axes.

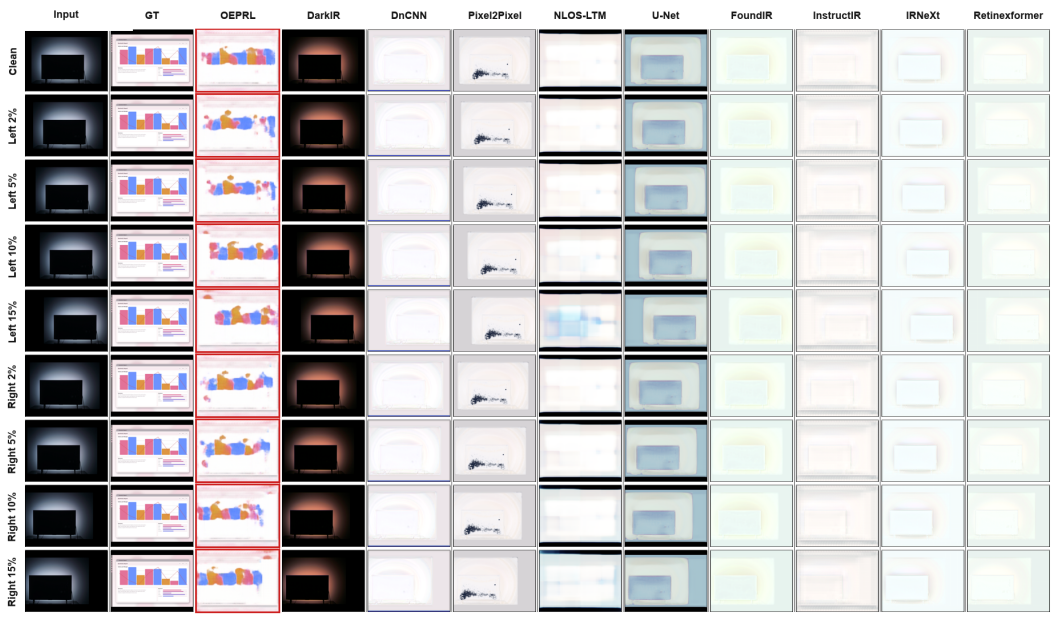

Figure A22: A Figure example under horizontal observation offsets. Rows show the reference, leftward offsets of 2%, 5%, 10%, and 15%, and rightward offsets of 2%, 5%, 10%, and 15%.

C.11 Camera Orientation

Following the displacement tests, we change its projection through pitch and yaw. These rotations test recovery of screen organization from differently oriented wall patterns.

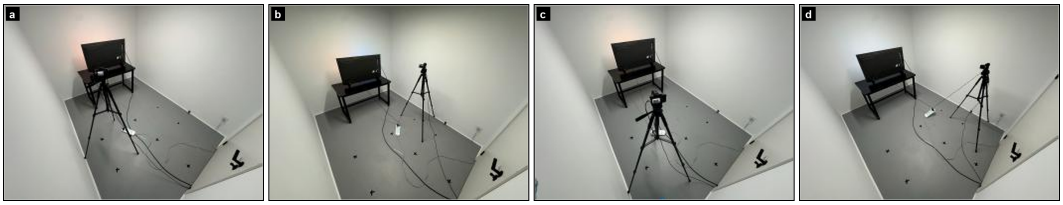

Figure A23: The screen–wall setup under different camera orientations.

The setup views locate the orientation change in the camera's observation of the relay wall. Pitch and yaw vary the projected wall pattern along different axes. The separate Figure and Lock comparisons below follow whether these changes still leave optical evidence for graphical layouts and natural scene organization.

Table A15: Figure point estimates under camera pitch perturbation. Best and second-best values are highlighted in red and blue, respectively. The corresponding trend is shown in Figure A24.

Method	−15°			−10°			−5°			0°			+5°			+10°			+15°		
	LPIPS↓	SSIM↑	PSNR (dB)↑	LPIPS↓	SSIM↑	PSNR (dB)↑	LPIPS↓	SSIM↑	PSNR (dB)↑	LPIPS↓	SSIM↑	PSNR (dB)↑	LPIPS↓	SSIM↑	PSNR (dB)↑	LPIPS↓	SSIM↑	PSNR (dB)↑	LPIPS↓	SSIM↑	PSNR (dB)↑
Passive Non-Line-of-Sight Reconstruction																					
NLOS-LTM	0.7415	0.5271	13.31	0.7398	0.5280	13.33	0.7390	0.5284	13.33	0.7277	0.5334	13.36	0.7385	0.5289	13.29	0.7385	0.5293	13.28	0.7386	0.5295	13.24
All-in-One and Universal Image Restoration																					
InstructIR	0.6344	0.6606	17.67	0.6308	0.6696	17.81	0.6302	0.6731	17.87	0.6207	0.6762	18.01	0.6300	0.6727	18.05	0.6262	0.6649	17.99	0.6258	0.6640	18.05
OneRestore	0.7177	0.5683	12.14	0.7176	0.5683	12.14	0.7176	0.5683	12.14	0.7055	0.5728	12.20	0.7148	0.5687	12.15	0.7156	0.5688	12.16	0.7155	0.5689	12.16
General-Purpose Image Restoration																					
SFHformer	0.7318	0.5738	12.74	0.7298	0.5736	12.72	0.7342	0.5748	12.71	0.7247	0.5791	12.75	0.7372	0.5750	12.69	0.7343	0.5726	12.68	0.7323	0.5709	12.68
Uformer	0.6432	0.6029	17.01	0.6406	0.6029	17.00	0.6408	0.6029	16.99	0.6309	0.6065	17.06	0.6402	0.6022	17.02	0.6384	0.6035	17.05	0.6329	0.6027	17.10
NAFNet	0.6369	0.6369	17.38	0.6352	0.6400	17.34	0.6357	0.6387	17.33	0.6250	0.6399	17.43	0.6334	0.6338	17.44	0.6306	0.6328	17.56	0.6275	0.6316	17.67
DeepSN-Net	0.7107	0.4724	13.62	0.7092	0.4765	13.65	0.7076	0.4768	13.67	0.6970	0.4815	13.72	0.7075	0.4758	13.67	0.7036	0.4750	13.65	0.7012	0.4712	13.59
DnCNN	0.6870	0.5464	13.38	0.6880	0.5498	13.38	0.6871	0.5514	13.39	0.6749	0.5547	13.44	0.6832	0.5491	13.39	0.6833	0.5489	13.40	0.6814	0.5473	13.42
U-Net	0.6955	0.5438	11.38	0.6930	0.5432	11.39	0.6944	0.5434	11.41	0.6833	0.5486	11.44	0.6929	0.5446	11.37	0.6911	0.5438	11.32	0.6935	0.5433	11.29
Related Degradations and Domains																					
INFWIDE	0.7052	0.6734	16.39	0.6403	0.6858	18.22	0.6962	0.6721	16.25	0.6812	0.6816	16.74	0.6868	0.6846	17.14	0.6631	0.6937	18.31	0.6798	0.6831	17.79
MetaWeather	0.6710	0.6440	17.74	0.6689	0.6466	17.75	0.6652	0.6611	17.80	0.6552	0.6650	17.90	0.6651	0.6622	17.89	0.6644	0.6555	17.80	0.6705	0.6498	17.86
Pixel2Pixel	0.6567	0.5935	14.81	0.6573	0.5932	14.83	0.6564	0.5940	14.86	0.6468	0.5981	14.91	0.6569	0.5941	14.85	0.6569	0.5914	14.82	0.6556	0.5901	14.77
DehazeFormer	0.6552	0.6912	18.33	0.6445	0.6915	18.47	0.6351	0.6926	18.56	0.6281	0.6971	18.64	0.6402	0.6955	18.62	0.6484	0.6933	18.41	0.6511	0.6879	18.43
DarkIR	0.9275	0.0382	4.44	0.9267	0.0387	4.45	0.9272	0.0387	4.45	0.9129	0.0477	4.49	0.9263	0.0375	4.43	0.9229	0.0366	4.42	0.9225	0.0357	4.40
OEPRL	0.6240	0.6989	18.44	0.6245	0.6992	18.58	0.5997	0.7003	18.71	0.5849	0.7047	18.90	0.5879	0.7031	19.00	0.6076	0.7013	18.59	0.6161	0.6957	18.56

Orientation changes introduce a different geometric test by altering the projection of the wall pattern. OEPRL leads all three Figure metrics across the pitch settings, while SSIM remains within 0.6957–0.7047. The recovered graphical organization is thus supported across changing projections.

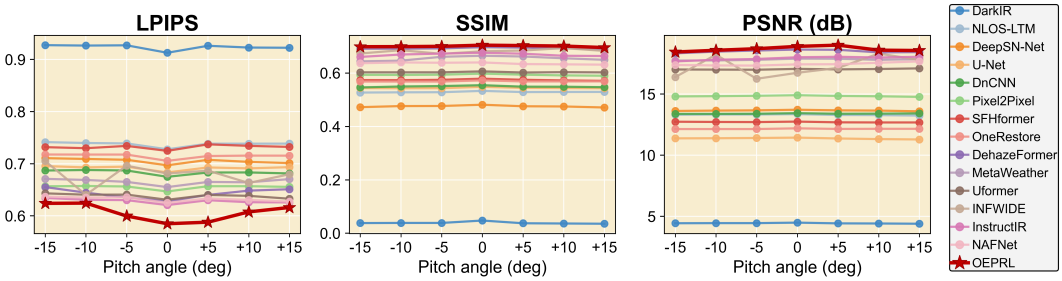

Figure A24: Figure trends under camera pitch perturbations. The curves report LPIPS, SSIM, and PSNR across the conditions in Table A15. Markers denote the evaluated settings.

The Figure curves retain OEPRL's leading position at the reference orientation and at the positive and negative pitch settings. The comparison therefore spans both directions of the projection change. The Lock results below test whether this behavior also appears when the target is organized by natural color regions and foreground structure.

Table A16: Lock point estimates under camera pitch perturbation. Best and second-best values are highlighted in red and blue, respectively. The corresponding trend is shown in Figure A25.

Method	−15°			−10°			−5°			0°			+5°			+10°			+15°		
	LPIPS↓	SSIM↑	PSNR (dB)↑	LPIPS↓	SSIM↑	PSNR (dB)↑	LPIPS↓	SSIM↑	PSNR (dB)↑	LPIPS↓	SSIM↑	PSNR (dB)↑	LPIPS↓	SSIM↑	PSNR (dB)↑	LPIPS↓	SSIM↑	PSNR (dB)↑	LPIPS↓	SSIM↑	PSNR (dB)↑
Passive Non-Line-of-Sight Reconstruction																					
NLOS-LTM	0.7767	0.3988	10.80	0.7766	0.3990	10.81	0.7766	0.4009	10.84	0.7656	0.4111	10.94	0.7779	0.4094	10.94	0.7791	0.4112	10.96	0.7799	0.4130	10.96
All-in-One and Universal Image Restoration																					
InstructIR	0.6713	**0.5596**	**15.33**	0.6717	**0.5650**	**15.53**	**0.6622**	**0.5791**	**16.02**	0.6594	0.5450	15.28	0.6767	0.5017	14.44	0.6965	0.4336	13.28	0.6938	0.4415	13.58
OneRestore	0.7225	0.5230	12.16	0.7236	0.5230	12.16	0.7252	0.5227	12.16	0.7139	0.5271	12.20	0.7244	0.5219	12.15	0.7239	0.5214	12.14	0.7238	0.5209	12.13
General-Purpose Image Restoration																					
SFHformer	0.7419	0.5094	12.40	0.7433	0.5089	12.39	0.7427	0.5090	12.39	0.7316	0.5138	12.44	0.7428	0.5088	12.39	0.7431	0.5072	12.38	0.7457	0.5057	12.36
Uformer	0.6847	0.5439	14.37	0.6808	0.5538	14.70	0.6789	0.5613	14.91	0.6697	0.5634	14.97	0.6809	0.5566	14.94	0.6863	0.5357	14.26	0.6972	0.5167	13.51
NAFNet	**0.6681**	0.5566	15.12	**0.6697**	0.5598	15.16	0.6685	0.5610	15.18	**0.6589**	**0.5651**	15.24	**0.6694**	**0.5604**	15.19	**0.6720**	**0.5586**	15.16	**0.6694**	**0.5610**	**15.01**
DeepSN-Net	0.7732	0.4185	12.68	0.7742	0.4200	12.70	0.7752	0.4213	12.72	0.7623	0.4281	12.80	0.7726	0.4233	12.78	0.7744	0.4225	12.78	0.7777	0.4218	12.76
DnCNN	0.7227	0.4802	11.77	0.7237	0.4798	11.76	0.7250	0.4795	11.76	0.7141	0.4841	11.80	0.7248	0.4782	11.74	0.7241	0.4772	11.73	0.7234	0.4764	11.72
U-Net	0.7646	0.4875	12.09	0.7642	0.4872	12.08	0.7649	0.4873	12.08	0.7532	0.4923	12.14	0.7645	0.4870	12.09	0.7636	0.4871	12.11	0.7601	0.4871	12.10
Related Degradations and Domains																					
INFWIDE	0.7390	0.5057	12.48	0.7353	0.5080	12.49	0.7370	0.5085	12.50	0.7255	0.5113	12.57	0.7362	0.5041	12.53	0.7356	0.4973	12.53	0.7356	0.4885	12.51
MetaWeather	0.7320	0.5038	15.03	0.7238	0.5143	15.33	0.7255	0.5155	15.33	0.7106	0.5205	**15.48**	0.7174	0.5159	**15.53**	0.7190	0.5035	**15.25**	0.7243	0.4836	14.63
Pixel2Pixel	0.7323	0.5185	12.33	0.7327	0.5183	12.33	0.7331	0.5180	12.32	0.7225	0.5224	12.36	0.7338	0.5171	12.31	0.7332	0.5163	12.29	0.7329	0.5155	12.28
DehazeFormer	0.6688	0.5320	14.76	0.6700	0.5353	14.74	0.6710	0.5368	14.76	0.6609	0.5383	14.83	0.6710	0.5305	14.80	**0.6720**	0.5238	14.80	0.6739	0.5221	14.79
DarkIR	0.8054	0.0932	8.74	0.8065	0.0931	8.74	0.8076	0.0929	8.74	0.7952	0.1017	8.78	0.8070	0.0924	8.72	0.8058	0.0919	8.71	0.8045	0.0914	8.70
OEPRL	**0.6615**	**0.5840**	**15.42**	**0.6629**	**0.5840**	**15.62**	**0.6401**	**0.6120**	**16.54**	**0.6342**	**0.5946**	**16.09**	**0.6476**	**0.5714**	**15.62**	**0.6593**	**0.5697**	**15.34**	**0.6530**	**0.5720**	**15.37**

The same comparative advantage holds across every pitch setting on Lock. The orientation result therefore extends from regular graphical regions to natural foreground–background organization.

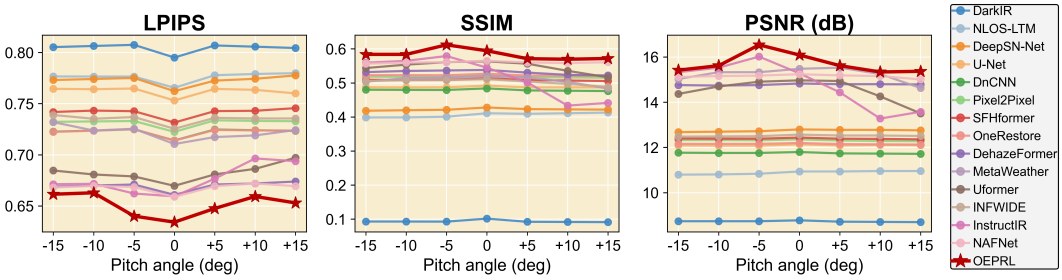

Figure A25: Lock trends under camera pitch perturbations. The curves report LPIPS, SSIM, and PSNR across the conditions in Table A16. Markers denote the evaluated settings.

The pitch comparison spans the reference orientation and both signs of rotation. On Figure, OEPRL's PSNR remains between 18.44 and 19.00 dB across the tested angles. On Lock, the corresponding range is 15.34–16.54 dB, with OEPRL leading each condition in all three metrics. These two content cases connect the orientation result to both regular graphical structure and natural image organization. The following Figure sequence shows the graphical regions recovered from the differently projected wall patterns.

The colored graphical regions remain recognizable within the dark interface as the wall projection changes. The image sequence extends the displacement result to changes in viewing orientation.

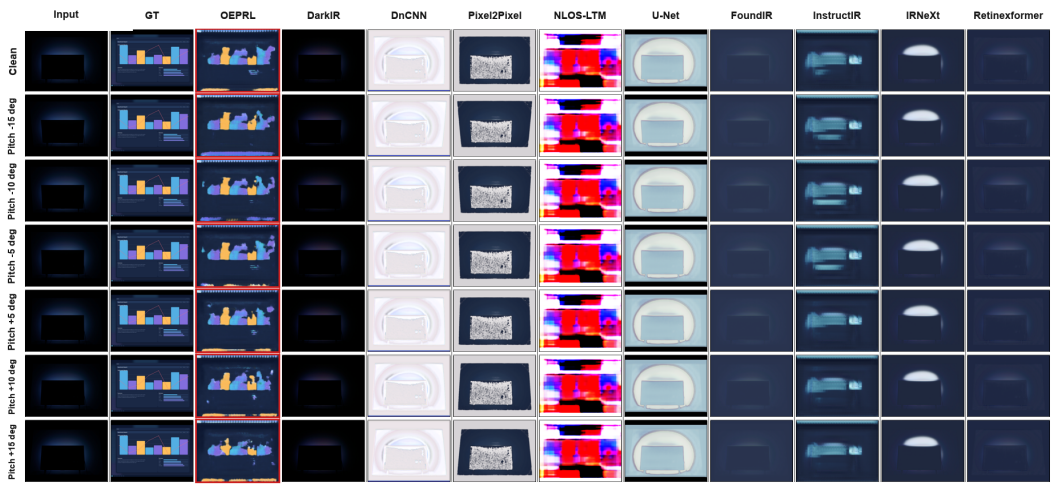

Figure A26: A Figure example under pitch perturbations. The reference is followed by −15°, −10°, −5°, +5°, +10°, and +15° settings.

Yaw provides the complementary orientation test. Rotating along the second axis changes the projected wall pattern; the Figure comparison below follows the recovered graphical organization across that change.

Table A17: Figure point estimates under camera yaw perturbation. Best and second-best values are highlighted in red and blue, respectively. The corresponding trend is shown in Figure A27.

Method	−15°			−10°			−5°			0°			+5°			+10°			+15°		
	LPIPS↓	SSIM↑	PSNR (dB)↑	LPIPS↓	SSIM↑	PSNR (dB)↑	LPIPS↓	SSIM↑	PSNR (dB)↑	LPIPS↓	SSIM↑	PSNR (dB)↑	LPIPS↓	SSIM↑	PSNR (dB)↑	LPIPS↓	SSIM↑	PSNR (dB)↑	LPIPS↓	SSIM↑	PSNR (dB)↑
Passive Non-Line-of-Sight Reconstruction																					
NLOS-LTM	0.7356	0.5351	13.53	0.7365	0.5327	13.46	0.7371	0.5309	13.41	0.7280	0.5333	13.35	0.7410	0.5263	13.20	0.7432	0.5248	13.10	0.7461	0.5228	12.98
All-in-One and Universal Image Restoration																					
InstructIR	**0.6320**	0.6654	17.92	**0.6319**	0.6678	17.92	**0.6312**	0.6724	17.95	**0.6204**	0.6749	18.00	**0.6284**	0.6708	17.95	0.6329	0.6659	17.93	0.6314	0.6621	17.91
OneRestore	0.7213	0.5692	12.15	0.7210	0.5691	12.15	0.7194	0.5688	12.15	0.7073	0.5732	12.20	0.7168	0.5689	12.15	0.7183	0.5691	12.15	0.7180	0.5697	12.16
General-Purpose Image Restoration																					
SFHformer	0.7357	0.5721	12.65	0.7362	0.5744	12.66	0.7388	0.5747	12.68	0.7271	0.5785	12.75	0.7375	0.5737	12.73	0.7370	0.5736	12.73	0.7361	0.5736	12.74
Uformer	0.6475	0.6041	16.99	0.6470	0.6039	17.00	0.6438	0.6038	17.00	0.6338	0.6077	17.05	0.6430	0.6036	17.00	0.6447	0.6037	17.00	0.6431	0.6035	16.99
NAFNet	0.6390	0.6356	17.49	0.6401	0.6370	17.41	0.6376	0.6372	17.37	0.6255	0.6399	17.43	0.6325	0.6354	17.38	**0.6318**	0.6355	17.44	**0.6307**	0.6347	17.51
DeepSN-Net	0.7096	0.4762	13.61	0.7086	0.4763	13.64	0.7110	0.4774	13.67	0.6977	0.4817	13.71	0.7056	0.4756	13.64	0.7091	0.4761	13.62	0.7065	0.4739	13.59
DnCNN	0.6955	0.5519	13.36	0.6913	0.5513	13.37	0.6901	0.5500	13.38	0.6779	0.5549	13.44	0.6864	0.5508	13.39	0.6910	0.5510	13.39	0.6931	0.5523	13.37
U-Net	0.7013	0.5447	11.38	0.6955	0.5451	11.40	0.6951	0.5443	11.39	0.6840	0.5494	11.45	0.6938	0.5454	11.40	0.7001	0.5436	11.36	0.7035	0.5439	11.36
Related Degradations and Domains																					
INFWIDE	0.6961	0.6697	16.86	0.6947	0.6779	17.41	0.6889	0.6835	17.56	0.6767	0.6871	17.75	0.6852	0.6844	17.85	0.7127	0.6624	16.52	0.7019	**0.6779**	17.41
MetaWeather	0.6794	0.6279	18.02	0.6720	0.6431	17.99	0.6656	0.6621	17.91	0.6551	0.6647	17.97	0.6645	0.6605	17.94	0.6697	0.6511	17.98	0.6722	0.6394	**17.99**
Pixel2Pixel	0.6654	0.5965	14.77	0.6629	0.5955	14.81	0.6587	0.5946	14.84	0.6495	0.5982	14.90	0.6602	0.5937	14.86	0.6614	0.5927	14.83	0.6659	0.5922	14.77
DehazeFormer	0.6498	**0.6838**	**18.12**	0.6506	**0.6867**	**18.15**	0.6446	**0.6897**	**18.35**	0.6343	**0.6926**	**18.43**	0.6432	**0.6892**	**18.40**	0.6565	**0.6852**	**18.11**	0.6615	0.6752	17.85
DarkIR	0.9342	0.0380	4.43	0.9340	0.0382	4.44	0.9284	0.0382	4.44	0.9135	0.0477	4.49	0.9264	0.0380	4.44	0.9276	0.0376	4.43	0.9299	0.0371	4.42
OEPRL	**0.6138**	**0.6917**	**18.46**	**0.6082**	**0.6945**	**18.63**	**0.5883**	**0.6979**	**18.99**	**0.5803**	**0.7018**	**19.01**	**0.5899**	**0.6996**	**18.93**	**0.6094**	**0.6930**	**18.50**	**0.6191**	**0.6859**	**18.32**

OEPRL remains first in all Figure metrics across the full set of angles, preserving its graphical-content advantage as the wall projection changes along the second rotation axis.

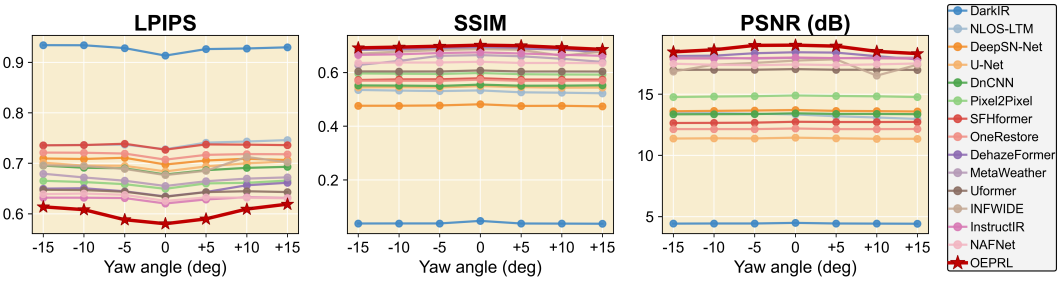

Figure A27: Figure trends under camera yaw perturbations. The curves report LPIPS, SSIM, and PSNR across the conditions in Table A17. Markers denote the evaluated settings.

Across the tested yaw angles, OEPRL's Figure PSNR ranges from 18.32 to 19.01 dB, reflecting angle-dependent variation in reconstruction accuracy.

The yaw curves show how the graphical-content comparison evolves across the second rotation axis. OEPRL remains first as the projection departs from the reference in either direction. The next table tests this orientation change on Lock, complementing the Figure result with natural screen imagery.

Table A18: Lock point estimates under camera yaw perturbation. Best and second-best values are highlighted in red and blue, respectively. The corresponding trend is shown in Figure A28.

Method	−15°			−10°			−5°			0°			+5°			+10°			+15°		
	LPIPS↓	SSIM↑	PSNR (dB)↑	LPIPS↓	SSIM↑	PSNR (dB)↑	LPIPS↓	SSIM↑	PSNR (dB)↑	LPIPS↓	SSIM↑	PSNR (dB)↑	LPIPS↓	SSIM↑	PSNR (dB)↑	LPIPS↓	SSIM↑	PSNR (dB)↑	LPIPS↓	SSIM↑	PSNR (dB)↑
Passive Non-Line-of-Sight Reconstruction																					
NLOS-LTM	0.7776	0.3963	10.72	0.7772	0.3977	10.77	0.7770	0.4000	10.81	0.7654	0.4094	10.91	0.7771	0.4069	10.91	0.7775	0.4101	10.94	0.7779	0.4135	10.96
All-in-One and Universal Image Restoration																					
InstructIR	0.6699	0.5339	15.43	0.6658	0.5471	15.65	0.6564	0.5716	16.15	0.6451	0.5838	16.33	0.6534	0.5876	16.41	0.6535	0.5811	16.35	0.6604	0.5610	15.95
OneRestore	0.7259	0.5224	12.15	0.7263	0.5224	12.15	0.7258	0.5224	12.15	0.7148	0.5272	12.20	0.7256	0.5225	12.15	0.7263	0.5226	12.15	0.7254	0.5227	12.15
General-Purpose Image Restoration																					
SFHformer	0.7467	0.5074	12.40	0.7440	0.5075	12.40	0.7439	0.5088	12.40	0.7335	0.5145	12.44	0.7454	0.5103	12.38	0.7443	0.5073	12.33	0.7442	0.5045	12.27
Uformer	0.6918	0.5361	14.34	0.6869	0.5456	14.73	0.6800	0.5579	15.01	0.6717	0.5637	15.02	0.6838	0.5607	14.94	0.6908	0.5468	14.49	0.6875	0.5410	14.42
NAFNet	0.6733	0.5574	15.17	0.6714	0.5580	15.18	0.6687	0.5601	15.18	0.6585	0.5656	15.24	0.6683	0.5623	15.19	0.6699	0.5607	15.19	0.6702	0.5598	15.18
DeepSN-Net	0.7762	0.4196	12.73	0.7748	0.4207	12.75	0.7751	0.4218	12.76	0.7643	0.4278	12.80	0.7769	0.4221	12.74	0.7758	0.4198	12.69	0.7746	0.4164	12.61
DnCNN	0.7242	0.4791	11.75	0.7244	0.4790	11.75	0.7246	0.4789	11.75	0.7144	0.4841	11.80	0.7260	0.4788	11.75	0.7259	0.4790	11.75	0.7255	0.4792	11.74
U-Net	0.7621	0.4874	12.08	0.7637	0.4875	12.09	0.7641	0.4874	12.10	0.7533	0.4926	12.15	0.7655	0.4875	12.11	0.7658	0.4877	12.10	0.7652	0.4878	12.09
Related Degradations and Domains																					
INFWIDE	0.7409	0.5042	12.51	0.7419	0.5043	12.52	0.7369	0.5050	12.53	0.7261	0.5103	12.57	0.7374	0.5058	12.51	0.7414	0.5043	12.46	0.7409	0.5030	12.40
MetaWeather	0.7454	0.4641	14.10	0.7383	0.4795	14.53	0.7247	0.5066	15.29	0.7133	0.5133	15.43	0.7236	0.5102	15.47	0.7347	0.4857	14.85	0.7414	0.4629	14.32
Pixel2Pixel	0.7326	0.5175	12.30	0.7341	0.5175	12.31	0.7336	0.5176	12.31	0.7231	0.5224	12.36	0.7346	0.5177	12.31	0.7331	0.5177	12.31	0.7330	0.5178	12.30
DehazeFormer	0.6709	0.5281	14.78	0.6689	0.5314	14.78	0.6697	0.5341	14.79	0.6621	0.5400	14.85	0.6746	0.5366	14.81	0.6746	0.5317	14.80	0.6723	0.5290	14.78
DarkIR	0.8061	0.0926	8.73	0.8068	0.0928	8.73	0.8070	0.0928	8.73	0.7955	0.1017	8.78	0.8083	0.0925	8.73	0.8081	0.0922	8.72	0.8070	0.0918	8.72
OEPRL	0.6506	0.5759	15.71	0.6455	0.5815	15.90	0.6366	0.5982	16.40	0.6256	0.6111	16.71	0.6336	0.6161	16.92	0.6373	0.6099	16.74	0.6399	0.6009	16.42

OEPRL also ranks first across all yaw settings on Lock. Combined with pitch, the yaw results show that the reconstruction advantage spans different viewing orientations and both graphical and natural screen content.

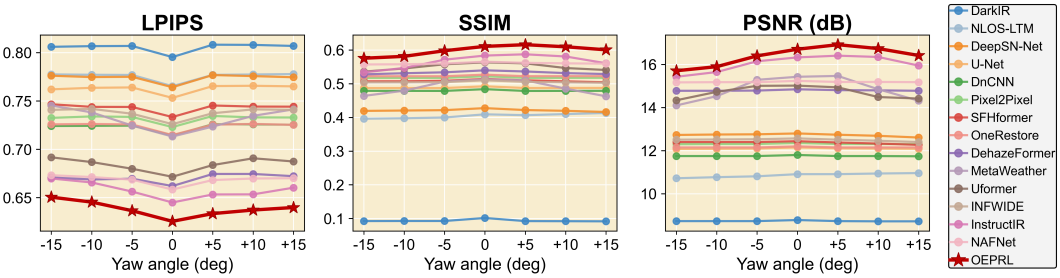

Figure A28: Lock trends under camera yaw perturbations. The curves report LPIPS, SSIM, and PSNR across the conditions in Table A18. Markers denote the evaluated settings.

In the Lock example (Figure A29), the broad blue and warm-toned regions and the central foreground arrangement remain visible across the yaw settings. This extends the orientation comparison from graphical interfaces to natural screen imagery.

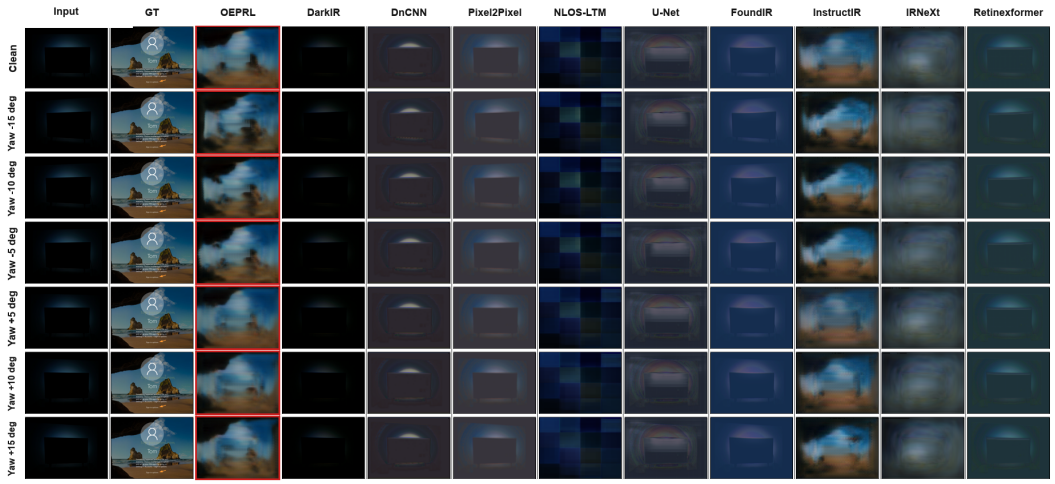

Figure A29: A Lock example under yaw perturbations. The reference is followed by −15°, −10°, −5°, +5°, +10°, and +15° settings.

C.12 Ambient-Light Direction

Ambient-light direction changes the spatial interference superposed on the screen-induced wall pattern. B and T denote illumination from below and above, while L and R denote illumination from the left and right; the numerical suffix denotes perturbation strength. The vertical and horizontal sweeps test recovery when directional ambient interference is mixed with the screen-induced light.

Table A19: Figure point estimates under vertical directional-light perturbations. Best and second-best values are highlighted in red and blue, respectively. The corresponding trend is shown in Figure A30.

Method	B40			B30			B20			B10			T10			T20			T30			T40		
	LPIPS↓	SSIM↑	PSNR (dB)↑	LPIPS↓	SSIM↑	PSNR (dB)↑	LPIPS↓	SSIM↑	PSNR (dB)↑	LPIPS↓	SSIM↑	PSNR (dB)↑	LPIPS↓	SSIM↑	PSNR (dB)↑	LPIPS↓	SSIM↑	PSNR (dB)↑	LPIPS↓	SSIM↑	PSNR (dB)↑	LPIPS↓	SSIM↑	PSNR (dB)↑
Passive Non-Line-of-Sight Reconstruction																								
NLOS-LTM	0.8046	0.4797	10.15	0.8119	0.4823	9.99	0.8084	0.4883	10.24	0.7700	0.5066	11.70	0.7505	0.5232	12.71	0.7575	0.5195	12.28	0.7670	0.5110	11.56	0.7742	0.5020	10.91
All-in-One and Universal Image Restoration																								
InstructIR	**0.6336**	0.6723	17.75	**0.6336**	0.6733	17.81	0.6331	0.6742	17.88	0.6335	0.6750	17.94	0.6328	0.6756	17.94	**0.6322**	0.6754	17.89	**0.6323**	0.6750	17.83	**0.6323**	0.6741	17.76
OneRestore	0.7164	0.5633	12.01	0.7169	0.5646	12.05	0.7174	0.5659	12.08	0.7179	0.5673	12.12	0.7178	0.5676	12.11	0.7167	0.5666	12.07	0.7167	0.5656	12.03	0.7164	0.5644	11.99
General-Purpose Image Restoration																								
SFHformer	0.7368	0.5747	12.67	0.7370	0.5752	12.68	0.7365	0.5756	12.69	0.7367	0.5762	12.69	0.7365	0.5763	12.70	0.7363	0.5760	12.70	0.7363	0.5756	12.70	0.7361	0.5753	12.71
Uformer	0.6440	0.5962	16.75	0.6433	0.5985	16.82	0.6430	0.6005	16.89	0.6430	0.6024	16.93	0.6434	0.6023	16.90	0.6436	0.6001	16.82	0.6445	0.5982	16.72	0.6451	0.5963	16.65
NAFNet	0.6434	0.6574	16.88	0.6420	0.6533	16.94	0.6401	0.6478	17.05	0.6382	0.6415	17.19	0.6384	0.6424	17.17	0.6407	0.6500	17.02	0.6427	0.6556	16.92	0.6443	0.6600	16.86
DeepSN-Net	0.7136	0.4849	13.85	0.7123	0.4847	13.82	0.7116	0.4839	13.79	0.7107	0.4828	13.75	0.7111	0.4828	13.74	0.7114	0.4831	13.77	0.7132	0.4834	13.80	0.7139	0.4831	13.82
DnCNN	0.6978	0.5426	13.00	0.6961	0.5402	13.00	0.6972	0.5485	13.03	0.6964	0.5500	13.09	0.7006	0.5497	13.06	0.6981	0.5497	13.01	0.6993	0.5446	12.97	0.7020	0.5483	12.94
U-Net	0.7044	0.5400	11.92	0.6959	0.5422	11.52	0.6925	0.5434	11.42	0.6909	0.5458	11.44	0.6926	0.5458	11.43	0.6939	0.5446	11.44	0.6966	0.5421	11.47	0.7008	0.5397	11.62
Related Degradations and Domains																								
INFWIDE	0.6473	0.6796	17.52	0.6422	0.6847	17.74	0.6364	0.6910	18.04	0.6351	**0.7013**	18.63	0.6351	**0.7018**	18.67	0.6362	0.6903	18.00	0.6408	0.6836	17.67	0.6477	0.6760	17.39
MetaWeather	0.6695	0.6664	17.86	0.6684	0.6673	17.89	0.6678	0.6677	17.91	0.6670	0.6678	17.92	0.6672	0.6677	17.93	0.6674	0.6676	17.93	0.6684	0.6670	17.93	0.6696	0.6660	17.93
Pixel2Pixel	0.6852	0.5899	14.21	0.6823	0.5925	14.29	0.6782	0.5940	14.41	0.6721	0.6004	14.62	0.6736	0.5949	14.59	0.6775	0.5877	14.38	0.6853	0.5861	14.26	0.6880	0.5841	14.18
DehazeFormer	0.6428	**0.6994**	**18.47**	0.6383	**0.7005**	**18.61**	**0.6330**	**0.7001**	**18.71**	**0.6305**	0.6986	**18.75**	**0.6306**	0.6989	**18.73**	0.6332	**0.6999**	**18.67**	0.6383	**0.6998**	**18.53**	0.6419	**0.6979**	**18.40**
DarkIR	0.9294	0.0510	4.57	0.9286	0.0471	4.53	0.9280	0.0435	4.50	0.9274	0.0405	4.47	0.9283	0.0408	4.47	0.9294	0.0439	4.51	0.9308	0.0476	4.54	0.9325	0.0516	4.58
OEPRL	0.5883	0.7069	19.00	0.5814	0.7079	19.11	0.5787	0.7076	19.20	0.5757	0.7088	19.24	0.5760	0.7093	19.23	0.5787	0.7074	19.16	0.5809	0.7073	19.08	0.5838	0.7054	18.92

Screen information remains recoverable when directional ambient light adds a second illumination pattern to the wall. OEPRL leads every Figure condition, with SSIM within 0.7054–0.7093 across top- and bottom-originating perturbations. The principal graphical organization remains supported despite the changing background illumination.

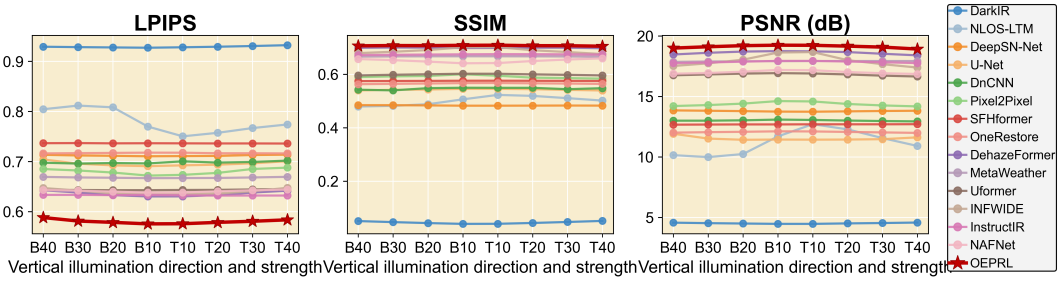

Figure A30: Figure trends under vertical directional-light perturbations. The curves report LPIPS, SSIM, and PSNR across the conditions in Table A19. Markers denote the evaluated settings.

For OEPRL, each metric changes within a narrow range across the illumination strengths, consistent with the stable structural agreement. The comparison covers interference arriving from both above and below. The Lock results that follow examine the same directions for natural imagery, where smooth backgrounds and salient subjects provide a complementary recovery target.

Table A20: Lock point estimates under vertical directional-light perturbations. Best and second-best values are highlighted in red and blue, respectively. The corresponding trend is shown in Figure A31.

Method	B40			B30			B20			B10			T10			T20			T30			T40		
	LPIPS↓	SSIM↑	PSNR (dB)↑	LPIPS↓	SSIM↑	PSNR (dB)↑	LPIPS↓	SSIM↑	PSNR (dB)↑	LPIPS↓	SSIM↑	PSNR (dB)↑	LPIPS↓	SSIM↑	PSNR (dB)↑	LPIPS↓	SSIM↑	PSNR (dB)↑	LPIPS↓	SSIM↑	PSNR (dB)↑	LPIPS↓	SSIM↑	PSNR (dB)↑
Passive Non-Line-of-Sight Reconstruction																								
NLOS-LTM	0.7816	0.4011	10.30	0.7784	0.4098	10.49	0.7734	0.3996	10.62	0.7787	0.3268	9.96	0.7860	0.2906	9.59	0.7834	0.4049	10.69	0.7954	0.4514	11.08	0.8008	0.4516	10.69
All-in-One and Universal Image Restoration																								
InstructIR	**0.7124**	0.5360	14.16	**0.6834**	**0.5548**	15.04	**0.6640**	**0.5719**	**15.81**	**0.6598**	**0.5641**	**15.90**	**0.6638**	**0.5762**	**16.00**	**0.6716**	**0.5669**	15.52	**0.6825**	**0.5564**	14.96	0.7066	0.5391	14.21
OneRestore	0.7275	0.5202	12.11	0.7266	0.5208	12.12	0.7257	0.5213	12.13	0.7247	0.5219	12.14	0.7246	0.5220	12.15	0.7260	0.5216	12.14	0.7268	0.5211	12.13	0.7278	0.5206	12.12
General-Purpose Image Restoration																								
SFHformer	0.7502	0.4992	12.14	0.7483	0.5022	12.22	0.7468	0.5049	12.29	0.7451	0.5074	12.35	0.7446	0.5070	12.34	0.7461	0.5042	12.27	0.7472	0.5013	12.20	0.7485	0.4982	12.13
Uformer	0.7156	**0.5407**	13.87	0.7046	0.5491	14.35	0.6925	0.5567	14.75	0.6839	0.5618	14.96	0.6837	0.5639	15.03	0.6908	0.5598	14.83	0.7015	0.5549	14.58	0.7132	**0.5484**	14.22
NAFNet	0.7288	0.5283	13.41	0.7083	0.5402	14.14	0.6897	0.5504	14.73	0.6751	0.5577	15.07	0.6749	0.5571	15.08	0.6885	0.5489	14.71	0.7063	0.5384	14.10	0.7252	0.5253	13.31
DeepSN-Net	0.7853	0.4186	12.47	0.7815	0.4233	12.64	0.7767	0.4258	12.77	0.7747	0.4253	12.79	0.7752	0.4222	12.72	0.7780	0.4199	12.65	0.7821	0.4164	12.53	0.7878	0.4103	12.36
DnCNN	0.7247	0.4742	11.79	0.7309	0.4752	11.77	0.7248	0.4775	11.76	0.7224	0.4777	11.73	0.7235	0.4782	11.73	0.7259	0.4786	11.77	0.7309	0.4763	11.79	0.7315	0.4753	11.81
U-Net	0.8075	0.4668	11.61	0.8135	0.4640	11.51	0.8104	0.4650	11.51	0.7866	0.4801	11.96	0.7817	0.4814	11.98	0.7961	0.4750	11.78	0.8004	0.4728	11.79	0.8010	0.4714	11.80
Related Degradations and Domains																								
INFWIDE	0.7398	0.4985	12.25	0.7404	0.5017	12.38	0.7368	0.5048	12.48	0.7351	0.5048	12.52	0.7356	0.5109	12.48	0.7375	0.5104	12.41	0.7405	0.5098	12.31	0.7413	0.5086	12.20
MetaWeather	0.7211	0.5021	**15.26**	0.7212	0.5049	**15.34**	0.7195	0.5105	15.47	0.7207	0.5095	15.48	0.7155	0.5398	15.93	0.7157	0.5432	**15.98**	0.7204	0.5424	**15.92**	0.7252	0.5407	**15.87**
Pixel2Pixel	0.7774	0.5141	12.14	0.7722	0.5148	12.18	0.7615	0.5155	12.22	0.7500	0.5164	12.26	0.7497	0.5164	12.27	0.7582	0.5158	12.23	0.7699	0.5152	12.19	0.7770	0.5147	12.16
DehazeFormer	0.7133	0.5112	13.83	0.6939	0.5272	14.53	0.6802	0.5384	14.88	0.6735	0.5425	14.93	0.6723	0.5433	14.93	0.6768	0.5415	14.88	0.6855	0.5324	14.56	**0.6999**	0.5190	13.92
DarkIR	0.8145	0.1086	8.82	0.8124	0.1049	8.79	0.8103	0.1008	8.77	0.8083	0.0963	8.75	0.8083	0.0961	8.75	0.8100	0.0998	8.78	0.8120	0.1034	8.81	0.8144	0.1065	8.84
OEPRL	0.7053	0.5522	15.36	0.6766	0.5669	15.48	0.6482	0.5915	15.98	0.6361	0.5974	16.11	0.6394	0.6072	16.19	0.6548	0.5922	16.13	0.6757	0.5759	16.04	0.6929	0.5597	15.96

The advantage also holds for Lock at every direction and strength. Recovery therefore extends to observations containing both screen-induced light and directional ambient interference.

The natural-content comparison includes the strongest perturbation from each side of the vertical sweep. OEPRL reaches 15.36 dB PSNR for B40 and 15.96 dB for T40, remaining first in LPIPS, SSIM, and PSNR at both settings. The curves below place these endpoint results alongside the intermediate strengths and connect the numerical comparison to the full tested range of directional interference.

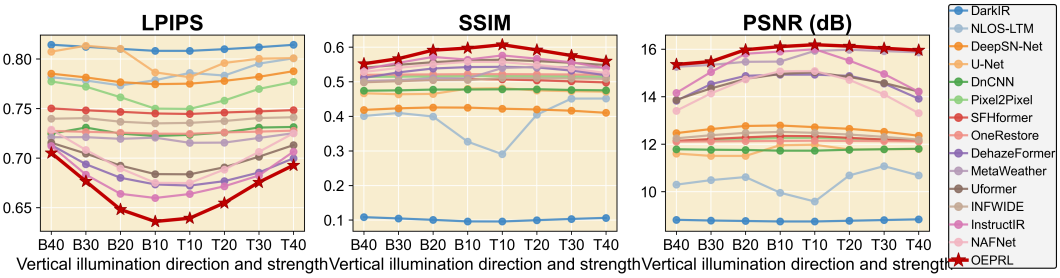

Figure A31: Lock trends under vertical directional-light perturbations. The curves report LPIPS, SSIM, and PSNR across the conditions in Table A20. Markers denote the evaluated settings.

In the Figure example (Figure A32), colored chart regions remain distinct within the bright page while directional illumination changes the wall background. The visible separation of these regions connects ambient-light robustness to the recovery of actual screen content.

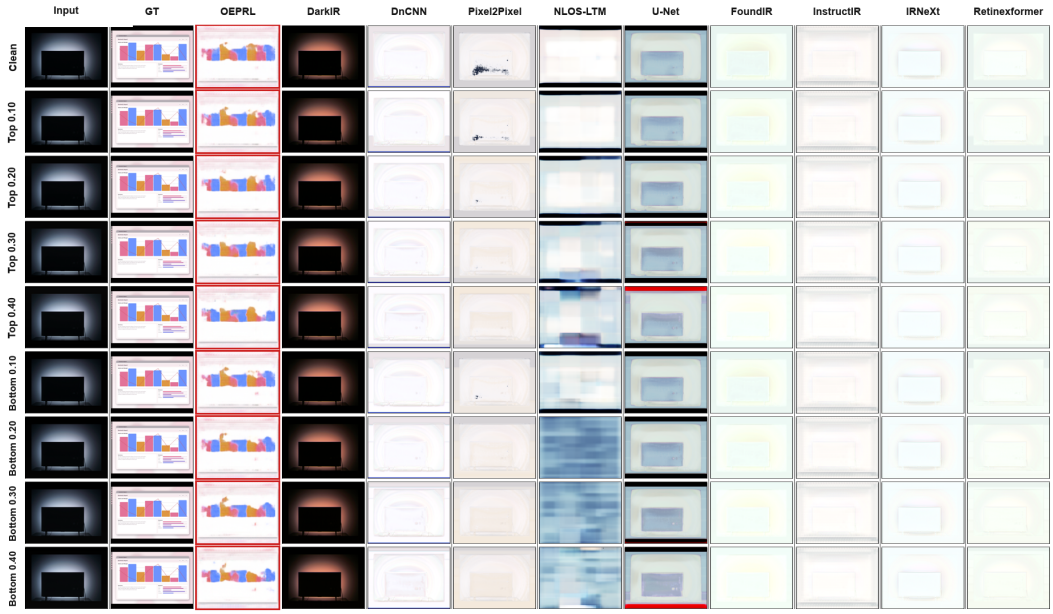

Figure A32: A Figure example under top- and bottom-originating ambient-light perturbations. Rows show the reference followed by the four strengths for each direction.

The horizontal sweep changes the spatial distribution of the ambient interference.

Table A21: Figure point estimates under horizontal directional-light perturbations. Best and second-best values are highlighted in red and blue, respectively. The corresponding trend is shown in Figure A33.

Method	L40			L30			L20			L10			R10			R20			R30			R40		
	LPIPS↓	SSIM↑	PSNR (dB)↑	LPIPS↓	SSIM↑	PSNR (dB)↑	LPIPS↓	SSIM↑	PSNR (dB)↑	LPIPS↓	SSIM↑	PSNR (dB)↑	LPIPS↓	SSIM↑	PSNR (dB)↑	LPIPS↓	SSIM↑	PSNR (dB)↑	LPIPS↓	SSIM↑	PSNR (dB)↑	LPIPS↓	SSIM↑	PSNR (dB)↑
Passive Non-Line-of-Sight Reconstruction																								
NLOS-LTM	0.7983	0.4733	9.56	0.7955	0.4822	10.01	0.7909	0.4922	10.64	0.7672	0.5102	11.88	0.7517	0.5207	12.62	0.7587	0.5197	12.31	0.7637	0.5168	12.01	0.7677	0.5133	11.72
All-in-One and Universal Image Restoration																								
InstructIR	**0.6327**	0.6730	17.77	**0.6326**	0.6739	17.83	**0.6329**	0.6748	17.89	0.6331	0.6752	17.95	0.6332	0.6755	17.95	**0.6330**	0.6751	17.89	**0.6329**	0.6744	17.82	**0.6333**	0.6736	17.75
OneRestore	0.7165	0.5632	12.01	0.7166	0.5646	12.04	0.7173	0.5660	12.08	0.7177	0.5674	12.11	0.7179	0.5675	12.11	0.7173	0.5664	12.07	0.7171	0.5654	12.04	0.7174	0.5645	12.00
General-Purpose Image Restoration																								
SFHformer	0.7362	0.5752	12.72	0.7359	0.5755	12.71	0.7363	0.5759	12.71	0.7361	0.5763	12.71	0.7365	0.5762	12.69	0.7372	0.5757	12.68	0.7377	0.5753	12.67	0.7375	0.5749	12.66
Uformer	0.6458	0.5970	16.71	0.6447	0.5986	16.78	0.6442	0.6007	16.86	0.6434	0.6026	16.92	0.6432	0.6023	16.92	0.6432	0.6001	16.85	0.6439	0.5976	16.76	0.6446	0.5955	16.67
NAFNet	0.6439	0.6580	16.88	0.6422	0.6539	16.94	0.6407	0.6485	17.03	0.6382	0.6417	17.18	0.6384	0.6420	17.18	0.6406	0.6494	17.02	0.6429	0.6549	16.93	0.6446	0.6593	16.87
DeepSN-Net	0.7144	0.4831	13.81	0.7131	0.4833	13.80	0.7118	0.4832	13.77	0.7109	0.4826	13.74	0.7110	0.4829	13.75	0.7118	0.4838	13.79	0.7132	0.4840	13.81	0.7143	0.4840	13.84
DnCNN	0.6972	0.5464	13.10	0.6967	0.5478	13.08	0.6962	0.5494	13.09	0.6950	0.5496	13.11	0.6967	0.5503	13.10	0.6971	0.5493	13.07	0.6979	0.5479	13.07	0.6982	0.5462	13.08
U-Net	0.7010	0.5414	11.77	0.7002	0.5404	11.49	0.6967	0.5442	11.43	0.6908	0.5457	11.44	0.6926	0.5460	11.43	0.6940	0.5443	11.43	0.6973	0.5397	11.44	0.7020	0.5406	11.65
Related Degradations and Domains																								
INFWIDE	0.6471	0.6787	17.51	0.6412	0.6836	17.69	0.6368	0.6911	18.04	0.6354	**0.7011**	18.63	0.6356	**0.7014**	18.64	0.6360	0.6909	18.03	0.6391	0.6845	17.72	0.6448	0.6790	17.51
MetaWeather	0.6692	0.6670	17.90	0.6683	0.6677	17.92	0.6674	0.6679	17.93	0.6675	0.6679	17.93	0.6672	0.6677	17.93	0.6675	0.6675	17.92	0.6685	0.6668	17.92	0.6701	0.6657	17.91
Pixel2Pixel	0.6828	0.5870	14.18	0.6790	0.5892	14.26	0.6741	0.5941	14.39	0.6647	0.6018	14.60	0.6682	0.5968	14.55	0.6757	0.5924	14.34	0.6801	0.5871	14.22	0.6872	0.5853	14.15
DehazeFormer	0.6407	**0.6990**	**18.49**	0.6366	**0.6999**	**18.61**	0.6330	**0.7000**	**18.70**	**0.6298**	0.6987	**18.74**	**0.6308**	0.6986	**18.73**	0.6345	**0.6999**	**18.68**	0.6385	**0.6998**	**18.56**	0.6421	**0.6983**	**18.42**
DarkIR	0.9335	0.0511	4.57	0.9314	0.0473	4.54	0.9306	0.0437	4.50	0.9288	0.0406	4.47	0.9276	0.0409	4.47	0.9279	0.0443	4.51	0.9281	0.0480	4.54	0.9287	0.0520	4.57
OEPRL	**0.5837**	**0.7065**	**19.06**	**0.5795**	**0.7074**	**19.15**	**0.5764**	**0.7075**	**19.22**	**0.5749**	**0.7085**	**19.26**	**0.5755**	**0.7089**	**19.26**	**0.5774**	**0.7074**	**19.19**	**0.5808**	**0.7073**	**19.13**	**0.5850**	**0.7058**	**19.03**

OEPRL leads every Figure metric, and SSIM remains within 0.7058–0.7089 under both left- and right-originating illumination.

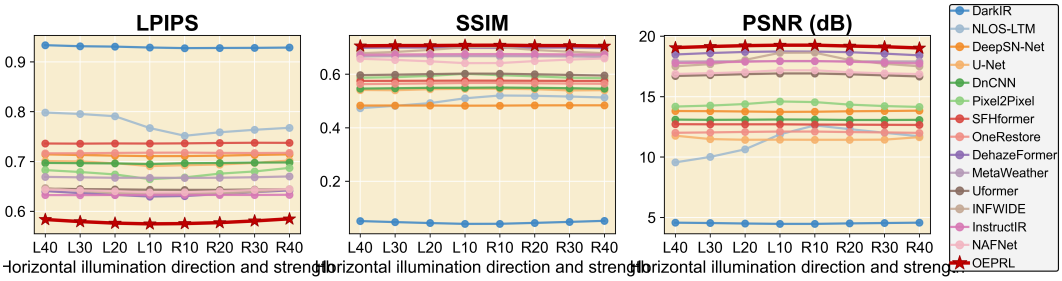

Figure A33: Figure trends under horizontal directional-light perturbations. The curves report LPIPS, SSIM, and PSNR across the conditions in Table A21. Markers denote the evaluated settings.

The left- and right-originating Figure curves preserve OEPRL's leading position across the horizontal sweep. Reading both directions together connects the reconstruction advantage to several spatial distributions of added illumination. The following Lock comparison checks this result for natural content under the corresponding horizontal interference.

Table A22: Lock point estimates under horizontal directional-light perturbations. Best and second-best values are highlighted in red and blue, respectively. The corresponding trend is shown in Figure A34.

Method	L40			L30			L20			L10			R10			R20			R30			R40		
	LPIPS↓	SSIM↑	PSNR (dB)↑	LPIPS↓	SSIM↑	PSNR (dB)↑	LPIPS↓	SSIM↑	PSNR (dB)↑	LPIPS↓	SSIM↑	PSNR (dB)↑	LPIPS↓	SSIM↑	PSNR (dB)↑	LPIPS↓	SSIM↑	PSNR (dB)↑	LPIPS↓	SSIM↑	PSNR (dB)↑	LPIPS↓	SSIM↑	PSNR (dB)↑
Passive Non-Line-of-Sight Reconstruction																								
NLOS-LTM	0.7921	0.3531	8.97	0.7894	0.3501	9.57	0.7826	0.2931	9.59	0.7946	0.3028	9.40	0.7905	0.2637	9.39	0.7984	0.3827	9.20	0.8020	0.4302	9.27	0.8014	0.4340	9.24
All-in-One and Universal Image Restoration																								
InstructIR	**0.7093**	0.5372	14.00	**0.6797**	**0.5597**	15.19	**0.6649**	**0.5758**	**15.93**	**0.6543**	**0.5874**	**16.31**	**0.6565**	**0.5821**	**16.23**	**0.6683**	**0.5705**	**15.80**	**0.6817**	**0.5553**	15.08	**0.7092**	0.5275	13.72
OneRestore	0.7283	0.5207	12.12	0.7269	0.5211	12.13	0.7261	0.5216	12.14	0.7248	0.5220	12.15	0.7250	0.5219	12.14	0.7260	0.5214	12.13	0.7269	0.5207	12.12	0.7280	0.5202	12.10
General-Purpose Image Restoration																								
SFHformer	0.7513	0.4927	11.81	0.7491	0.4971	11.95	0.7470	0.5018	12.11	0.7453	0.5059	12.26	0.7455	0.5078	12.38	0.7482	0.5049	12.32	0.7507	0.5015	12.23	0.7529	0.4978	12.12
Uformer	0.7159	**0.5457**	14.11	0.7044	0.5526	14.49	0.6938	0.5587	14.80	0.6837	0.5633	15.02	0.6840	0.5629	14.99	0.6946	0.5583	14.78	0.7056	0.5518	14.43	0.7174	**0.5446**	14.03
NAFNet	0.7270	0.5275	13.37	0.7082	0.5396	14.12	0.6897	0.5499	14.70	0.6747	0.5577	15.08	0.6745	0.5577	15.08	0.6899	0.5494	14.71	0.7076	0.5391	14.12	0.7270	0.5268	13.35
DeepSN-Net	0.7935	0.4118	12.11	0.7880	0.4177	12.34	0.7828	0.4218	12.55	0.7769	0.4234	12.70	0.7761	0.4230	12.73	0.7819	0.4208	12.63	0.7868	0.4160	12.43	0.7929	0.4090	12.15
DnCNN	0.7265	0.4767	11.81	0.7292	0.4775	11.79	0.7272	0.4779	11.76	0.7237	0.4780	11.73	0.7242	0.4778	11.73	0.7278	0.4778	11.76	0.7310	0.4763	11.79	0.7280	0.4756	11.80
U-Net	0.7941	0.4716	11.73	0.7987	0.4704	11.68	0.7973	0.4727	11.67	0.7829	0.4815	11.95	0.7802	0.4819	11.93	0.7942	0.4722	11.68	0.7938	0.4711	11.69	0.7921	0.4730	11.76
Related Degradations and Domains																								
INFWIDE	0.7393	0.5044	12.08	0.7397	0.5062	12.21	0.7383	0.5070	12.33	0.7358	0.5070	12.43	0.7362	0.5109	12.50	0.7385	0.5102	12.42	0.7406	0.5096	12.28	0.7396	0.5063	12.09
MetaWeather	0.7269	0.5122	**15.43**	0.7255	0.5138	**15.49**	0.7236	0.5147	15.54	0.7209	0.5141	15.57	0.7149	0.5292	**15.79**	0.7170	0.5284	15.77	0.7205	0.5234	**15.67**	0.7239	0.5233	**15.64**
Pixel2Pixel	0.7804	0.5145	12.15	0.7730	0.5151	12.18	0.7639	0.5158	12.22	0.7502	0.5164	12.26	0.7496	0.5165	12.27	0.7664	0.5157	12.22	0.7737	0.5150	12.18	0.7828	0.5143	12.14
DehazeFormer	0.7119	0.5130	13.77	0.6936	0.5278	14.50	0.6813	0.5377	14.86	0.6734	0.5421	14.92	0.6737	0.5430	14.93	0.6813	0.5393	14.87	0.6936	0.5298	14.52	0.7116	0.5147	13.79
DarkIR	0.8158	0.1070	8.83	0.8132	0.1040	8.80	0.8110	0.1004	8.77	0.8087	0.0963	8.75	0.8080	0.0962	8.75	0.8098	0.1004	8.78	0.8115	0.1041	8.80	0.8136	0.1075	8.83
OEPRL	**0.7022**	**0.5571**	**15.54**	**0.6729**	**0.5789**	**15.63**	**0.6466**	**0.5989**	**16.11**	**0.6313**	**0.6114**	**16.53**	**0.6353**	**0.6080**	**16.43**	**0.6509**	**0.5942**	**15.96**	**0.6749**	**0.5752**	**15.79**	**0.7021**	**0.5560**	**15.74**

OEPRL also remains first throughout the Lock sweep.

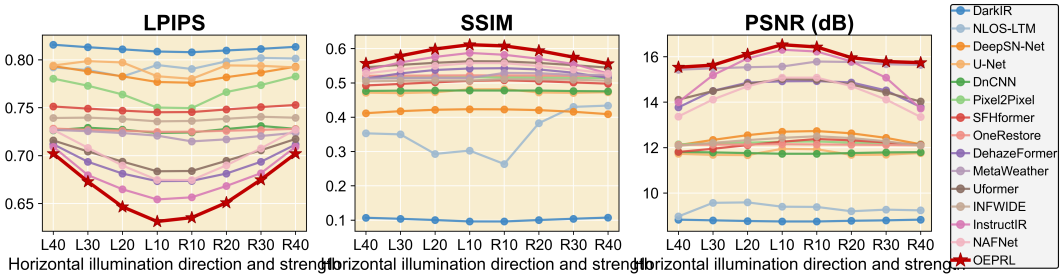

Figure A34: Lock trends under horizontal directional-light perturbations. The curves report LPIPS, SSIM, and PSNR across the conditions in Table A22. Markers denote the evaluated settings.

The Lock curves show a consistent lead for OEPRL as interference arrives from either side. At L40 and R40, PSNR is 15.54 and 15.74 dB, respectively, while SSIM remains above 0.55 at both endpoints. The accompanying Figure experiment retains a narrow SSIM range across the same directional sweep. These complementary content cases relate the numerical comparison to two forms of recoverable organization: natural foreground–background structure and regular graphical regions within the screen.

The added illumination changes the wall background, while OEPRL retains the colored chart regions and their horizontal organization within the hidden interface (Figure A35). Together with Figure A32, this shows that useful screen organization remains recoverable across different spatial distributions of ambient light.



Figure A35: A Figure example under left- and right-originating ambient-light perturbations. Rows show the reference followed by the four strengths for each direction.

C.13 Wall Roughness

Wall roughness changes how strongly the relay surface spreads local screen variation. This group tests the core global–local premise of RCER: broad color and luminance information remains a recovery cue while the strength and organization of residual structure evolve with surface scattering.

Table A23: Figure point estimates under wall roughness. Best and second-best values are highlighted in red and blue, respectively. The corresponding trend is shown in Figure A36.

Method	10			20			30			40		
	LPIPS↓	SSIM↑	PSNR (dB)↑	LPIPS↓	SSIM↑	PSNR (dB)↑	LPIPS↓	SSIM↑	PSNR (dB)↑	LPIPS↓	SSIM↑	PSNR (dB)↑
Passive Non-Line-of-Sight Reconstruction												
NLOS-LTM	0.7402	0.5271	13.19	0.7537	0.5187	12.48	0.7686	0.5110	11.77	0.7742	0.5060	11.43
All-in-One and Universal Image Restoration												
InstructIR	0.6357	0.6755	18.00	0.6437	0.6753	18.00	0.6515	0.6750	18.00	0.6611	0.6745	18.00
OneRestore	0.7233	0.5685	12.14	0.7368	0.5682	12.14	0.7476	0.5677	12.13	0.7616	0.5670	12.12
General-Purpose Image Restoration												
SFHformer	0.7424	0.5766	12.70	0.7594	0.5765	12.70	0.7724	0.5763	12.70	0.7862	0.5759	12.70
Uformer	0.6461	0.6039	16.99	0.6579	0.6035	16.97	0.6683	0.6031	16.95	0.6827	0.6024	16.94
NAFNet	0.6406	0.6361	17.36	0.6533	0.6354	17.35	0.6646	0.6346	17.35	0.6783	0.6333	17.34
DeepSN-Net	0.7146	0.4815	13.70	0.7270	0.4815	13.70	0.7366	0.4811	13.70	0.7476	0.4804	13.70
DnCNN	0.7154	0.5372	13.26	0.7262	0.5338	13.26	0.7332	0.5284	13.26	0.7440	0.5183	13.26
U-Net	0.6975	0.5459	11.44	0.7096	0.5436	11.50	0.7160	0.5405	11.52	0.7239	0.5295	11.53
Related Degradations and Domains												
INFWIDE	0.6397	**0.7037**	**18.76**	0.6609	0.6824	17.72	0.6728	0.6706	17.23	0.6807	0.6638	17.02
MetaWeather	0.6678	0.6677	17.93	0.6687	0.6676	17.93	0.6701	0.6672	17.93	0.6720	0.6668	17.93
Pixel2Pixel	0.7012	0.5618	13.67	0.7241	0.5304	13.77	0.7265	0.5477	13.79	0.7464	0.5205	12.79
DehazeFormer	**0.6307**	0.6947	18.70	**0.6387**	**0.6884**	**18.55**	**0.6456**	**0.6834**	**18.43**	**0.6546**	**0.6765**	**18.29**
DarkIR	0.9291	0.0383	4.44	0.9336	0.0390	4.44	0.9378	0.0396	4.45	0.9432	0.0407	4.45
OEPRL	**0.5800**	**0.7111**	**19.18**	**0.6030**	**0.6962**	**18.72**	**0.6219**	**0.6913**	**18.54**	**0.6425**	**0.6846**	**18.40**

The surface experiments test the wall itself, whose scattering response shapes the screen light available for reconstruction. Across all wall-roughness settings, OEPRL provides the best perceptual, structural, and pixel-level reconstruction on Figure. As the wall response changes, OEPRL retains its lead across the roughness sweep. RCER supplies the reconstruction with both broad color and luminance cues and positioned local variation, allowing the evidence pathway to draw on complementary information in the altered wall response.

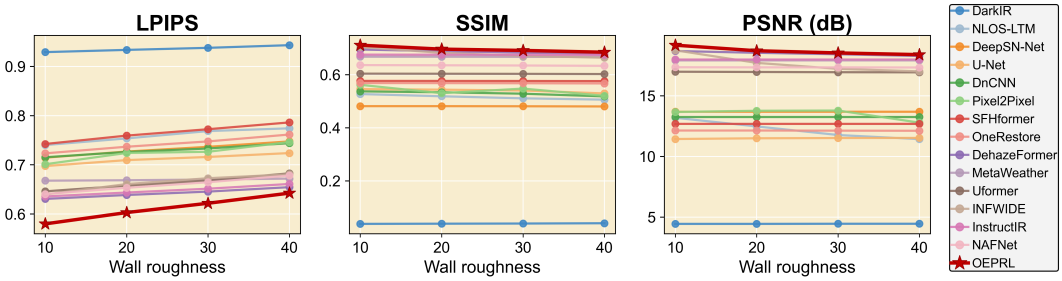

Figure A36: Figure trends under varying wall roughness. The curves report LPIPS, SSIM, and PSNR across the conditions in Table A23. Markers denote the evaluated settings.

From the first to the last roughness setting, Figure LPIPS changes from 0.5800 to 0.6425 and SSIM from 0.7111 to 0.6846, while PSNR changes from 19.18 to 18.40 dB. OEPRL leads at each setting. These complementary measures describe how perceptual appearance and regional structure vary with the altered wall response.

Table A24: Lock point estimates under wall roughness. Best and second-best values are highlighted in red and blue, respectively. The corresponding trend is shown in Figure A37.

Method	10			20			30			40		
	LPIPS↓	SSIM↑	PSNR (dB)↑	LPIPS↓	SSIM↑	PSNR (dB)↑	LPIPS↓	SSIM↑	PSNR (dB)↑	LPIPS↓	SSIM↑	PSNR (dB)↑
Passive Non-Line-of-Sight Reconstruction												
NLOS-LTM	0.7773	0.3346	10.07	0.7830	0.2925	9.65	0.7840	0.2890	9.61	0.7843	0.2906	9.61
All-in-One and Universal Image Restoration												
InstructIR	**0.6622**	**0.5808**	**16.35**	**0.6861**	**0.5627**	**15.91**	0.7065	0.5542	**15.68**	0.7322	0.5399	**15.32**
OneRestore	0.7264	0.5222	12.15	0.7358	0.5219	12.14	0.7435	0.5214	12.13	0.7537	0.5207	12.13
General-Purpose Image Restoration												
SFHformer	0.7467	0.5096	12.39	0.7577	0.5091	12.38	0.7668	0.5084	12.37	0.7772	0.5073	12.35
Uformer	0.6887	0.5637	15.06	0.7138	0.5577	14.98	0.7266	0.5518	14.89	0.7421	0.5427	14.74
NAFNet	0.6720	0.5619	15.18	0.6902	0.5599	15.14	0.7032	**0.5577**	15.09	0.7201	**0.5544**	15.00
DeepSN-Net	0.7818	0.4231	12.76	0.7982	0.4231	12.75	0.8069	0.4223	12.73	0.8168	0.4207	12.70
DnCNN	0.7390	0.4754	11.71	0.7379	0.4741	11.68	0.7442	0.4704	11.67	0.7479	0.4584	11.65
U-Net	0.7769	0.4831	12.08	0.8016	0.4712	12.02	0.8005	0.4670	12.06	0.8006	0.4617	12.03
Related Degradations and Domains												
INFWIDE	0.7444	0.5096	12.52	0.7487	0.5043	12.51	0.7558	0.5022	12.50	0.7628	0.5004	12.47
MetaWeather	0.7164	0.5193	15.64	0.7188	0.5112	15.52	0.7226	0.5054	15.39	0.7275	0.4983	15.25
Pixel2Pixel	0.7494	0.5164	12.30	0.7754	0.5138	12.26	0.7876	0.5123	12.23	0.8029	0.5098	12.20
DehazeFormer	0.6762	0.5380	14.83	0.6883	0.5384	14.89	**0.6981**	0.5362	14.93	**0.7129**	0.5302	14.92
DarkIR	0.8078	0.0930	8.73	0.8106	0.0942	8.73	0.8132	0.0952	8.74	0.8178	0.0964	8.74
OEPRL	**0.6391**	**0.6087**	**16.89**	**0.6644**	**0.5954**	**16.47**	**0.6911**	**0.5802**	**16.04**	**0.7057**	**0.5655**	**15.44**

The same cross-method advantage holds on Lock at every roughness setting. The benefit of the evidence-to-reconstruction pathway therefore extends across both surface variation and content type.

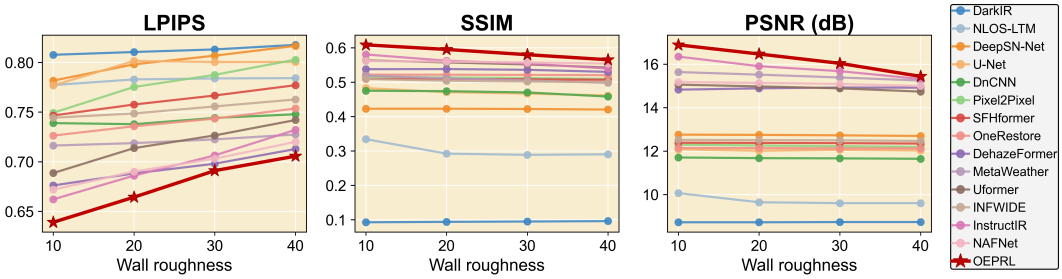

Figure A37: Lock trends under varying wall roughness. The curves report LPIPS, SSIM, and PSNR across the conditions in Table A24. Markers denote the evaluated settings.

The distinguishable graphical regions in Figure A38 show the resulting recovery of screen layout and color organization.

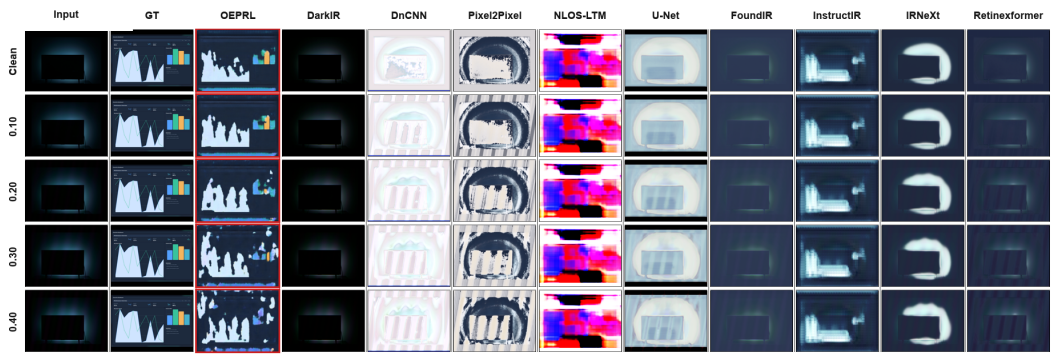

Figure A38: A Figure example under four wall-roughness settings, shown after the reference observation.

C.14 Wall Reflectance

Wall reflectance controls the radiometric strength of the screen signal that reaches the camera. We examine whether changes in wall-response strength still leave useful optical evidence for recovering the screen's regional organization.

Table A25: Figure point estimates under wall reflectance. Best and second-best values are highlighted in red and blue, respectively. The corresponding trend is shown in Figure A39.

Method	10			20			30			40		
	LPIPS↓	SSIM↑	PSNR (dB)↑	LPIPS↓	SSIM↑	PSNR (dB)↑	LPIPS↓	SSIM↑	PSNR (dB)↑	LPIPS↓	SSIM↑	PSNR (dB)↑
Passive Non-Line-of-Sight Reconstruction												
NLOS-LTM	0.7381	0.5291	13.34	0.7653	0.5135	12.01	0.7612	0.5154	12.16	0.7554	0.5178	12.45
All-in-One and Universal Image Restoration												
InstructIR	0.6334	0.6753	18.00	0.6333	0.6757	18.00	0.6333	0.6753	17.99	**0.6332**	0.6748	17.99
OneRestore	0.7181	0.5684	12.14	0.7183	0.5684	12.13	0.7185	0.5682	12.13	0.7190	0.5682	12.12
General-Purpose Image Restoration												
SFHformer	0.7363	0.5765	12.70	0.7369	0.5768	12.70	0.7370	0.5766	12.70	0.7372	0.5764	12.69
Uformer	0.6427	0.6036	16.96	0.6434	0.6033	16.94	0.6436	0.6026	16.92	0.6437	0.6020	16.89
NAFNet	0.6367	0.6367	17.33	0.6374	0.6378	17.30	0.6375	0.6380	17.28	0.6377	0.6381	17.26
DeepSN-Net	0.7105	0.4811	13.70	0.7112	0.4839	13.73	0.7116	0.4834	13.73	0.7123	0.4828	13.72
DnCNN	0.6871	0.5518	13.39	0.6975	0.5507	12.96	0.6975	0.5503	12.96	0.6974	0.5497	12.96
U-Net	0.6913	0.5459	11.42	0.6916	0.5466	11.44	0.6926	0.5463	11.43	0.6937	0.5457	11.43
Related Degradations and Domains												
INFWIDE	0.6345	**0.7049**	**18.88**	0.6384	**0.7011**	18.62	0.6391	**0.7008**	**18.60**	0.6400	**0.7002**	**18.53**
MetaWeather	0.6671	0.6675	17.93	0.6671	0.6679	17.93	0.6673	0.6678	17.93	0.6676	0.6674	17.92
Pixel2Pixel	0.6577	0.5926	14.79	0.6717	0.6004	14.59	0.6720	0.6000	14.60	0.6726	0.5991	14.61
DehazeFormer	**0.6288**	0.6961	18.72	**0.6313**	0.6960	**18.65**	**0.6327**	0.6956	**18.60**	0.6341	0.6945	18.52
DarkIR	0.9273	0.0384	4.45	0.9296	0.0399	4.45	0.9296	0.0403	4.46	0.9298	0.0406	4.46
OEPRL	**0.5759**	**0.7123**	**19.26**	**0.5777**	**0.7085**	**19.24**	**0.5811**	**0.7083**	**19.12**	**0.5847**	**0.7077**	**19.00**

Reflectance varies the strength of the wall response, complementing the roughness test of how that response is spread. OEPRL leads every Figure condition, with PSNR between 19.00 and 19.26 dB and SSIM between 0.7077 and 0.7123. The graphical arrangement remains recoverable across the corresponding change in wall-response strength.

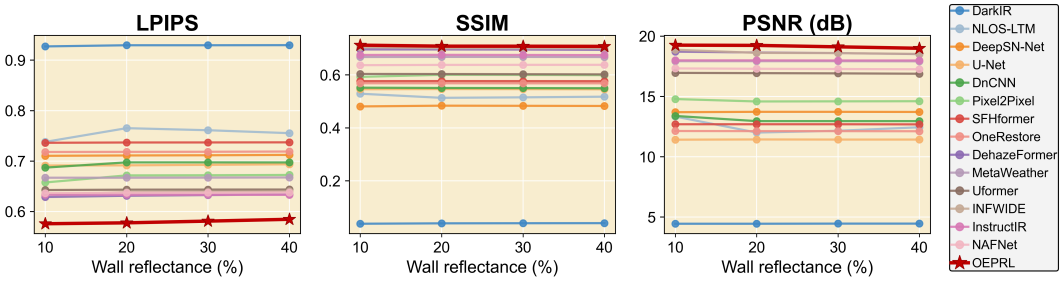

Figure A39: Figure trends under varying wall reflectance. The curves report LPIPS, SSIM, and PSNR across the conditions in Table A25. Markers denote the evaluated settings.

Perceptual agreement also varies within a narrow range: Figure LPIPS is 0.5759–0.5847 across the four reflectance settings. At the final setting, OEPRL reaches 0.5847, compared with 0.6377 for NAFNet and 0.6437 for Uformer. This complements the structural and pixel-level comparison by tracing perceptual differences in the recovered graphical content.

Table A26: Lock point estimates under wall reflectance. Best and second-best values are highlighted in red and blue, respectively. The corresponding trend is shown in Figure A40.

Method	10			20			30			40		
	LPIPS↓	SSIM↑	PSNR (dB)↑	LPIPS↓	SSIM↑	PSNR (dB)↑	LPIPS↓	SSIM↑	PSNR (dB)↑	LPIPS↓	SSIM↑	PSNR (dB)↑
Passive Non-Line-of-Sight Reconstruction												
NLOS-LTM	0.7768	0.4056	10.90	0.7884	0.2608	9.37	0.7880	0.2628	9.39	0.7877	0.2641	9.40
All-in-One and Universal Image Restoration												
InstructIR	**0.6493**	**0.5889**	**16.46**	**0.6528**	**0.5879**	**16.36**	**0.6537**	**0.5875**	**16.29**	**0.6558**	**0.5855**	**16.19**
OneRestore	0.7239	0.5222	12.15	0.7251	0.5223	12.14	0.7249	0.5221	12.14	0.7248	0.5218	12.14
General-Purpose Image Restoration												
SFHformer	0.7438	0.5094	12.39	0.7451	0.5084	12.34	0.7453	0.5077	12.33	0.7457	0.5069	12.32
Uformer	0.6783	0.5650	15.08	0.6829	0.5637	15.05	0.6842	0.5628	15.02	0.6858	0.5614	14.97
NAFNet	0.6672	0.5623	15.19	0.6739	0.5592	15.10	0.6746	0.5585	15.09	0.6754	0.5578	15.08
DeepSN-Net	0.7745	0.4225	12.76	0.7734	0.4258	12.75	0.7740	0.4252	12.75	0.7751	0.4244	12.74
DnCNN	0.7246	0.4785	11.75	0.7207	0.4785	11.71	0.7213	0.4782	11.71	0.7217	0.4777	11.72
U-Net	0.7637	0.4877	12.12	0.7820	0.4814	11.96	0.7816	0.4811	11.97	0.7812	0.4808	11.98
Related Degradations and Domains												
INFWIDE	0.7358	0.5115	12.52	0.7345	0.5113	12.49	0.7346	0.5111	12.49	0.7348	0.5108	12.47
MetaWeather	0.7150	0.5251	15.71	0.7164	0.5236	15.64	0.7175	0.5243	15.61	0.7186	0.5230	15.56
Pixel2Pixel	0.7336	0.5175	12.32	0.7489	0.5168	12.25	0.7493	0.5167	12.25	0.7499	0.5165	12.26
DehazeFormer	0.6723	0.5372	14.82	0.6719	0.5428	14.90	0.6725	0.5426	14.91	0.6733	0.5422	14.92
DarkIR	0.8070	0.0928	8.73	0.8093	0.0955	8.74	0.8093	0.0958	8.74	0.8094	0.0961	8.75
OEPRL	**0.6269**	**0.6157**	**17.02**	**0.6314**	**0.6136**	**16.91**	**0.6334**	**0.6100**	**16.75**	**0.6364**	**0.6066**	**16.55**

OEPRL also retains the best reconstruction throughout the Lock reflectance sweep. Combined with roughness, this shows that the relative advantage extends across two different aspects of the relay surface.

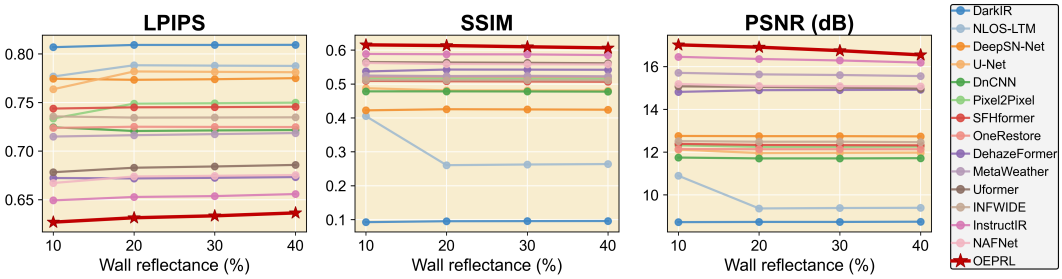

Figure A40: Lock trends under varying wall reflectance. The curves report LPIPS, SSIM, and PSNR across the conditions in Table A26. Markers denote the evaluated settings.

OEPRL preserves distinct colored chart blocks within the bright page as the wall response changes. Several comparison methods recover a largely uniform page region, while OEPRL retains more of the target's regional color organization.

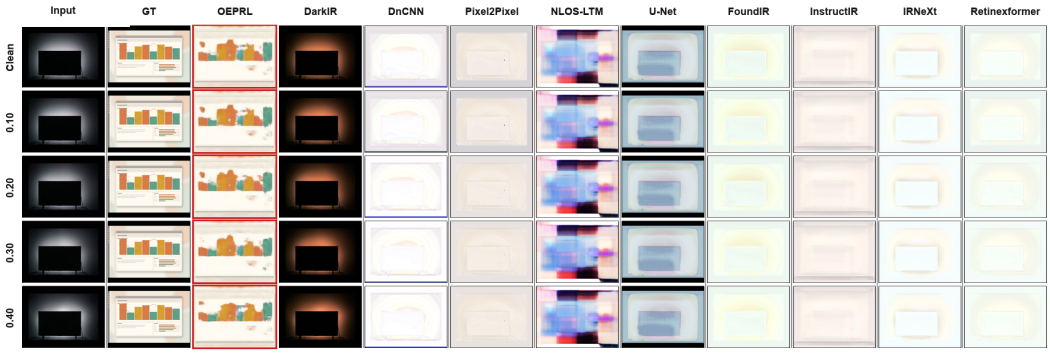

Figure A41: A Figure example under four wall-reflectance settings, shown after the reference observation.

C.15 MOTION BLUR

Motion blur selectively attenuates local variation in the wall observation while retaining much of its broad luminance field. The experiments therefore test whether the surviving wall pattern continues to support coarse screen organization as sharper local variation is smoothed.

Table A27: Figure point estimates under motion blur. Best and second-best values are highlighted in red and blue, respectively. The corresponding trend is shown in Figure A42.

Method	k=3			k=5			k=7			k=9			k=11		
	LPIPS↓	SSIM↑	PSNR (dB)↑	LPIPS↓	SSIM↑	PSNR (dB)↑	LPIPS↓	SSIM↑	PSNR (dB)↑	LPIPS↓	SSIM↑	PSNR (dB)↑	LPIPS↓	SSIM↑	PSNR (dB)↑
Passive Non-Line-of-Sight Reconstruction															
NLOS-LTM	0.7394	0.5281	13.29	0.7399	0.5278	13.29	0.7404	0.5274	13.27	0.7413	0.5269	13.24	0.7422	0.5261	13.20
All-in-One and Universal Image Restoration															
InstructIR	0.6360	0.6792	18.00	0.6343	0.6809	18.00	0.6364	0.6831	18.00	0.6380	0.6855	17.99	**0.6376**	0.6856	17.99
OneRestore	0.7223	0.5709	12.16	0.7257	0.5724	12.17	0.7285	0.5735	12.18	0.7300	0.5746	12.19	0.7313	0.5757	12.20
General-Purpose Image Restoration															
SFHformer	0.7396	0.5785	12.70	0.7401	0.5793	12.70	0.7411	0.5800	12.70	0.7413	0.5808	12.70	0.7422	0.5815	12.69
Uformer	0.6468	0.6078	17.02	0.6479	0.6106	17.03	0.6515	0.6134	17.04	0.6552	0.6168	17.06	0.6596	0.6193	17.07
NAFNet	0.6390	0.6402	17.36	0.6417	0.6434	17.36	0.6453	0.6460	17.36	0.6501	0.6487	17.36	0.6548	0.6505	17.37
DeepSN-Net	0.7105	0.4852	13.70	0.7105	0.4867	13.70	0.7117	0.4883	13.71	0.7099	0.4909	13.71	0.7088	0.4926	13.71
DnCNN	0.6873	0.5539	13.39	0.6844	0.5532	13.38	0.6834	0.5519	13.38	0.6812	0.5497	13.38	0.6825	0.5474	13.37
U-Net	0.6943	0.5461	11.43	0.6950	0.5465	11.44	0.6957	0.5465	11.45	0.6953	0.5457	11.46	0.6963	0.5451	11.47
Related Degradations and Domains															
INFWIDE	0.6384	**0.7020**	18.61	0.6444	**0.6990**	18.34	0.6492	**0.6964**	18.08	0.6539	**0.6949**	17.88	0.6625	0.6935	17.66
MetaWeather	0.6674	0.6678	17.93	0.6675	0.6680	17.92	0.6674	0.6683	17.92	0.6667	0.6685	17.91	0.6664	0.6684	17.90
Pixel2Pixel	0.6567	0.5934	14.85	0.6605	0.5945	14.85	0.6624	0.5967	14.86	0.6646	0.5985	14.87	0.6664	0.5986	14.87
DehazeFormer	**0.6290**	0.6953	**18.69**	**0.6311**	0.6953	**18.65**	**0.6340**	0.6950	**18.60**	**0.6366**	0.6948	**18.57**	0.6398	**0.6945**	**18.53**
DarkIR	0.9347	0.0382	4.44	0.9399	0.0383	4.44	0.9441	0.0384	4.44	0.9495	0.0385	4.44	0.9530	0.0386	4.44
OEPRL	**0.5808**	**0.7055**	**19.18**	**0.5810**	**0.7004**	**19.17**	**0.5814**	**0.7005**	**19.16**	**0.5815**	**0.6999**	**19.12**	**0.5834**	**0.6995**	**19.09**

INFWIDE combines image- and feature-space Wiener deconvolution for low-light deblurring Zhang et al. (2023), and its Figure PSNR in our blur test decreases from 18.61 to 17.66 dB as k increases from 3 to 11 (Table A27). With RCER's broad color and luminance cues from the wall and positioned local evidence, OEPRL retains distinguishable chart regions while Figure PSNR decreases from 19.18 to 19.09 dB over the same sweep, a change of only 0.09 dB (Figure A44).

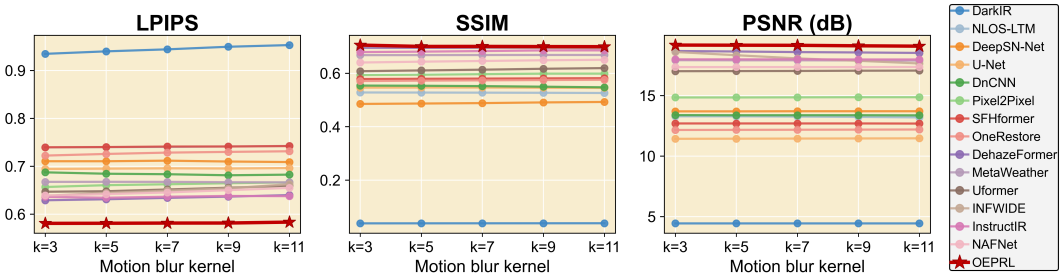

Figure A42: Figure trends under varying motion blur. The curves report LPIPS, SSIM, and PSNR across the conditions in Table A27. Markers denote the evaluated settings.

The perceptual and structural comparisons support the small PSNR change. At the largest tested kernel, OEPRL reaches 0.5834 LPIPS and 0.6995 SSIM on Figure, compared with 0.6625 and 0.6935 for INFWIDE. Its PSNR at this setting is 19.09 dB, against 17.66 dB for INFWIDE. Thus, the preserved graphical regions accompany an advantage in both perceptual distance and pixel-level agreement. RCER's representation retains broad wall color and luminance together with local residual information, while the decoder receives global and regional evidence corrections. These are the complementary information paths through which OEPRL processes the blurred observation. The next comparison follows the same capture disturbance on Lock, whose natural color transitions and salient foreground provide a different content structure.

Across the kernel sweep, OEPRL's Figure LPIPS changes from 0.5808 at $k = 3$ to 0.5834 at $k = 11$, while SSIM changes from 0.7055 to 0.6995. The LPIPS increase of 0.0026 and SSIM decrease of 0.0060 provide complementary measures of the endpoint change. Together with the reported PSNR values, they describe the variation across the evaluated blur conditions.

Table A28: Lock point estimates under motion blur. Best and second-best values are highlighted in red and blue, respectively. The corresponding trend is shown in Figure A43.

Method	k=3			k=5			k=7			k=9			k=11		
	LPIPS↓	SSIM↑	PSNR (dB)↑	LPIPS↓	SSIM↑	PSNR (dB)↑	LPIPS↓	SSIM↑	PSNR (dB)↑	LPIPS↓	SSIM↑	PSNR (dB)↑	LPIPS↓	SSIM↑	PSNR (dB)↑
Passive Non-Line-of-Sight Reconstruction															
NLOS-LTM	0.7775	0.4034	10.86	0.7777	0.4012	10.82	0.7778	0.3988	10.78	0.7779	0.3955	10.74	0.7780	0.3929	10.71
All-in-One and Universal Image Restoration															
InstructIR	**0.6502**	**0.5909**	**16.49**	**0.6506**	**0.5921**	**16.48**	**0.6512**	**0.5929**	**16.48**	**0.6509**	**0.5919**	**16.45**	**0.6509**	**0.5891**	**16.38**
OneRestore	0.7300	0.5234	12.15	0.7342	0.5240	12.15	0.7388	0.5246	12.15	0.7439	0.5252	12.16	0.7479	0.5256	12.16
General-Purpose Image Restoration															
SFHformer	0.7463	0.5108	12.40	0.7493	0.5119	12.40	0.7515	0.5130	12.40	0.7536	0.5146	12.40	0.7564	0.5162	12.39
Uformer	0.6788	0.5669	15.08	0.6790	0.5683	15.08	0.6790	0.5692	15.08	0.6788	0.5699	15.08	0.6776	0.5697	15.04
NAFNet	0.6675	0.5645	15.19	0.6676	0.5662	15.19	0.6680	0.5675	15.19	0.6676	0.5688	15.19	0.6676	0.5695	15.19
DeepSN-Net	0.7779	0.4240	12.76	0.7803	0.4250	12.76	0.7832	0.4258	12.76	0.7859	0.4267	12.76	0.7869	0.4275	12.76
DnCNN	0.7284	0.4797	11.75	0.7293	0.4807	11.76	0.7297	0.4815	11.76	0.7303	0.4826	11.76	0.7309	0.4833	11.76
U-Net	0.7691	0.4886	12.12	0.7725	0.4899	12.11	0.7747	0.4908	12.10	0.7762	0.4910	12.03	0.7784	0.4914	11.99
Related Degradations and Domains															
INFWIDE	0.8533	0.0696	8.44	0.8533	0.0696	8.44	0.8533	0.0696	8.44	0.8533	0.0696	8.44	0.8533	0.0696	8.44
MetaWeather	0.7172	0.5215	15.66	0.7187	0.5187	15.60	0.7200	0.5160	15.55	0.7210	0.5135	15.49	0.7226	0.5102	15.41
Pixel2Pixel	0.7344	0.5179	12.32	0.7353	0.5184	12.32	0.7375	0.5190	12.32	0.7371	0.5198	12.32	0.7409	0.5206	12.32
DehazeFormer	0.6722	0.5393	14.81	0.6723	0.5409	14.80	0.6727	0.5421	14.80	0.6720	0.5433	14.78	0.6713	0.5439	14.75
DarkIR	0.8093	0.0927	8.73	0.8111	0.0927	8.73	0.8127	0.0927	8.73	0.8154	0.0927	8.73	0.8172	0.0927	8.73
OEPRL	**0.6331**	**0.6090**	**16.97**	**0.6329**	**0.6102**	**16.97**	**0.6331**	**0.6108**	**16.96**	**0.6337**	**0.6079**	**16.76**	**0.6360**	**0.6025**	**16.53**

The reconstruction advantage also persists on Lock through the largest blur kernel (Table A28), extending the result from graphical layouts to natural screen content.

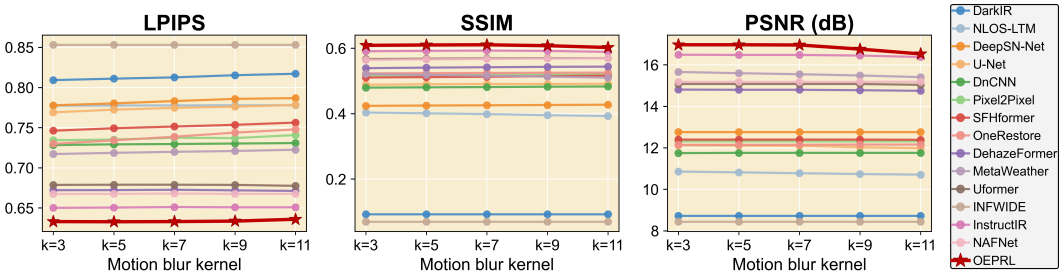

Figure A43: Lock trends under varying motion blur. The curves report LPIPS, SSIM, and PSNR across the conditions in Table A28. Markers denote the evaluated settings.

The Lock curves place the natural-content comparison alongside the Figure result: OEPRL remains ahead through the largest tested kernel. The qualitative Figure sequence below shows the corresponding graphical content. Distinct chart regions remain visible as the input is smoothed, giving the metric comparison a direct interpretation in terms of recovered screen organization.

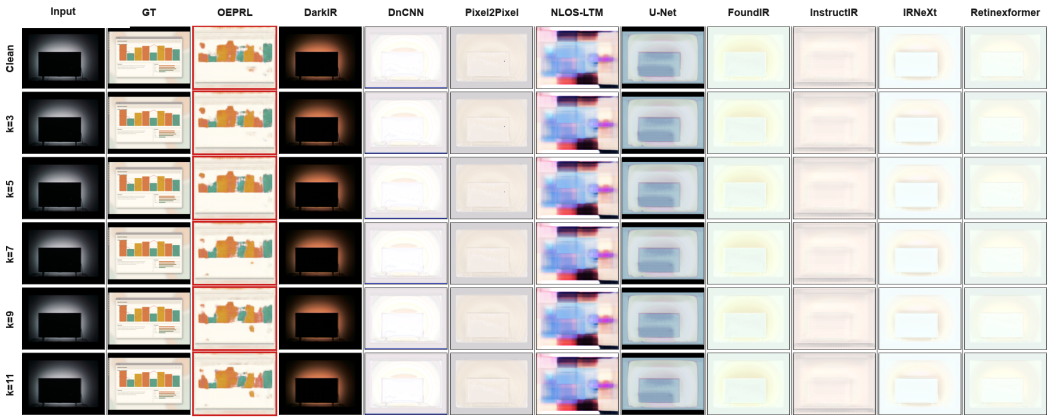

Figure A44: A Figure example under motion blur. Rows show the reference and kernel settings $k = 3, 5, 7, 9$, and 11.

C.16 Camera Shake

The preceding blur experiment smooths local wall variation; camera shake also disturbs its spatial placement. We now examine whether the main screen regions remain recoverable from this disturbed evidence.

Table A29: Figure point estimates under camera shake. Best and second-best values are highlighted in red and blue, respectively. The corresponding trend is shown in Figure A45.

Method	0.6 px			1.0 px			1.4 px			1.8 px			2.2 px		
	LPIPS↓	SSIM↑	PSNR (dB)↑	LPIPS↓	SSIM↑	PSNR (dB)↑	LPIPS↓	SSIM↑	PSNR (dB)↑	LPIPS↓	SSIM↑	PSNR (dB)↑	LPIPS↓	SSIM↑	PSNR (dB)↑
Passive Non-Line-of-Sight Reconstruction															
NLOS-LTM	0.7392	0.5279	13.27	0.7399	0.5272	13.24	0.7411	0.5262	13.19	0.7422	0.5256	13.16	0.7424	0.5250	13.13
All-in-One and Universal Image Restoration															
InstructIR	0.6382	0.6811	18.00	0.6387	0.6828	18.00	0.6390	0.6840	18.01	0.6385	0.6841	18.00	**0.6383**	0.6846	17.99
OneRestore	0.7203	0.5706	12.16	0.7232	0.5723	12.17	0.7252	0.5736	12.18	0.7265	0.5747	12.19	0.7279	0.5755	12.20
General-Purpose Image Restoration															
SFHformer	0.7386	0.5781	12.70	0.7408	0.5792	12.69	0.7427	0.5797	12.69	0.7444	0.5801	12.69	0.7455	0.5805	12.69
Uformer	0.6473	0.6081	17.02	0.6510	0.6113	17.04	0.6538	0.6135	17.06	0.6555	0.6156	17.07	0.6565	0.6167	17.08
NAFNet	0.6410	0.6406	17.37	0.6446	0.6439	17.38	0.6478	0.6463	17.39	0.6498	0.6485	17.39	0.6505	0.6497	17.39
DeepSN-Net	0.7121	0.4851	13.71	0.7118	0.4872	13.71	0.7133	0.4889	13.71	0.7149	0.4904	13.71	0.7156	0.4917	13.71
DnCNN	0.6869	0.5531	13.39	0.6859	0.5525	13.38	0.6848	0.5503	13.38	0.6841	0.5480	13.38	0.6839	0.5471	13.37
U-Net	0.6926	0.5458	11.44	0.6944	0.5455	11.45	0.6955	0.5457	11.47	0.6969	0.5455	11.48	0.6974	0.5459	11.48
Related Degradations and Domains															
INFWIDE	0.6403	**0.7015**	18.57	0.6501	**0.6979**	18.13	0.6591	**0.6961**	17.98	0.6627	0.6955	17.80	0.6645	0.6953	17.82
MetaWeather	0.6677	0.6678	17.92	0.6672	0.6678	17.92	0.6675	0.6674	17.90	0.6676	0.6672	17.88	0.6682	0.6666	17.86
Pixel2Pixel	0.6582	0.5939	14.86	0.6610	0.5934	14.85	0.6631	0.5948	14.86	0.6649	0.5960	14.86	0.6667	0.5975	14.86
DehazeFormer	**0.6307**	0.6952	**18.67**	**0.6325**	0.6962	**18.70**	**0.6355**	0.6952	**18.59**	**0.6383**	**0.6965**	**18.60**	0.6397	**0.6965**	**18.58**
DarkIR	0.9337	0.0382	4.44	0.9403	0.0383	4.44	0.9440	0.0383	4.44	0.9467	0.0384	4.44	0.9474	0.0386	4.44
OEPRL	**0.5805**	**0.7050**	**19.14**	**0.5814**	**0.6994**	**19.14**	**0.5835**	**0.6993**	**19.07**	**0.5859**	**0.6992**	**19.04**	**0.5892**	**0.6974**	**19.00**

The screen's principal graphical regions remain recoverable as shake disturbs the spatial organization of the measured wall pattern. OEPRL retains the best Figure reconstruction across all levels, with PSNR within 19.00–19.14 dB. The corresponding images preserve the main graphical regions despite the observation disturbance.

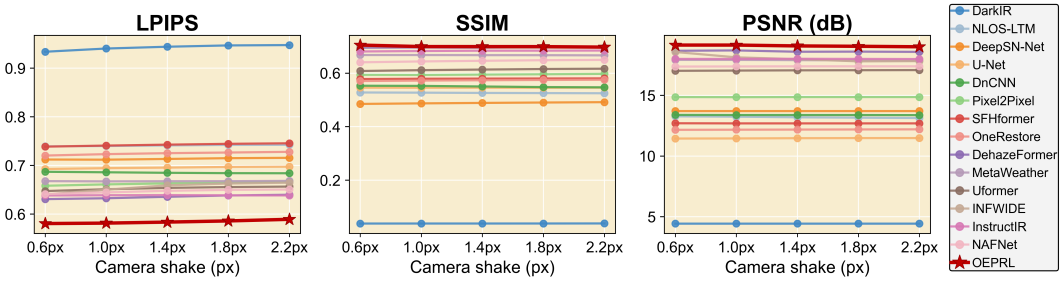

Figure A45: Figure trends under camera shake. The curves report LPIPS, SSIM, and PSNR across the conditions in Table A29. Markers denote the evaluated settings.

The perceptual comparison supports the preserved graphical regions at the largest shake level: OEPRL reaches 0.5892 LPIPS, compared with 0.6645 for INFWIDE. Its SSIM at this setting is 0.6974, against 0.6953 for INFWIDE. These two measures complement the PSNR comparison when assessing the reconstruction of spatially disturbed wall observations.

Table A30: Lock point estimates under camera shake. Best and second-best values are highlighted in red and blue, respectively. The corresponding trend is shown in Figure A46.

Method	0.6 px			1.0 px			1.4 px			1.8 px			2.2 px		
	LPIPS↓	SSIM↑	PSNR (dB)↑	LPIPS↓	SSIM↑	PSNR (dB)↑	LPIPS↓	SSIM↑	PSNR (dB)↑	LPIPS↓	SSIM↑	PSNR (dB)↑	LPIPS↓	SSIM↑	PSNR (dB)↑
Passive Non-Line-of-Sight Reconstruction															
NLOS-LTM	0.7770	0.4020	10.85	0.7772	0.3996	10.82	0.7772	0.3972	10.79	0.7777	0.3951	10.76	0.7778	0.3927	10.73
All-in-One and Universal Image Restoration															
InstructIR	**0.6514**	**0.5886**	**16.45**	**0.6565**	**0.5750**	**16.23**	**0.6597**	0.5663	**15.96**	**0.6599**	0.5651	**15.82**	**0.6646**	0.5548	15.48
OneRestore	0.7301	0.5232	12.15	0.7350	0.5240	12.15	0.7382	0.5245	12.16	0.7399	0.5248	12.16	0.7415	0.5250	12.16
General-Purpose Image Restoration															
SFHformer	0.7459	0.5110	12.40	0.7488	0.5124	12.40	0.7511	0.5135	12.40	0.7525	0.5142	12.40	0.7539	0.5149	12.40
Uformer	0.6792	0.5672	15.10	0.6786	0.5676	15.07	0.6788	**0.5675**	15.03	0.6787	0.5658	14.97	0.6785	0.5640	14.86
NAFNet	0.6678	0.5645	15.19	0.6680	0.5659	15.19	0.6681	0.5670	15.19	0.6680	**0.5677**	15.19	0.6687	**0.5685**	15.19
DeepSN-Net	0.7782	0.4240	12.76	0.7806	0.4250	12.75	0.7825	0.4258	12.75	0.7839	0.4266	12.75	0.7856	0.4274	12.74
DnCNN	0.7274	0.4800	11.75	0.7291	0.4812	11.75	0.7298	0.4820	11.75	0.7300	0.4825	11.75	0.7299	0.4831	11.76
U-Net	0.7681	0.4878	12.06	0.7712	0.4876	12.00	0.7731	0.4884	11.97	0.7741	0.4886	11.93	0.7745	0.4890	11.91
Related Degradations and Domains															
INFWIDE	0.8533	0.0696	8.44	0.8533	0.0696	8.44	0.8533	0.0696	8.44	0.8533	0.0696	8.44	0.8533	0.0696	8.44
MetaWeather	0.7160	0.5232	15.70	0.7167	0.5218	15.67	0.7177	0.5204	15.62	0.7184	0.5194	15.63	0.7190	0.5172	**15.57**
Pixel2Pixel	0.7348	0.5180	12.32	0.7370	0.5186	12.32	0.7387	0.5193	12.32	0.7401	0.5198	12.32	0.7416	0.5204	12.32
DehazeFormer	0.6718	0.5390	14.80	0.6708	0.5398	14.77	0.6706	0.5401	14.76	0.6707	0.5403	14.75	0.6709	0.5402	14.74
DarkIR	0.8095	0.0927	8.73	0.8119	0.0927	8.73	0.8136	0.0927	8.73	0.8148	0.0928	8.73	0.8160	0.0928	8.73
OEPRL	**0.6342**	**0.6054**	**16.84**	**0.6391**	**0.5966**	**16.51**	**0.6440**	**0.5805**	**16.07**	**0.6473**	**0.5809**	**15.88**	**0.6531**	**0.5720**	**15.69**

The same comparative advantage extends to natural lock-screen imagery. Across all shake levels, OEPRL remains first in perceptual, structural, and pixel-level agreement, extending the capture-disturbance result beyond regular graphical content.

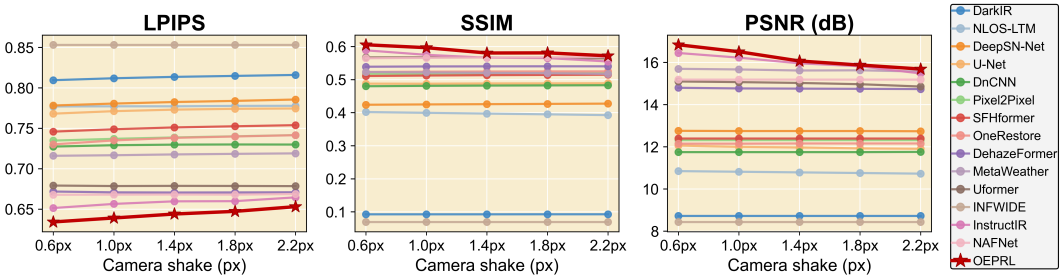

Figure A46: Lock trends under camera shake. The curves report LPIPS, SSIM, and PSNR across the conditions in Table A30. Markers denote the evaluated settings.

The main light graphical regions and the colored bars on the right remain recognizable across the shake levels. The example closes the capture-disturbance analysis with a visible result: useful screen organization persists in reconstructions from spatially disturbed wall observations.

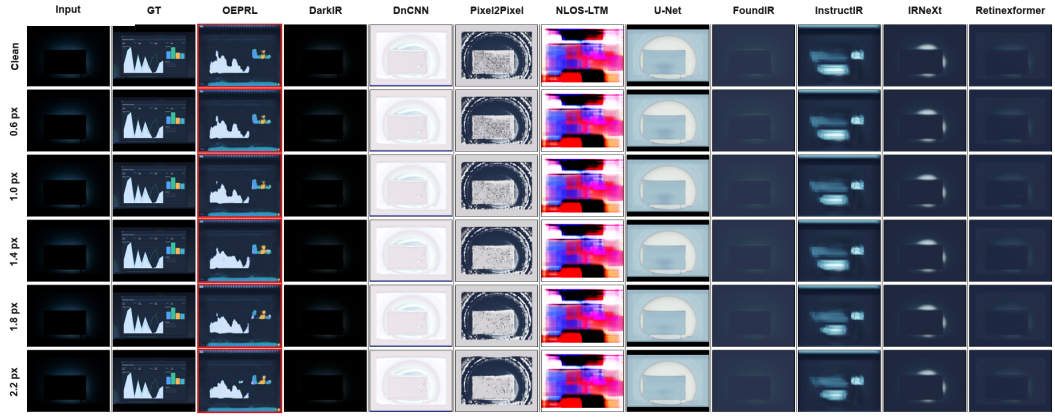

Figure A47: A Figure example under camera-shake perturbations. Rows show the reference and shake levels of 0.6, 1.0, 1.4, 1.8, and 2.2 px.

The numerical comparisons support the visible persistence of these regions. At the largest shake level, Figure PSNR is 19.00 dB for OEPRL, compared with 17.82 dB for INFWIDE and 17.39 dB for NAFNet. On Lock, OEPRL reaches 15.69 dB at the same level, compared with 15.19 dB for NAFNet. Its leading position therefore extends to both graphical and natural content at the end of the tested sweep.

The shake and blur experiments complement the earlier camera-position tests. The latter change where wall evidence is sampled in the observation; the capture disturbances alter the measured pattern from which the reconstruction is formed. Across these comparisons, the recovered color regions and principal layouts provide a common image-level result. OEPRL carries broad optical context into the latent features and passes positioned evidence into the global and regional decoder corrections. This evidence-to-reconstruction pathway connects the diverse observation changes to the same output task: recovering the organization of hidden-screen content from diffuse wall light. The remaining comparison examines how that advantage extends across lens configurations.

C.17 Lens Configuration

Lens configuration changes the camera's field of view and image formation. The two tables examine whether the reconstruction advantage persists when the wall evidence is presented through different optical mappings.

Table A31: Figure point estimates under camera lens. Best and second-best values are highlighted in red and blue, respectively.

Method	pinhole			telephoto			wide			strong-wide			ultrawide		
	LPIPS↓	SSIM↑	PSNR (dB)↑	LPIPS↓	SSIM↑	PSNR (dB)↑	LPIPS↓	SSIM↑	PSNR (dB)↑	LPIPS↓	SSIM↑	PSNR (dB)↑	LPIPS↓	SSIM↑	PSNR (dB)↑
Passive Non-Line-of-Sight Reconstruction															
NLOS-LTM	0.7389	0.5283	13.29	0.7364	0.5289	13.44	0.7402	0.5284	13.27	0.7457	0.5278	13.16	0.7483	0.5327	13.10
All-in-One and Universal Image Restoration															
InstructIR	0.6334	0.6756	18.00	**0.6437**	0.6653	17.60	**0.6294**	0.6650	18.03	**0.6303**	0.6600	**18.17**	**0.6351**	0.6468	**17.74**
OneRestore	0.7180	0.5688	12.14	0.7187	0.5663	12.10	0.7198	0.5693	12.18	0.7219	0.5717	12.21	0.7223	0.5753	12.21
General-Purpose Image Restoration															
SFHformer	0.7361	0.5767	12.70	0.7306	0.5695	12.68	0.7341	0.5711	12.70	0.7363	0.5697	12.68	0.7382	0.5743	12.66
Uformer	0.6425	0.6042	17.00	0.6493	0.6016	16.84	0.6404	0.6033	17.09	0.6388	0.6091	17.09	0.6445	0.6118	17.07
NAFNet	0.6365	0.6366	17.36	0.6464	0.6726	16.84	0.6324	0.6328	17.65	0.6384	0.6362	16.87	0.6680	0.6319	14.55
DeepSN-Net	0.7102	0.4815	13.70	0.7143	0.4733	13.63	0.7079	0.4758	13.64	0.7021	0.4744	13.50	0.6989	0.4759	13.21
DnCNN	0.6870	0.5521	13.39	0.7018	0.5546	13.20	0.6833	0.5501	13.44	0.6805	0.5514	13.53	0.6819	0.5502	13.56
U-Net	0.6908	0.5461	11.42	0.7074	0.5430	11.58	0.6965	0.5445	11.40	0.6981	0.5461	11.18	0.7033	0.5480	11.00
Related Degradations and Domains															
INFWIDE	0.6347	**0.7050**	**18.88**	0.6909	0.6808	17.11	0.6988	0.6771	17.00	0.7165	**0.6782**	17.16	0.7568	**0.6570**	15.52
MetaWeather	0.6674	0.6677	17.93	0.6891	0.6030	17.75	0.6668	0.6522	17.70	0.7431	0.5587	17.12	0.9239	0.3764	8.36
Pixel2Pixel	0.6559	0.5950	14.86	0.6705	0.6028	15.20	0.6570	0.5924	14.79	0.6570	0.5909	14.47	0.6661	0.5880	14.12
DehazeFormer	**0.6279**	0.6954	18.71	0.6666	**0.6912**	**17.81**	0.6583	**0.6879**	**18.34**	0.6698	0.6632	17.92	0.6792	0.6144	16.32
DarkIR	0.9275	0.0382	4.44	0.9373	0.0449	4.56	0.9252	0.0370	4.41	0.9235	0.0320	4.30	0.9282	0.0269	4.20
OEPRL	**0.5805**	**0.7085**	**19.17**	**0.6398**	**0.6947**	**17.93**	**0.6256**	**0.6914**	**18.46**	**0.6266**	**0.6817**	**18.29**	**0.6313**	**0.6605**	**17.86**

The lens comparison changes how the wall response is mapped into the image. OEPRL ranks first in every metric across all five configurations on Figure, extending its reconstruction advantage to different image-formation settings.

The Figure comparison includes pinhole, telephoto, wide, strong-wide, and ultrawide configurations. OEPRL's lead spans perceptual, structural, and pixel-level agreement within each configuration. For the ultrawide setting, it reaches 17.86 dB PSNR and 0.6313 LPIPS, compared with 17.07 dB and 0.6445 for Uformer. The Lock table then applies the same set of configuration labels to natural imagery, testing whether the cross-method advantage extends beyond graphical layouts.

Table A32: Lock point estimates under camera lens. Best and second-best values are highlighted in red and blue, respectively.

Method	pinhole			telephoto			wide			strong-wide			ultrawide		
	LPIPS↓	SSIM↑	PSNR (dB)↑	LPIPS↓	SSIM↑	PSNR (dB)↑	LPIPS↓	SSIM↑	PSNR (dB)↑	LPIPS↓	SSIM↑	PSNR (dB)↑	LPIPS↓	SSIM↑	PSNR (dB)↑
Passive Non-Line-of-Sight Reconstruction															
NLOS-LTM	0.7770	0.4052	10.89	0.7779	0.4085	11.02	0.7779	0.4047	10.85	0.7797	0.4057	10.70	0.7817	0.4087	10.60
All-in-One and Universal Image Restoration															
InstructIR	**0.6489**	**0.5892**	**16.49**	0.6764	0.5480	**15.03**	0.6758	0.5104	14.77	0.6960	0.4740	14.23	0.6922	**0.5580**	**14.73**
OneRestore	0.7240	0.5224	12.15	0.7278	0.5229	12.18	0.7247	0.5225	12.15	0.7221	0.5223	12.11	0.7194	0.5219	12.07
General-Purpose Image Restoration															
SFHformer	0.7437	0.5098	12.40	0.7477	0.5024	12.33	0.7430	0.5064	12.37	0.7392	0.5101	12.34	0.7378	0.5101	12.29
Uformer	0.6778	0.5653	15.08	0.7015	0.5097	13.35	0.6899	0.5202	13.90	0.7079	0.4918	12.89	0.7027	0.5093	13.39
NAFNet	0.6668	0.5627	15.19	**0.6714**	**0.5559**	14.74	0.6727	**0.5589**	**15.13**	**0.6729**	**0.5599**	**14.65**	**0.6747**	0.5554	14.10
DeepSN-Net	0.7741	0.4230	12.76	0.7815	0.4071	12.55	0.7732	0.4233	12.78	0.7711	0.4259	12.72	0.7648	0.4303	12.59
DnCNN	0.7246	0.4787	11.75	0.7280	0.4795	11.80	0.7239	0.4792	11.74	0.7193	0.4789	11.69	0.7142	0.4791	11.64
U-Net	0.7638	0.4880	12.11	0.7743	0.4863	12.10	0.7628	0.4866	12.05	0.7546	0.4883	12.02	0.7449	0.4895	12.01
Related Degradations and Domains															
INFWIDE	0.8533	0.0696	8.44	0.8533	0.0696	8.44	0.8533	0.0696	8.44	0.8533	0.0696	8.44	0.8533	0.0696	8.44
MetaWeather	0.7150	0.5252	15.72	0.7458	0.4634	14.14	0.7293	0.4823	14.97	0.7561	0.4242	13.62	0.7904	0.3806	12.02
Pixel2Pixel	0.7332	0.5177	12.32	0.7340	0.5189	12.37	0.7334	0.5177	12.30	0.7309	0.5167	12.25	0.7288	0.5155	12.18
DehazeFormer	0.6721	0.5374	14.81	0.6737	0.5239	14.55	**0.6700**	0.5238	14.74	0.6733	0.5131	14.42	0.6767	0.5060	13.86
DarkIR	0.8071	0.0927	8.73	0.8096	0.0954	8.77	0.8066	0.0920	8.72	0.8060	0.0896	8.68	0.8050	0.0869	8.64
OEPRL	**0.6326**	**0.6063**	**16.97**	**0.6674**	**0.5650**	**15.12**	**0.6611**	**0.5624**	**15.25**	**0.6688**	**0.5634**	**14.77**	**0.6707**	**0.5615**	**14.85**

The same cross-configuration advantage holds on Lock. Across both content categories, the reconstruction advantage extends from changes in the wall signal to changes in how that signal is imaged by the camera.

The supplementary experiments connect reconstruction quality to the optical information available in the wall observation. Spatial interventions locate influential regions, deletion and retention tests show that selected regions concentrate useful support, and the shared-backbone comparison establishes the value of evidence organization. Across photometric, geometric, relay-surface, and camera-condition variations, OEPRL retains a consistent advantage over the compared methods. The reconstructed brightness, colors, regional layouts, and salient contours give this advantage a concrete meaning: an ordinary camera can use diffuse wall light to recover visual information from a screen whose displayed content is hidden from direct view.